

CHEMICAL PHYSICS AND APPLICATIONS OF DYNAMIC NUCLEAR
POLARIZATION-ENHANCED NUCLEAR MAGNETIC RESONANCE

by

Christopher Richard Parish

APPROVED BY SUPERVISORY COMMITTEE:

Dr. Lloyd Lumata, Chair

Dr. Anvar Zakhidov

Dr. Lindsay King

Dr. Jason Slinker

Dr. Robert Glosser

Copyright 2019
Christopher Richard Parish
All Rights Reserved

Dedicated to my parents: Without them I would never have gotten this far.

CHEMICAL PHYSICS AND APPLICATIONS OF DYNAMIC NUCLEAR
POLARIZATION-ENHANCED NUCLEAR MAGNETIC RESONANCE

by

CHRISTOPHER RICHARD PARISH, BS, MS

DISSERTATION

Presented to the Faculty of
The University of Texas at Dallas
in Partial Fulfillment
of the Requirements
for the Degree of

DOCTOR OF PHILOSOPHY IN
PHYSICS

THE UNIVERSITY OF TEXAS AT DALLAS

May 2019

ACKNOWLEDGMENTS

First, I must acknowledge my parents, as they were essential to helping me overcome dyslexia and in helping me get through the three years in which I was treated with chemotherapy for Ewing's sarcoma. Second, I would like to acknowledge Dr. Lloyd Lumata whose kindness unknowingly helped me to continue my education in spite of some residual psychological trauma which I had acquired while undergoing my second year of chemotherapy. Under his tutelage, my mind and rationale were able to return to their normal states and, perhaps, were even able to improve. Furthermore, I would like to thank Dr. Andhika Kiswandhi and Dr. Peter Niedbalski whose oversight speeded the recovery from "chemo-brain" and sharpened my rational mind. I would also like to thank my fellow graduate students in the Lumata research group, Qing Wang, Fatemeh Khashami, Ruchika Dhawan, Asiye Asaadzade, and Wirya Feizi for their camaraderie and help inside and outside the lab. I am also grateful to a number of undergraduate students who aided me in my experiments, namely, David Clark, Aya Cloyd, and Alan Zanders. Moreover, I would like to thank my committee members, Dr. Anvar Zakhidov, Dr. Robert Glosser, Dr. Jason Slinker, and Dr. Lindsay King. Thanks is also extended to our collaborators Dr. Charlie Khemtong of The University of Texas Southwestern Medical Center at Dallas and Dr. Likai Song of the National High Magnetic Field Laboratory in Tallahassee, Florida.

Finally, I would also like to thank the funding agencies that supported the projects in this dissertation. Funding for the research performed herein was provided by the United States Department of Defense (grant number W81XWH-17-1-0303), the Welch Foundation (grant number AT-1877-20180324), and the Cancer Prevention and Research Institute of Texas (grant

number RP180716. Additionally, the electron paramagnetic resonance (EPR) measurements were performed at the National High Magnetic Field Laboratory at Florida State University, which is supported by the National Science Foundation (DMR 1157490) and the State of Florida. A number of dynamic nuclear polarization (DNP) experiments were also performed at the Advanced Imaging Research Center (AIRC) at The University of Texas Southwestern Medical Center. The DNP hyperpolarization facility at the AIRC is supported by the National Institutes of Health (8P41-EB015908).

April 2019

CHEMICAL PHYSICS AND APPLICATIONS OF DYNAMIC NUCLEAR
POLARIZATION-ENHANCED NUCLEAR MAGNETIC RESONANCE

Christopher Richard Parish, PhD
The University of Texas at Dallas, 2019

Supervising Professor: Lloyd Lumata

Nuclear magnetic resonance (NMR) spectroscopy of nuclei with low magnetic moments such as ^{13}C spins can be quite challenging and time-consuming. Dynamic nuclear polarization (DNP) via the dissolution method greatly alleviates this sensitivity problem by enhancing the NMR signals of these insensitive nuclei by several thousand-fold. Dissolution DNP thus allows ^{13}C NMR tracking of cellular metabolism in living cells in real-time with superb sensitivity and high specificity. Herein, the bulk of my PhD dissertation work has been devoted to the elucidation and optimization of chemical physics of DNP technology in pursuit of attaining the highest NMR signal enhancements. One finding highlighted in this dissertation is the confirmation that the solid-state ^{13}C DNP efficiency is affected by the isotopic location of the ^{13}C label within the target molecule. Such can be explained via the thermal mixing model of DNP. Another major work in this dissertation is the investigation of the effects of ^2H enrichment of the glassing solvents on the solid-state ^{13}C spin-lattice T_1 relaxation times of hyperpolarized ^{13}C acetate. It is reported herein that glassing solvent deuteration elongates the ^{13}C T_1 relaxation times significantly, indicative of reduced intermolecular dipolar interaction of ^{13}C spins with ^2H spins compared to coupling with

^1H spins. Next, this dissertation also encompasses two studies regarding the effect upon DNP of doping samples with mixtures of two different free radicals as opposed to doping them with one type of free radical. In one of the two studies, it was determined that a mixture of the wide EPR width 4-oxo-TEMPO and narrow EPR width trityl OX063 yields interesting ^{13}C DNP results. There appears to be competing effects when the microwave irradiation frequency was set to the negative polarization peak of trityl OX063 which coincides with the positive polarization peak of 4-oxo-TEMPO. On the other hand, a mixture of both narrow EPR widths trityl and BDPA free radicals yields an additive effect. Finally, this dissertation also details the use of ^{13}C NMR in the characterization of ^{13}C -labelled amino acids and their application in investigating cancer cell metabolism. ^{13}C -labeled amino acids are potential hyperpolarized ^{13}C NMR spectroscopy and imaging (MRI) metabolic probes for cancer because a number of metabolic pathways that involve these biomolecules are abnormal in tumors. For instance, the enzyme branched chain amino acid transferase (BCAT), which catalyzes the conversion of branched chain amino acids (BCAA) to their ketoacid counterparts or vice versa, is overexpressed in several cancers. In this project, [1- ^{13}C] L-leucine and [1- ^{13}C] alpha-ketoisocaproate (KIC) were used to study the aberrant BCAT metabolic activity in glioblastoma. *SfXL* glioblastoma cells appear to preferentially convert ^{13}C -KIC to ^{13}C leucine rather than vice versa. Western blot experiments confirmed that BCAT expression is higher in *SfXL* cells than in normal astrocytes. Overall, this dissertation details the chemical tuning methods in DNP that I have unraveled in pursuit of attaining the highest ^{13}C NMR signal enhancements. These optimized DNP signals are crucial to the success of *in vivo* NMR or MRI studies, particularly in probing the hyperactive metabolism of cancer.

TABLE OF CONTENTS

ACKNOWLEDGMENTS	v
ABSTRACT.....	vii
LIST OF FIGURES	xi
LIST OF TABLES	xiii
CHAPTER 1 INTRODUCTION.....	1
1.1 The Fundamentals of NMR	1
1.2 The Basics of DNP.....	9
1.3 Cancer	24
CHAPTER 2 SOLVENT DEUTERATION IN DNP.....	31
2.1 Prior Findings.....	31
2.2 Methods.....	32
2.3 Results and Discussion	35
CHAPTER 3 THE EFFECT OF INTERMOLECULAR DEUTERATION AND ¹³ C LOCATION UPON DNP.....	42
3.1 Background	42
3.2 The Experiment.....	44
3.3 Results and Discussion	45
CHAPTER 4 THE IMPACT OF RADICAL MIXTURES ON DNP	51
4.1 Biradicals and Radical Mixtures	51
4.2 Two Experiments	53
4.3 Collective Results and Discussion	57
CHAPTER 5 CONCENTRATION DEPENDENCE OF DNP HYPERPOLARIZATION.....	72
5.1 DNP-assisted Spin Diffusion	72
5.2 Methods.....	76
5.3 Results and Discussion	78
CHAPTER 6 NMR CHARACTERIZATION OF AMINO ACIDS	85
CHAPTER 7 CANCER METABOLISM OF ALPHA-KETOISOCAPROATE AND LEUCINE	94

7.1 Leucine Metabolism in Cancer	94
7.2 The Experiment.....	95
7.3 Results and Discussion	97
CHAPTER 8 CONCLUSIONS	104
APPENDIX A WESTERN BLOT PROCEDURE.....	105
APPENDIX B CELL EXTRACT PROCEDURE.....	113
REFERENCES	121
BIOGRAPHICAL SKETCH	132
CURRICULUM VITAE	

LIST OF FIGURES

1	Definition of “peak” in an NMR spectrum.....	4
2	Definition of P(+) and P(-) in a DNP spectrum.....	11
3	Structures of the radicals used in this dissertation.....	18
4	Images of a homebuilt dDNP system and a homebuilt cryogen-free DNP system.....	22
5	Various microscope images of cancer cells.....	29
6	Deuterated and non-deuterated buildup data for two free radicals in two differing solvents..	35
7	Deuterated and non-deuterated decay data for trityl and TEMPO in two different glassing matrices.....	37
8	Deuterated and non-deuterated ESR data (T_1 temperature dependence and spectra) for two free radicals in either glycerol:water or DMSO:water.....	39
9	Examples of the ^{13}C DNP buildup curves and a histogram of the equilibrium polarizations using varying ^{13}C isotopic sites combined with both deuterating and leaving un-deuterated of sodium acetate.....	46
10	Examples of decay curves and a bar plot corresponding to the ^{13}C $T_{1\text{S}}$ of differing ^{13}C isotopic sites combined with possible deuteration of sodium acetate.....	48
11	DNP spectra recorded for a) radical mixtures typically containing an optimal concentration of trityl and variable concentrations of TEMPO and b) radical mixtures generally composed of equal parts trityl and BDPA.....	57
12	^{13}C buildup data corresponding to: (left) a mixture doped with an optimal concentration of trityl and a variable concentration of TEMPO irradiated at either the P(+) or the P(-) peak of trityl; and (right) irradiation of a [$1\text{-}^{13}\text{C}$] acetic acid:sulfolane glass doped with equal parts trityl and BDPA.....	60
13	^{13}C equilibrium polarizations and buildup times of: (left) a 3 M [$1\text{-}^{13}\text{C}$] sodium acetate containing glass, doped with 15 mM trityl and a variable concentration of TEMPO, irradiated at either the P(+) or P(-) peak of trityl; and (right) an [$1\text{-}^{13}\text{C}$] acetic acid:sulfolane glassing matrix doped with a variable concentration of equal parts trityl and BDPA.....	62
14	Top: ESR spectra of a) 10 mM trityl and TEMPO, both alone and separately at 10 K, or c) 10 mM trityl and BDPA, both alone and separately, recorded at 5 K. Bottom: Temperature	

dependence of the b) electronic spin-lattice relaxation rate of 10 mM trityl and TEMPO, both alone and together or of the d) electronic T_1 relaxation rate of 10 mM trityl and BDPA, both mixed and alone.....	65
15 Buildup (a) or decay (b) curves of 14.4 M $[1-^{13}\text{C}]$ and natural abundance pyruvic acid measured at 3.35 T and 1.2 K.....	78
16 The ^{13}C concentration dependence of ^{13}C hyperpolarization buildup times of $[1-^{13}\text{C}]$ pyruvic acid.....	80
17 The ^{13}C concentration dependence of equilibrium ^{13}C polarization for $[1-^{13}\text{C}]$ pyruvic acid.....	81
18 The ^{13}C T_{1s} as a function of concentration of $[1-^{13}\text{C}]$ pyruvic acid.....	83
19 ^{13}C NMR spectra of cell extracts and media such that each plot represents a time series involving <i>PC-3</i> cancer cells.....	98
20 Curves representing (top) the intra-cellular reaction between $[1-^{13}\text{C}]$ KIC and $[1-^{13}\text{C}]$ leucine and (bottom) the impact of this reaction upon the media about the (<i>PC-3</i>) prostate cancer cells.....	99
21 Curves representing (top) the reaction between $[1-^{13}\text{C}]$ KIC and $[1-^{13}\text{C}]$ leucine occurring within (<i>SfXL</i>) glioblastoma cancer cells. The bottom plot describes the reaction from ^{13}C -labeled KIV to valine in <i>SfXL</i> cells.....	100
22 The qualitative and quantitative results of a western blot performed upon glioblastoma and normal human astrocytes to determine the expression of BCAT.....	101

LIST OF TABLES

1	A comparison of the experimental and predicted ratios of the buildup times corresponding to 14.4 M and the other concentrations.....	79
2	Solubilities of ten amino acids at various concentrations in water and in 1:1 v/v water:glycerol.....	85
3	Solubilities of a) five or b) two amino acids in a) 12 M HCl or 1:1 v/v 12 M HCl:glycerol and b) 12 M NaOH or 1:1 v/v 12 M NaOH:glycerol.....	86
4	Graphical and tabular displays of ^{13}C NMR chemical shift locations of ten amino acids.....	87
5	Graphical and tabular descriptions of T_{1s} for ten amino acids, extrapolated from decay data.....	89
6	Chemical structures and Liquid-state enhancements for ten amino acids as measured under various conditions.....	90
7	^{13}C DNP buildup times and example buildup curves for nine amino acids, recorded at 9.4 T and under various conditions.....	91

CHAPTER 1

INTRODUCTION

Nuclear magnetic resonance (NMR) is a frequently used, non-invasive method by which one may determine the chemical makeup and relative concentrations of a given compound. By adding in space- or time- dependence, NMR may be used to monitor chemical reactions in real time or the location of such reactions in complex biological systems. However, NMR is insensitive when applied to non-zero spin nuclei other than ^1H . This insensitivity is largely removed via the application of a technique called dynamic nuclear polarization (DNP). Significantly, DNP allows ^{13}C nuclei to be tracked both *in vitro* and *in vivo*. This means that ^{13}C -labeled biomolecules such as amino acids may be traced in cancer cells. In this chapter, the basic concepts of NMR, DNP and cancer will be discussed.

1.1 The Fundamentals of NMR

In order to describe NMR, we must first come to understand spin. Spin is a kind of angular momentum which originates from Dirac's equation in such a manner that the Dirac Hamiltonian commutes with the total angular momentum, i.e., so that the total angular momentum is conserved. That is, spin is really a relativistic, quantum phenomenon, the dynamics of which may be approximated (for low momenta) by the Pauli equation:

$$\hat{H}\psi = \frac{(\vec{\sigma}\cdot\vec{p})^2}{2m}\psi \quad (0.1)$$

with $\vec{\sigma}$ a vector of Pauli spin operators, \vec{p} is the 3-momentum \hat{H} is the Hamiltonian operator, m is the mass of the fermion and ψ is the non-relativistic one-particle wave function (technically, this "wave function" is not like that found in Schrodinger's equation but is a separate object which

may only be rigorously based when treated as a field) [1]. As the Pauli spin matrices are of dimension 2, the wave functions are actually vectors with two components which represent the different directions of spin in a two-level system. Now the spin angular momentum for spin-half particles is given by $\hbar\vec{S} = \frac{\hbar}{2}\vec{\sigma}$. This concept of spin was first realized in reality in the Stern-Gerlach experiment [2].

Building upon the Stern-Gerlach experiment, I. I. Rabi et al. effectively invented NMR via using molecular beams to identify sodium's nuclear spin in 1938 [3]. However, it was F. Bloch and E. M. Purcell who, in 1946, extended this NMR method for gases to apply to solids and liquids [4], [5]. NMR primarily works off of the principle called Zeeman splitting: When infinitesimal magnetic dipoles, such as particles with spin half, are placed in an external magnetic field they will tend to align with or against the magnetic field [2]. Now, because there is a finite energy difference between these two orientations (given by $\Delta U = 2\mu \cdot B$, with ΔU the potential energy difference, μ the magnetic moment of the particle and B the external magnetic field strength [6]) a particle with spin aligned with the field can absorb enough energy to jump to the higher energy level via absorption of a photon of energy $E_i = \Delta U$ [2]. Later, when the spin relaxes, it releases a photon with energy $E_f = \hbar f_f$, with \hbar Planck's reduced constant and f_f the final photon's frequency. If B were the full extent of each nuclide's magnetic environment, then these two energies would be equivalent, $E_i = E_f$. However, almost every nuclide comes with an electron cloud. Being in a magnetic field, and, being charged, the electrons (classically) begin to rotate about the magnetic field. By Lenz's law, such produces an opposing magnetic field situated locally about each nucleus [6]. This oppositely oriented magnetic field acts in such a manner as to shield the nucleus. This means that the magnetic field about this nucleus varies slightly depending upon the location. Now,

because nearby nuclei are also experiencing this shielding effect, said field ends up encoding information about the environment of the nuclei [7], [8]. Thus, $\Delta E = E_f - E_i > 0$, which reveals itself through the chemical shift in an NMR spectrum, allows in-depth analyses of the environments of non-zero spin nuclei. While these magnetic fields are significant, they are frequently many times smaller than B because the z -component of the electron magnetic moment has a magnitude close to that of the Bohr magneton (which is quite small) [9]. So, any two instances of the isotope being examined have similar magnetic dipole moment magnitudes. Now, the magnetization is a vector that represents the density of magnetic dipole moments. As such, the total magnetization detected – the source of the NMR signal – is typically proportional to the difference between the number of nuclei aligned with the field and of those aligned against the field (multiplied by the average density of magnetic dipole moments) [6], [7]. Hence, defining the polarization of a sample as the fraction of this difference [$P = \frac{N_{\uparrow} - N_{\downarrow}}{N_{\uparrow} + N_{\downarrow}}$ for spin-1/2 particles, with

N_{\uparrow} (N_{\downarrow}) the number of nuclei parallel (anti-parallel) to the field], one is inevitably led to conclude that the NMR signal strength is at least proportional to the concentration of the nuclei within the sample being considered [10]. This is reflected in the following equation:

$$SNR \propto \gamma PC \quad (0.2)$$

where SNR represents the signal-to-noise ratio, which we shall from hereon typically refer to as the NMR signal strength, γ is the gyromagnetic ratio, P is the polarization and C is the concentration. To relate this definition of polarization to magnetization we note that, as the spin-half particle has an intrinsic angular momentum, it has an intrinsic magnetic moment given by

$\vec{\mu}_s = \gamma_s \hbar \vec{S}$. Hence, as the polarization is effectively the normalized magnetization, we must have that the polarization is given by:

$$\vec{P}_s = \frac{1}{\|\vec{\mu}_s\|} \frac{\text{Tr}\{\rho \vec{\mu}_s\}}{\text{Tr}\{\rho\}} \quad (0.3)$$

with $\vec{\mu}_s$ the magnetic moment vector of spin S and $\text{Tr}\{\rho\}$ the trace of the density matrix ρ of the ensemble [11]. Notice that, if we divide the numerator and denominator by the volume of the sample, we get that the polarization of spin S is the same as the normalized magnetization.

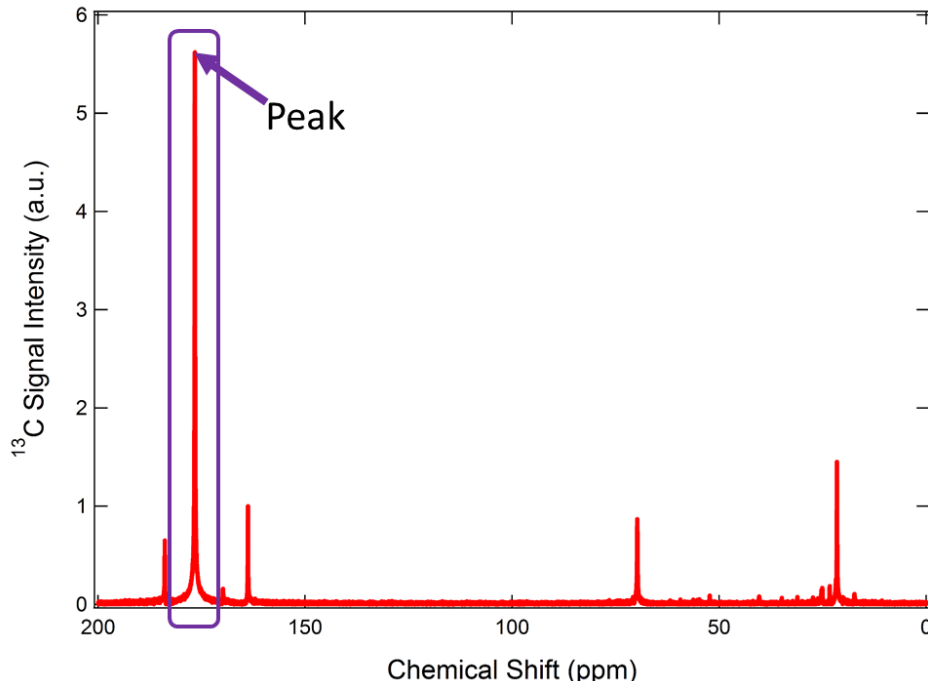


Figure 1: An example of an NMR spectrum such that the tallest peak is identified within a purple box.

An example of this NMR signal strength is shown in Figure 1, where we define a “peak” with the signal inside the purple box. This brings us to the topic of J-coupling, wherein, as NMR detects only nuclei with spin and, as spins measured parallel to the external magnetic field occupy a space of size $2IN+1$ (with I the value of the spin quantum number and N the number of like

nuclei), each nucleus must have $2I_N+1$ corresponding peaks. In this dissertation, when looking at NMR spectra, we shall typically be dealing with molecules that are labeled with but one ^{13}C nucleus. As such, J-coupling shall often be minimal herein (i.e., we shall frequently observe but one peak for any singly-labeled molecule).

Now, this process of a photon being absorbed and later emitted is called spin-lattice relaxation and the average time that must pass between the photon being absorbed and its emission is called the spin-lattice, or longitudinal, relaxation time, T_1 [8]. Macroscopically, spin-lattice relaxation can be identified with the magnetization associated with the net spin-half vector as follows: As nature seems to prefer lower energy states, the macroscopic equilibrium configuration contains more spins aligned with the magnetic field than anti-aligned spins [8], [12]. Furthermore, although all of the spins precess about B at their associated Larmor frequency, the deviations from the z -axis approximately cancels out leading to the net spin vector being along the z -axis [8]. Upon bombarding the system with photons having the same frequency as the particles' Larmor frequency, the net spin vector is tilted and precesses about the z -axis in such a manner that the net spin's projection upon the xy -plane is non-zero [8]. At this point, spin-lattice relaxation occurs so long as the lattice, in this case the nuclei containing the spins, produces fluctuating magnetic fields such that, upon reaching these spins, the fluctuations have the same frequency as the Larmor frequency of the spins [8]. In other words, spin-lattice relaxation is fundamentally an energy transfer between excited particles and their surroundings [8]. Now, these fluctuations in the lattice's magnetic field are, in the case of thermal relaxation, produced by thermal motions [8]. This may be understood as follows: The magnetic dipoles of two different nuclei in an external magnetic field are oriented along this external field. These two dipoles interact via a dipole-dipole

interaction which is dependent upon the distance separating the two dipoles. Motion of either an encompassing molecule or between two separate molecules containing the two dipoles can change this separation distance [8]. This changing inter-dipole distance causes the magnetic field produced by either dipole and felt by the other dipole to fluctuate.

In particular, the spin-lattice relaxation of electrons has been well-studied in the form of phonon exchanges between energy levels of a set of spins [13], [14]. In this dissertation, only three mechanisms of such energy exchanges between a set of energy levels and the lattice shall be relevant: the (1-phonon) direct process, the 2-phonon Raman process and the 2-phonon Orbach process. The direct process is essentially the absorption of a phonon of energy E followed by the emission of a phonon with the same energy E [13]. This means that only two energy levels are needed to describe this event [14]. Curiously, although the energy is conserved, this mechanism still drives relaxation because the probability of phonon emission is proportional to the Bose-Einstein statistical distribution plus unity, whereas the chance of phonon absorption is proportional to just the Bose-Einstein distribution [13]. Both of the 2-phonon processes, on the other hand, require three energy levels in their description, one of which is a transitory excited state. That is, the first phonon is annihilated by a spin in an upper energy state which uses this influx of energy to jump to a higher, temporary state [14]. This spin then creates a phonon and drops down into an energy level that is lower than the level it started in [14]. All three of these processes are characterized by the following dependence of their electronic spin-lattice relaxation rate, T_1^{-1} , upon temperature, T :

$$T_1^{-1} \propto T^\beta \quad (0.4)$$

such that $\beta \in \{0,1\}$ describes the direct process, $\beta \sim 2$ is ascribed to the 2-phonon Raman process and $\beta \geq 3$ characterizes a combination of the 2-phonon Raman and Orbach processes [13], [14].

Now, in reality, the external magnetic field is not perfectly homogeneous. This means that while the net spin is projected upon the xy-plane, the individual spins, being at different locations in the sample, feel slightly different values for the external magnetic field [15]. This affects their Larmor frequencies such that each individual spin begins to precess at a slightly different frequency than its neighbors. In turn, this means that the oppositely oriented magnetic field about each nucleus will take on a slightly different value than those of the neighboring nuclei. Hence, the magnetic moments – the components of the net magnetic field corresponding to the net spin – begin to de-phase from each other [15]. As this happens, the magnitude of the net magnetic moment of any particular group of nearby spins, as projected upon the xy-plane, must shrink and eventually become infinitesimal or zero. The time required for these spins to completely separate from each other, such that the magnitude of each group becomes ever smaller in the xy-plane, is called the spin-spin, or transverse, relaxation time, T_2 [15]. The T_2 time constant takes on particular significance when dealing with liquids [8] or solids [15] where the resonance line-shape (the shape of a peak in the sample's spectrum) is describable by a Lorentzian function. In such cases, the line-shape's line-width at half-height, $\Delta\nu_{Half}$, is given by:

$$\Delta\nu_{Half} = \frac{1}{\pi T_2} + \frac{\gamma\Delta B}{2\pi} \quad (0.5)$$

with ΔB the magnitude of the magnetic field inhomogeneities and γ the gyromagnetic ratio [8], [15]. This means that doping a solution with any substance that changes either of the nuclear relaxation times, such as gadolinium (III), leads to alteration of the NMR spectral peak-widths.

An additional factor that must be accounted for when irradiating a system of nuclei doped with paramagnetic ions is spin diffusion. Spin diffusion, as defined by the one who first described it, is the diffusion of quanta (usually photons or phonons) toward the radicals [16]. That is, the irradiation photons are absorbed by spins distant from the electron sources; this causes those spins to flip to be anti-parallel with the external field; then the distant nuclei emit phonons, flipping back to being parallel to the field while the phonon is absorbed by the nucleus which is next nearest to the closest radical; this process then repeats (less the absorption of a photon) until the phonon is absorbed by the free radical; finally, the phonon is re-emitted but, this time, is absorbed by the lattice formed by the free radicals [16]. When the quantum is absorbed by the lattice of electrons, the spins of the radicals use the energy to rearrange themselves instead of flipping [16]. This diffusion process can be equally described as the diffusion of a spin state (the state in which a spin is anti-parallel to the field) towards the free radical. Additionally, according to Khutsishvili, in the ideal case, one may treat each nucleus as within a “sphere of influence” [17]. That is, the nuclei within each such sphere would only feel the relaxation effects of the radical sitting in the center of that sphere – the impact upon nuclear relaxation from all other radicals would be negligible [17]. Further, when considering this ideal case, Khutsishvili defined the volume of such a sphere, V , and the concentration of free radicals in said sphere, C , by: $V \cdot C = 1$ radical. Using these definitions, Khutsishvili determined that there exists something called a spin diffusion barrier. Originally, spin diffusion was thought to be limited to only occurring outside this spin diffusion barrier – a distance which marked the region in which the spin-diffusion process would cease to conserve energy [16], [17]. However, Horvitz demonstrated that spin diffusion actually occurs within said barrier as well as without, just with different rates [18]. Furthermore, Ramanathan

proved that a combination of electron spin dipolar couplings and the fluctuations of the spin of a free radical aid transport thru the diffusion barrier [19].

According to Boltzmann statistics, the NMR signal intensity for any spin-1/2 particle is given by:

$$P = \tanh \left(2 \frac{|\vec{\mu} \cdot \vec{B}|}{k_B T} \right) \quad (0.6)$$

with \vec{B} the strength of the magnetic field, $\vec{\mu}$ the magnetic moment of the particular nucleus, T the temperature of the ensemble and k_B the Boltzmann constant. Hence, in high magnetic fields and at low temperatures, the polarization is roughly linear in the argument – it becomes proportional to the nuclear gyromagnetic ratio, γ . Thus, nuclei with low gyromagnetic ratios, such as all nuclei other than ^1H 's (which have $\gamma \cong 43 \frac{\text{MHz}}{T}$), are relatively difficult to measure with NMR. Therefore, as wonderful as NMR is, it still has some issues: it is limited in resolution and sensitivity. Fortunately, dissolution DNP and DNP fix this sensitivity problem for liquids and solids, respectively.

1.2 The Basics of DNP

While the nuclei other than ^1H all have such low γ s that they are quite difficult to measure in practice, the electron has a γ which is three to four magnitudes greater than that of any nucleus ($\gamma_{electron} \cong 28,000 \frac{\text{MHz}}{T}$). This fact is key to the idea behind DNP: It effectively transfers the polarization of the electrons to the nuclei. Experimentally, this is carried out by: doping a solid (or amorphous liquid if the solution is then frozen), which already contains a lattice composed at least

partly of non-zero spin nuclei, with a few paramagnetic molecules (such as free radicals in the amorphous liquid case) which each have a Larmor frequency of ω_e [20]. This is followed by applying microwaves which are slightly off-resonance with the electron spin resonance (ESR) – i.e., the sample is bombarded by microwaves of frequency $\omega_{\text{microwave}} = \omega_e \pm \omega_{\text{nuclear}}$, such that ω_{nuclear} is much smaller than ω_e [20]. Such results in the nuclei taking on a polarization that is, at the very least, much larger than they may obtain in thermal equilibrium and possibly similar to the electronic polarization in magnitude [20]. This is made possible by the dipolar interaction (DI) between the electronic spins S, and the nuclear spins I. In particular, the DI allows flip-flips, which are simultaneous reversals in the same direction of S and I (i.e., $\omega_{\text{microwave}} = \omega_e + \omega_{\text{nuclear}}$), and flip-flops, which are simultaneous reversals of S and I in the opposite direction (i.e., $\omega_{\text{microwave}} = \omega_e - \omega_{\text{nuclear}}$) [20]. Now, these flip-flips and flip-flops must conserve energy – meaning that this missing energy need either be sent to or acquired from the lattice (i.e., via phonons) or that this energy comes from a source external to the system [20]. If it is by phonons, then said flip-flips/flip-flops represent spin-lattice relaxation to one of the two Zeeman levels, where which level is being “relaxed to” depends upon the initial orientation of the electrons and the microwave frequency used [20]. Yet, at low temperatures, while the nuclei tend to flip/flop at rates on the order of around 10^{-3} s^{-1} , the electron spins tend to flip/flop (without a nucleus necessarily flipping or flopping in tandem) at a rate on the order of about 10^3 s^{-1} [20]. Hence, the free radicals tend to flip so fast that there is little danger that any nucleus will flop simultaneously with the electron. This model of a nucleus-electron pair experiencing flip-flops/flip-flips followed by the free radical regaining its original orientation is called the solid effect (SE). Specifically, there are two versions

of the SE: the well-resolved solid effect wherein the linewidth of the ESR spectrum of the radical is smaller than the nuclear Larmor frequency [11]; and the differential SE in which the EPR spectra of the radical is on the same order as the nuclear Larmor frequency [11]. Curiously, in the differential SE, both positive and negative polarization may be transferred to the nuclei, while only one sign of polarization may be acquired by the nuclei in the well-resolved SE [11].

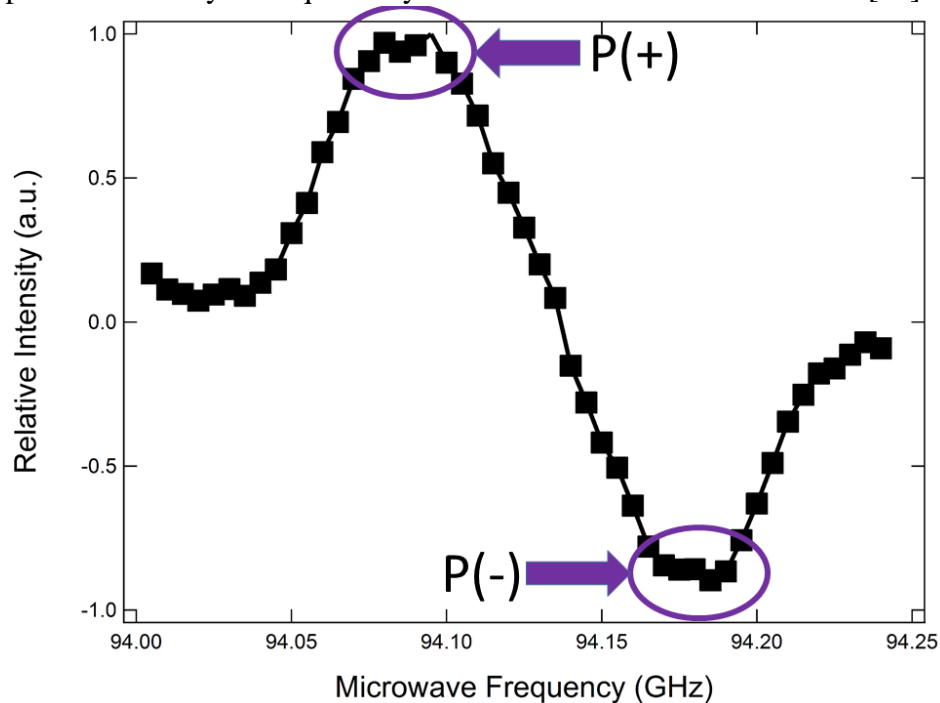


Figure 2: An example of a ^{13}C DNP microwave frequency sweep; P(+) and P(-) are identified in purple circles with accompanying labels.

We define the P(+) and P(-) DNP enhancement peaks as in Figure 2. Specifically, P(+) denotes the peak at which the majority, if not all, of the nuclear spins are oriented anti-parallel with respect to the external magnetic field while P(-) represents the peak where most of the nuclear spins are directed parallel with the field.

Now, around 1967, Hwang and Hill found that, by raising the concentration of a bis-phenyl aroxyl free radical in polystyrene, the DNP enhancement peaks P(+) and P(-) became closer to each other [21]–[23]. The mechanism behind this behavior – the cross effect (CE) – was quickly investigated experimentally. The CE is like the SE, but with one extra electron per nucleus–electron pair: In this case, the two radicals must have resonant frequencies, ω_{e_1} and ω_{e_2} , with a difference whose magnitude is the Larmor frequency of the nucleus [24]; If so, then all three spins involved flip in tandem due to a resulting degeneracy in the energy levels of the states of the system [21]. That is, when this requirement is satisfied, the probability that all three spins involved will flip becomes maximal [24]. However, when this CE condition is not met, said transition probability plummets [24]. In addition to this required equality, the CE regime requires 1) that the inhomogeneous ESR line-width be strictly greater than the nuclear Larmor frequency and 2) that the homogeneous EPR line-width be strictly less than the nuclear Larmor frequency [21]. Yet, another regime, called thermal mixing (TM), can also be active under these conditions [21]. One of the main differences between TM and CE are that the CE regime (but not the TM regime) is applicable when the ESR line is inhomogeneously broadened [21]. It should be noted that both the CE and TM regimes display a much speedier build-up of polarization than the SE regime [21]. This may be tied to the fact that the CE and TM regimes are founded upon allowed transitions, whereas SE is based upon forbidden transitions [21].

In some qualitative respects, TM may be understood as like CE, but with a system of electrons (i.e., more than 2 radicals) [21]. TM has been modeled primarily in two ways: For most of the history of TM, it has been described thermodynamically; however, recently, TM has begun to be modeled from a quantum mechanic perspective. We shall first portray the thermodynamic

prescription followed by the quantum mechanical version. In all variants of TM, the condition for TM to be applicable is that the linewidth of the ESR line-shape of the radical used must be greater than the Larmor frequency of the nuclei to be polarized [21].

The thermodynamic picture is based around something called “spin temperature” [25]. That is, the Boltzmann distribution is assumed to hold so long as the spin ensemble is in an internal equilibrium, as opposed to holding only so long as the system is in thermal equilibrium with its environment [25]. This spin temperature is thus a sort of description of the order of the ensemble and is not necessarily the same as the temperature of the lattice [25]. Due to this definition of spin temperature, one may define a variant of thermal contact between two reservoirs containing order. In TM, once established, this thermal contact (or what Goertz refers to as being “on resonance” [25]) allows the electron Zeeman reservoir to exchange energy with the electron dipolar system [25]. Specifically, the application of a radio-frequency field can cause spins which were parallel to the external field to flip to become anti-parallel with the field [25]. Hence, the magnetic field felt by the average magnetic moment in a frame rotating with said moment should decrease [25]. Furthermore, as a fairly large number of spins flip with the application of this radio-frequency field, this flipping of spins also causes the entropy associated with the spins to fall – lowering the spin temperature felt by the average Zeeman element [25]. The reduction in the magnetic field also shrinks the distance between Zeeman energy levels to the point where the electron Zeeman transition energy becomes similar in magnitude to the transition energy between different configurations of the electron magnetic dipoles [25]. Hence, the application of a radio-frequency field brings the electron Zeeman and electron dipolar reservoirs into thermal contact [25]. Now, the electron dipolar and nuclear Zeeman systems already happen to be in thermal contact due to

their similar transition energies [25]. Thus, via application of radio-frequency irradiation, one may cool the three reservoirs and, in so doing, raise the amount of order in the ensemble – resulting in a high percentage of spins being either parallel or anti-parallel with the external magnetic field.

The thermodynamic characterization of TM has resulted in multiple models of which perhaps the most well-known is Borghini’s model [20]. This model, developed by Borghini and popularized by Abragam and Goldman, requires that one assume the spin temperature to be low and that the ESR line-shape be describable by an excessively simplified model [20]. Borghini’s model may then be encapsulated in the following equation:

$$\Delta_0 |P_0| + \frac{\omega_n}{C} \frac{T_{1,n}^{-1}}{T_{1,e}^{-1}} P_n = \int_{-\infty}^{\infty} \tanh\left(\frac{1}{2} \beta \Delta\right) \Delta f(\Delta + \Delta_0) d\Delta \quad (0.7)$$

where C is the relative concentration of free radicals, $T_{1,n}^{-1}$ is the nuclear spin-lattice relaxation rate, $T_{1,e}^{-1}$ is the electronic spin-lattice relaxation rate, Δ is the electronic wave-packet’s frequency such that Δ_0 is the frequency of some specific electron wave packet, P_n is the polarization of the nuclei, P_0 is the thermal equilibrium polarization of the free radicals, β is the inverse spin temperature in units of seconds, ω_n is the nuclear Larmor frequency and $f(\Delta)$ is the electronic EPR resonance line (which shall from hereon be referred to simply as the ESR line-shape) [20]. Unfortunately, the Borghini model has its share of problems: it is only valid when the applied microwave field is sufficiently strong; it is only reasonably accurate when both the average electronic Zeeman energy and the average of the sum of the nuclear Zeeman and electron dipole-dipole energies are roughly constant in time; Borghini’s model requires that the spin diffusion between free radicals be incredibly efficient; that the contact between nuclei and free radicals be flawless; and it requires that the ESR line-shape be fully saturated [26]–[29]. In 2012 and 2013,

Serra et al. built modified Borghini models in which they investigated the effect of weakening the contact between the nuclei and radicals [26], the effect of varying both the strength of the electron-nuclei contact and the degree of microwave saturation [29], and the effect of varying the rates of both energy conserving and energy non-conserving spin diffusion among electrons [28]. Later, in 2017, Wenckebach constructed a modification to Borghini's model in which he was able to remove the two requirements that the microwave be strong and that the average energies be constant [27]. In all these modifications to the Borghini model, the electronic spin-lattice relaxation rate and the EPR line-shape play significant roles, whereas, in Borghini's original model, only the ESR line-shape plays an important role [the second term in the left hand side of equation (0.4) tends to be very, very small, and thus negligible, due to $T_{1,e}^{-1} \gg T_{1,n}^{-1}$ being common]. For example, Wenckebach's model for the nuclear polarization, P_n , in TM is signified by the following equation:

$$\begin{aligned} \frac{N_n}{N_e} \omega_{0,n} \frac{\partial}{\partial t} P_n = & -T_{1,e}^{-1} \int_{-\infty}^{\infty} d\omega f(\omega) (\omega - \omega_0) \tanh \left[\frac{1}{2} (\omega_0 \alpha + (\omega - \omega_0) \beta_{NZ}) \right] \\ & - 2W(\omega_m) (\omega_m - \omega_0) \tanh \left[\frac{1}{2} (\omega_0 \alpha + (\omega_m - \omega_0) \beta_{NZ}) \right] \end{aligned} \quad (0.8)$$

where N_n is the number of nuclei in the sample, N_e is the number of radicals within the sample,

$W(\omega_m)$ is defined by $W(\omega_m) = \frac{\pi}{2} (\omega_{1,e})^2 f(\omega_m)$, with ω_m the microwave irradiation frequency

and $\omega_{1,e} = \gamma_{electron} \|\vec{B}_1\|$, where \vec{B}_1 is the microwave irradiation amplitude, α is the inverse

temperature assigned to the electron Zeeman reservoir, β_{NZ} is the inverse temperature associated

with the electron non-Zeeman ensemble, $\omega_{0,n}$ represents the nuclear Larmor frequency and ω_0 is

defined by $\omega_0 = \int_{-\infty}^{\infty} \omega d\omega f(\omega)$ such that ω denotes the frequency of the electron wave packet [27].

Notice that the first term on the right hand side of equation (0.8) is multiplied by the electronic spin-lattice relaxation rate – suggesting that this relaxation rate is an important part of this model.

However, as Borghini’s model has been around for a substantially longer period of time, we shall tend to use Borghini’s model more than modifications to it. Based upon Borghini’s model, one may derive the greatest attainable nuclear polarization to be:

$$\max P_{\frac{1}{2}} = B_{\frac{1}{2}} \left(\hbar \beta_L \frac{\omega_e \omega_{\frac{1}{2}}}{4D} (\eta(1+f))^{-\frac{1}{2}} \right) \quad (0.9)$$

with $B_{\frac{1}{2}}(\cdot)$ representative of the Brillouin function for a spin-half particle, ω_e the Larmor frequency of the free radical, $\omega_{\frac{1}{2}}$ the Larmor frequency of the spin-half nucleus, β_L the inverse temperature of the lattice, D the line-width of the ESR line, η the ratio $\frac{T_D^{-1}}{T_Z^{-1}}$ (where T_Z^{-1} is the electron Zeeman relaxation rate and T_D^{-1} is the electronic dipolar relaxation rate) and f is the relaxation leakage factor [30]. The relaxation leakage factor represents all nuclear relaxation processes in which the cooling is not accomplished by way of the electron dipole-dipole reservoir [30].

The quantum variant of TM is chiefly concerned with modeling it via a single nucleus – multiple electron system. In [31], Hovav et al. proved that, upon microwave irradiation, such a system should, in theory, give rise to the spin temperature concept. In the same work, they also proved that this irradiated system must, in theory, undergo TM when the associated ESR line-width is homogeneously broadened and that said system will instead undergo a mixture of the SE and CE if the EPR line-width is in-homogeneously broadened [31]. Curiously, Hovav et al. also

demonstrated that the spin temperature concept is ill-defined if the microwave power is not sufficiently great [31].

A growing body of evidence suggests that TM tends to be applicable at low temperatures and high field strengths: Prior reports have established that at cryogenic temperatures (around 1.4 K) and magnetic fields of about 3.35 T hyperpolarization of samples containing ^{13}C nuclei and doped with either trityl (both mono-radicals and bi-radicals) or TEMPO tends to be largely driven by TM [32]–[34], [34]–[39]. Additionally, according to an experiment performed by W. de Boer, hyperpolarization of samples containing ^1H or ^2H nuclei and doped with BDPA proceeds via a combination of the SE and TM mechanisms when at 0.5 K and approximately 2.5 T [40]. As this result has been placed on a sound theoretical footing by Karabanov et al. [41], we may assume that de Boer's results extend to ^{13}C nuclei.

This dependence, in both Borghini's model and the modified Borghini models, upon the ESR line-shape and the electronic spin-lattice relaxation rate means that the radicals used are significant to DNP. Further, being important to DNP means that they must be crucial to dDNP. Three commonly used radicals that shall also be used in the experiments below are trityl OX063 (trityl) and α,γ -bis(diphenylene)- β -phenylallyl (BDPA), which represent narrow (ESR) linewidth free radicals, and 4-oxo-TEMPO (TEMPO), which is a mono-radical with a wide (EPR) linewidth. When the ESR linewidth is representative of the width of the EPR line-shape measured at 2% of the height (where the 2% height is measured from the base of the line-shape), trityl has a linewidth

of 62 MHz, BDPA a linewidth of 115 MHz and TEMPO has a linewidth of 465 MHz [42]. These three radicals are pictured in Figure 3 below.

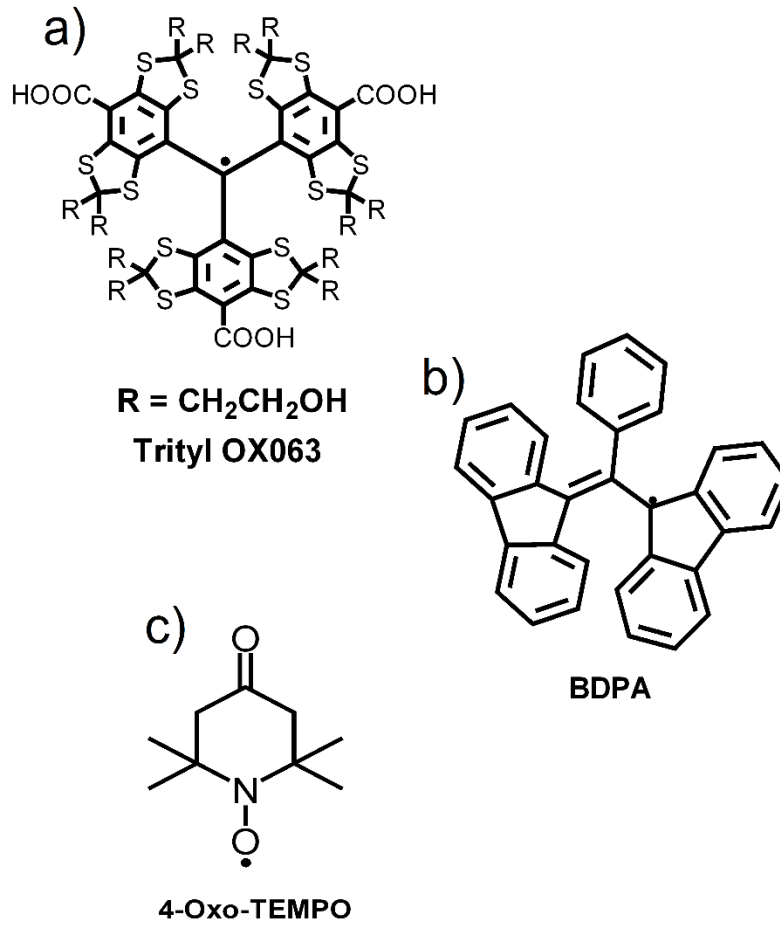


Figure 3: Structures of the three free radicals used in the experiments below: a) trityl, b) BDPA and c) TEMPO.

Under the TM regime, these ESR linewidths correspond to specific heat capacities, each given by:

$$C_z = NA\Delta^2 \quad (0.10)$$

with N the number of like radicals in the solution, A a constant dependent upon the spin quantum number of said radicals and Δ the difference between the electronic Larmor frequency and the

frequency of the microwave irradiation such that Δ is proportional to the EPR linewidth [25]. These specific heat capacities are each associated with a potential electron Zeeman reservoir (depending upon which radical is used to dope the sample). As such, the thinner the ESR linewidth of the radical used, the smaller the resulting heat capacity of the electron Zeeman system. The definition of heat capacity demands that the smaller it is, the less energy is needed to reduce the temperature of the corresponding electron Zeeman reservoir. Hence, if the same energy of microwave irradiation were to be used for two different radicals, the sample doped with the radical having the smaller EPR linewidth would see its electron Zeeman system attain the lower temperature.

Similarly, according to TM, the specific heat capacity of the nuclear Zeeman system, C_{NZ} , is given by:

$$C_{NZ} \propto (\gamma B_{\text{local}})^2 \quad (0.11)$$

with B_{local} representing the local magnetic field about the nuclei [25].

Now, behind all of the above regimes lie the basic flip-flop and flip-flip transitions driven by microwave irradiation. As such, the rate at which the nuclear polarization builds up in any of these regimes may be approximated by the nuclear polarization build up rate in this simplified model. This rate is derived in [20] for a nucleus in a lone electron-nucleus system to be roughly:

$$\frac{d}{dt} P_n \approx -\frac{1}{t_{bu}} (P_n - P_{\text{equilibrium}}) \quad (0.12)$$

with P_n the nuclear polarization (which has an initial value of zero), t_{bu} the build-up time and $P_{\text{equilibrium}}$ the nuclear polarization at equilibrium [20]. Furthermore, when the magnetic moment of

an electron is placed in a magnetic field, \vec{B} , it begins to precess in accordance with Bloch's equations:

$$\frac{\partial \vec{P}_{e^-}}{\partial t} = -\gamma_{e^-} \vec{B} \times \vec{P}_{e^-} \quad (0.13)$$

where \vec{P}_{e^-} is the polarization of the electron and $\gamma_{e^-} \approx -28,000 \text{ MHz/T}$ is the magnetic moment (with the correct sign) of the electron [11]. This eventually leads to a more accurate rate equation than equation (0.12):

$$\frac{\partial P_s^z(t)}{\partial t} = -2WP_s^z(t) \quad (0.14)$$

with $P_s^z(t)$ the z-component of the polarization and W the transition rate [11]. However, the rates dealt with in equation (0.14) and (0.12) are not necessarily the same: equation (0.14) involves the (average) rate at which a spin transitions from one Zeeman level to the next, whereas equation (0.12) describes the time required for either nearly all the spins, or as many spins as possible, to gather in one energy level.

Dynamic nuclear polarization was largely applied to solid-state samples until 2003 when Ardenkjaer-Larsen et al. invented dissolution DNP (dDNP) [35], [43]–[46]. In dDNP, the aliquot first undergoes DNP; then, once the sample (via the sample cup) is lifted out of the liquid helium, super-heated solvent is *carefully*, but rapidly, injected via the injection wand into the sample cup [43]. If the resulting liquid is intended for an application where sterility is not a concern, it is then pressured through the injection wand and into an external container [43]. (In the experiments discussed in this dissertation, said container was typically a NMR tube with a diameter of 10 mm placed inside a superconducting magnet built to perform NMR.) Thus, a hyperpolarized solution is produced at physiological temperatures. However, as transportation of this solution necessarily

removes it from the magnet and the microwave irradiation, this hyperpolarization decays, sometimes quite rapidly. The magnetization of the resulting solution then decays according to:

$$M = M_0 \sin \theta (\cos \theta)^{\frac{t}{TR}} e^{-\frac{t}{T_1}} \quad (0.15)$$

where M_0 is the initial signal intensity, θ is the flip angle, TR is the repetition time, t is the time and T_1 is the spin-lattice relaxation time [47].

While the mechanisms behind DNP and dDNP have been briefly reviewed, there has, as of yet, been no mention of a qualitative measure demonstrating the improvement of dDNP over NMR. That is rectified via the signal enhancement. Such an enhancement, ε , may be measured via:

$$\varepsilon = \frac{\frac{A_{\text{hyperpolarized}}}{S_{\text{hyperpolarized}} \sin \theta_{\text{hyperpolarized}} c_{\text{hyperpolarized}}}}{\frac{A_{\text{thermal}}}{S_{\text{thermal}} \sin \theta_{\text{thermal}} c_{\text{thermal}}}} e^{-\frac{t}{T_1}} \quad (0.16)$$

with $A_{\text{hyperpolarized}}$ (A_{thermal}) the area under the hyperpolarized (thermal) peak(s) of the compound being investigated, $\theta_{\text{hyperpolarized}}$ (θ_{thermal}) the radiofrequency flip angle used to acquire the hyperpolarized (thermal) spectra, $c_{\text{hyperpolarized}}$ (c_{thermal}) the solute concentration used in acquiring the hyperpolarized (thermal) spectra and $S_{\text{hyperpolarized}}$ (S_{thermal}) is the number of scans used to acquire each hyperpolarized (thermal) spectrum [33]. Typically, $S_{\text{hyperpolarized}}$ equals unity because each spectra has an incredibly low signal-to-noise ratio and, more importantly, the NMR signal is rapidly decaying so that any two spectra taken at different times cannot be averaged to get a spectrum with a better signal-to-noise ratio.

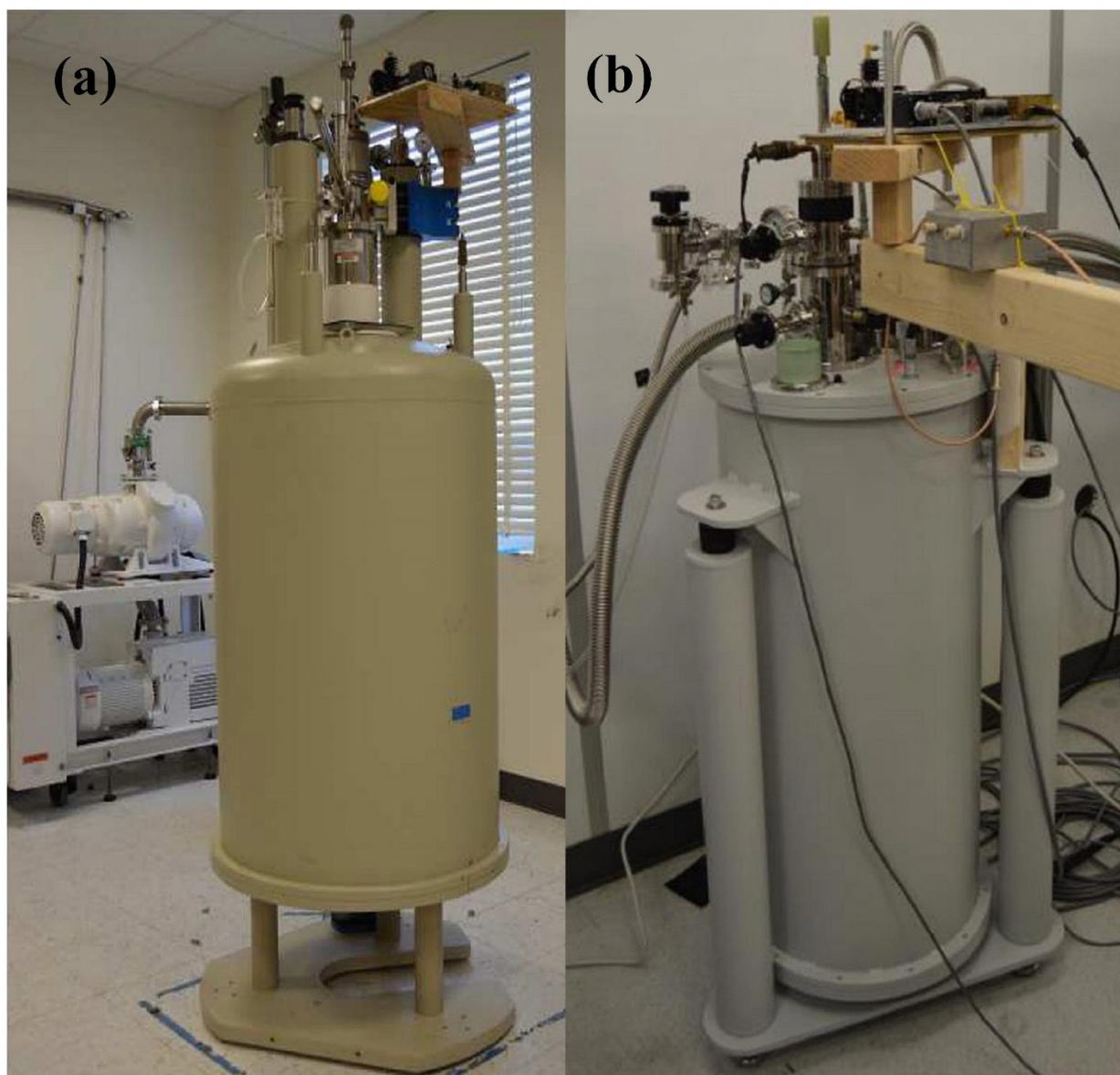


Figure 4: Pictures of: (a) a home-built dissolution DNP polarizer [48]; and (b) a home-built cryogen-free DNP polarizer [49]. (a) was reproduced from [48] A. Kiswandhi *et al.*, “Construction and ^{13}C hyperpolarization efficiency of a 180 GHz dissolution dynamic nuclear polarization system,” *Magn. Reson. Chem.*, vol. 55, no. 9, pp. 828–836, 2017, with the permission of AIP Publishing; and (b) was reproduced from [49] A. Kiswandhi, P. Niedbalski, C. Parish, Q. Wang, and L. Lumata, “Assembly and performance of a 6.4 T cryogen-free dynamic nuclear polarization system,” *Magn. Reson. Chem.*, vol. 55, no. 9, pp. 846–852, 2017, with the permission of AIP Publishing.

With this definition of enhancement, we may quantify the improvement of dDNP over NMR: In [43], which initiated dDNP, the hyperpolarized liquid was found to be enhanced by more than 10,000 times. When using a home-built dDNP system [see Figure 4 (a)], we were able to net liquid-state enhancements of ~241,000 or ~98,000 when using trityl or TEMPO, respectively [48]. This corresponded to polarization percentages of 21% and 8.5 %, respectively [48]. However, due to the high costs of liquid helium, we eventually modified a C-Mag Vari-9 Research System (Cryomagnetics Inc., Oak Ridge, TN) into a cryogen-free DNP system [see Figure 4 (b)] and switched from primarily using the previously mentioned home-built dDNP system to mainly using this cryogen-free system [49].

Finally, when DNP is involved spin diffusion bifurcates into pure spin diffusion and DNP-assisted spin diffusion: Pure, or, as it is sometimes called, spectral, spin diffusion is as described previously in the NMR subsection [50]. DNP-assisted spin diffusion, however, is in some ways the reverse – in DNP-assisted spin diffusion the polarization moves away from the radical instead of towards it [51]. This last means that, in effect, the spins travel away from the radical. While this may initially seem the same as pure spin diffusion, the difference lies in that the spin state that is undergoing the random walk is not restricted to being anti-parallel to the external field. According to Hovav et al., the nuclei in the bulk show slower build-up times than nearer nuclei so that an increase in bulk nuclei concentration leads to rising build-up times [50]. They also proved that the majority, by far, of the NMR signal that is measured during DNP originates from the bulk nuclei [50]. Curiously, Karabanov et al. demonstrated via a simulation involving 1330 nuclei that the rate of spin diffusion depends upon the entire spin ensemble's state [52]. This is most peculiar – it suggests that the rate of occurrence of flip-flop transitions between both nuclei and the radical and

between two nuclei depends not upon the microscopic properties, such as the immediate environs of the free radical or of the nuclei, but instead depends upon global properties, such as the polarization of the whole nuclear ensemble.

1.3 Cancer

Cancer, in rather simplistic terminology, is one or more clumps of cells which generally tend to spread throughout the body [53]. Cancer arises due to a sequence of mutations in the cell's DNA [54], or because of epigenetic mutations (such as alterations in DNA repair genes – alterations allowing errors in a particular cell's DNA to go uncorrected, leading to daughter cells and their daughter cells, and so on, to carry said errors) followed by genetic mutations [55]. These mutations occur as a result of any combination of: DNA-damaging environments, mistakes made by proteins devoted to repairing DNA damage, DNA replication errors, errors in cellular re-combinations, and, on rare occasions, one or more mutations passed from parent to child via the germ line [56].

For cancer, genetic mutations involving either the development of new oncogenes (genes that promote cell growth and division), over-expression of current oncogenes, the under-expression of tumor suppressors, or the disabling of tumor suppressor genes are particularly significant [57]. Via these mutations, a cell may acquire genetic instructions promoting its survival and reproduction over that of the whole organism – genetic instructions that often increase the mutation accumulation rate leading to what is called “clonal evolution,” or the placement of the mutated cell and its kin on evolutionary competitive grounds with respect to nearby cells lacking in these mutations [58]. Thus, via extrapolation, we arrive at a similar conclusion as Hanahan and Weinberg, there are eight categorical characteristics of cancer:

- 1) The ability to avoid apoptosis (cell death);
- 2) The tendency to continually reproduce;
- 3) The ability to metastasize;
- 4) The tendency to be ignored by the immune system;
- 5) The ability to ignore anti-growth signals;
- 6) The tendency to maintain angiogenesis (i.e., the creation of new blood vessels from previously existing blood vessels) for extended periods;
- 7) The ability to reprogram energy metabolism; and
- 8) The tendency to be self-sufficient with respect to growth signals [59], [60].

That is, via consideration of the incredibly large number of cells in the average human body (which implies that the law of truly large numbers is applicable according to [61]), multiplied by the average human's lifespan and divided by the average cell's lifespan, combined with the rather high error accumulation rate in the average mammalian cell's DNA (natural DNA damage occurs more than 60,000 times every day per mammalian cell according to [62]), one arrives at: characteristics 1), 4), 5), and 8) when considering that evolutionary theory favors organisms with longer lifespans in tandem with the above; we reach characteristic 2) via the expectation that higher reproductive rates lead to increased proportions of highly reproductive organisms to less reproductive organisms in some environment; characteristics 6) and 7) are found via adding in consideration of both the nutrient requirement for higher cell division rates or greater cell lifetimes and adding in that increased nutrient levels within the environment, or increased energy efficiency in the cell, provides the cancer cells with an evolutionary advantage; and one finds characteristic 3) through combining the evolutionary advantages of higher reproductive capability and lower resource-

competition (which occurs when the offspring are moved to a different location than the parent such that the offspring have a competitive advantage in the new setting).

Now, cellular reproduction cannot occur without resources – without the building blocks which make up a cell. One of the key categories of building blocks of a cell is that of proteins. Proteins, which are built out of amino acids, are macromolecules significant in cell metabolism, cell signaling, the immune response of a body and are important in the cell cycle [63]. Amino acids are biological compounds made up of carboxylic acid (COOH) and amine (NH₂) functional groups (a functional group is a set of atoms/bonds in a molecule which determine said molecules' chemical-reaction-behavior) along with a unique side chain [64]. Amino acids are largely essential nutrients for all cells, including those that are malignant. This is because amino acids join to create proteins and, significantly, not all amino acids are encoded for in human DNA.

While there exist at least five hundred known amino acids [65], there are only about twenty-two amino acids used for building proteins [66]. Of these twenty-two amino acids, there exist but twenty (standard) amino acids coded for in DNA [63]. Out of these twenty, only ten were initially investigated: leucine, valine, isoleucine, arginine, glutamine, alanine, serine, glycine, methionine and proline. Just two of those amino acids came to be relevant to experiments described herein: leucine and valine. In particular,

- Leucine has been noted for manipulating cell growth via activating mammalian target of rapamycin kinase (the mechanistic target of rapamycin enzyme, such that mammalian target of rapamycin is a protein, which regulates cell growth, motility, and proliferation as well as protein synthesis, autophagy – the process

of cell degradation of unnecessary/dysfunctional cell parts – and protein transcription) [67].

- Valine has been noted for its role in muscle growth and tissue repair, especially in those with liver disease, injuries, or who have had surgery [68]; valine is also a source of energy which can replace use of glucose [68].
- Arginine has been noted for speeding up wound healing and, thus have the effect of increasing mitotic cell division rates [69].
- Glutamine has been noted as providing energy to cells [70], and as providing carbons for the citric acid cycle and nitrogens for anabolic processes [71], [72].
- Alanine has been noted for its niche in the glucose-alanine cycle between tissues and the liver: in tissues which degrade amino acids for energy, glutamate sends its amino group to pyruvate which results in alanine and alpha-ketoglutarate; this alanine is then sent to the liver where it is transformed into glucose and glutamate; thus alanine is key for a cell's disposal of pyruvate [73].
- Serine has been noted for its significant role in the biosynthesis of purines and pyrimidines (biomolecules that are building blocks for DNA, RNA, ATP, NADH, and other important biomolecules) [74].
- Glycine has been experimentally found to provide the central C2N subunit of every purine [73].
- Isoleucine has been noted for its role in the citric acid cycle – its carbon skeleton is convertible into succinyl CoA, to be sent into the citric acid cycle, oxaloacetate, to be sent into gluconeogenesis, and it is convertible into acetyl

CoA, to be sent into the citric acid cycle – which are significant in providing cells with (chemical) energy (in the form of adenosine triphosphate) [75].

- Methionine has been noted for being encoded in the most prevalent start codon – meaning that methionine is usually in the protein’s N-terminal position (the end of a protein’s main chain which displays a free amino group) [76].
- Proline has been noted for its prevalence as the first residue in alpha helices (a secondary structure of proteins which is a helix wherein every amine group donates a hydrogen bond to the backbone carbonyl group situated four residues – or four monomers within the protein – earlier) and as the edge strands in beta sheets (a secondary structure in proteins which is a twisted, possibly pleated, sheet made up of beta strands – stretches of polypeptide chains often three to ten amino acids in length – linked by a minimum of two/three backbone hydrogen bonds) as well as its prevalence in the turns of proteins due to its change in entropy (when going from an unfolded form to a folded form) being smaller than that of other amino acids [77].

According to the characteristics of cancer cells, they can, in a naïve but intuitive sense, be viewed as hyperactive versions of normal cells – they reproduce faster, they live longer, and they take up more nutrients. As such, the required concentration of leucine or valine, in combination with their products, might be expected to see an increase when comparing their concentrations in normal cells and in the corresponding cancerous cells.

While this seems to survive initial scrutiny – as seen in specific cases concerning serine and glycine [78], [79], glutamine [80], valine [81], arginine – as implied by [82] – proline [83],

methionine [84], isoleucine and leucine [85]–[89], and alanine [90] — the evolution of cancer cells usually involves more mutations than those of tumorigenesis, so that the behaviors of any particular species may be more complex than these expected concentration increases [60].

Still, as tumors tend to be heterogeneous in their makeup, to the extent that the characteristics of cancer seem, at present, to be their only common factors, this dissertation shall not be overly concerned with such “passenger” mutations [91].

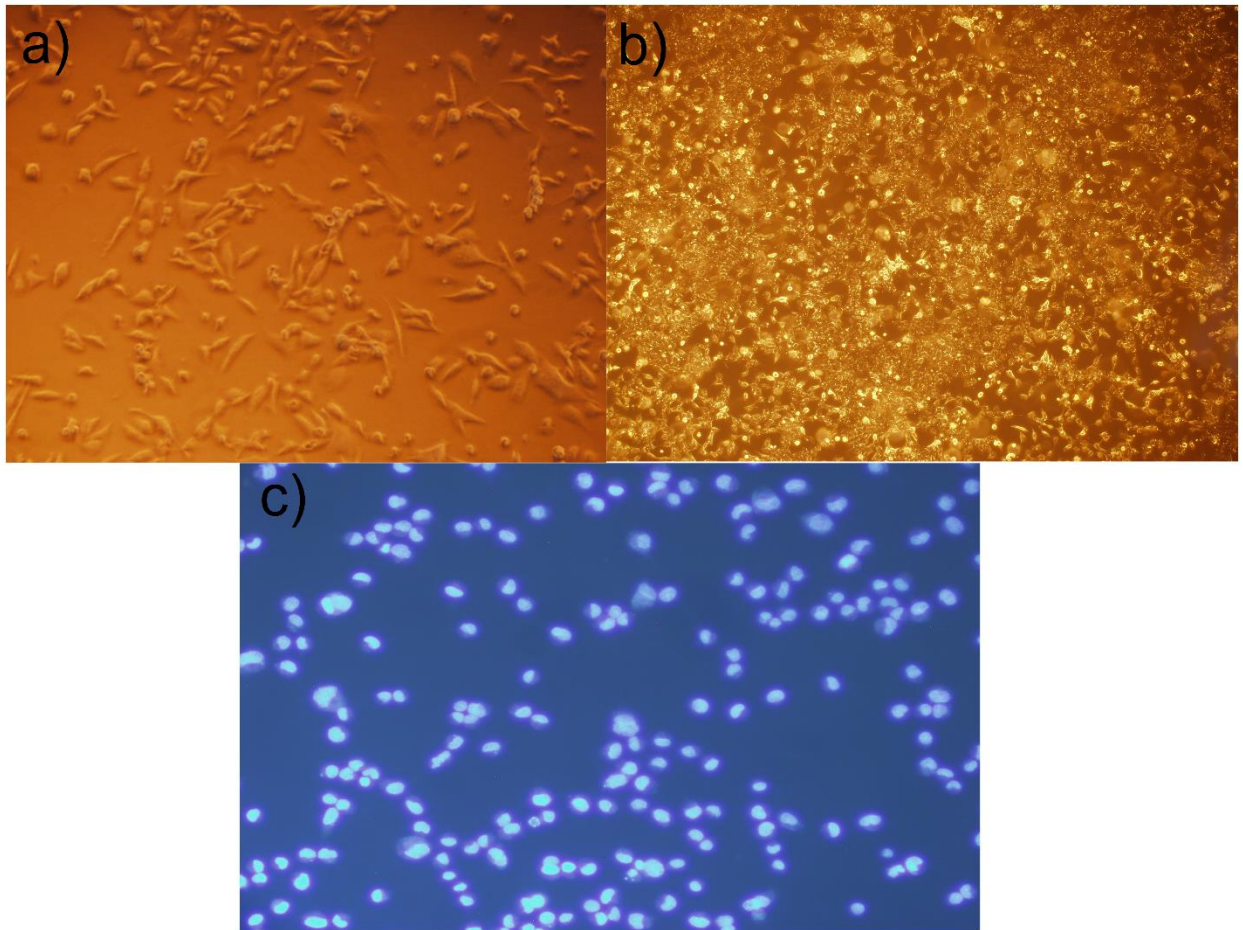


Figure 5: Images of the cell lines: a) PC-3, b) SfXL and c) SfXL such that the SfXL cells in c) were dyed with fluorescent dyes that picked out living (blue) and dead (green) cells. The SfXL cells in c) were imaged using fluorescence spectroscopy.

A cancer cell line (or cell line) is a collection of identical cancer cells that propagate indefinitely *in vitro*. Every time that a sample of a cell line is cultured, or split, the number of passages that it has undergone is said to have increased by one. This is significant because, when culturing a cell line, one must be wary of cancer cells that have a passage number greater than 10 or 20; that is, the higher the passage number associated with a particular sample, the more likely it is that the cancer cells making up the sample have mutated. The cancer cell lines that were used herein are pictured in Figure 5.

Specifically, the last study contained in this dissertation involved *SfXL* (a type of glioblastoma), *PC-3* (a kind of prostate cancer) and a cell line of normal human astrocytes (which was dubbed “NHA”). The inclusion of NHA is significant: comparison of the results for NHA and those of SfXL theoretically allows any statistically significant differences in (in this case) metabolism to be nailed down.

CHAPTER 2

SOLVENT DEUTERATION IN DNP

In this chapter, we discuss the impact of solvent deuteration on DNP. In particular, we shall first, briefly, overview prior results considering its effect upon the hyperpolarized ^{13}C NMR signal intensity and upon the build-up time of this same signal intensity. This shall be followed by an account of our experiment investigating the effect of solvent deuteration upon: ^{13}C spin-lattice relaxation times and the electronic T_{1s} and T_{2s} . We shall end the chapter with a detailed discussion of the results of this experiment.

2.1 Prior Findings

According to Lumata et al., use of a wide ESR linewidth free radical (such as TEMPO, galvinoxyl or DPPH) in combination with glassing solvent deuteration results in between a 2- and 3- fold rise in the hyperpolarized ^{13}C NMR signal [92]. However, when they tried deuteration a solvent doped with a radical characterized by a narrow EPR linewidth (like trityl or BDPA), they found that the ^{13}C NMR signal decreased relative to the non-deuterated case [92]. When Kiswandhi et al. investigated the effect of glassing matrix deuteration upon both the equilibrium polarization and build-up times of samples doped with either TEMPO or trityl in [93], their results supported the findings of Lumata et al. Furthermore, Kiswandhi et al. found that, upon deuteration, the build-up rates of the ^{13}C DNP intensity doubled [93].

Yet, there do not seem to have been any studies investigating the impact of solvent deuteration upon the ^{13}C T_{1s} in a solution which has undergone DNP. There also do not seem to be any reports concerning such an effect upon the electronic T_{1s} or T_{2s} of the radicals used to dope a sample intended for DNP.

2.2 Methods

All compounds which were used in the experiments discussed herein were gotten through commercial means and were used without further alteration or purification. An Ohaus Discovery DV-215CD semi-micro analytical balance (Ohaus Corporation, NJ) was used throughout this dissertation to accurately measure masses in order to mix with solutions. All masses were measured with the use of 1.5 mL microcentrifuge tubes (Scientific USA, FL) and mixed via a Fisherbrand digital vortex mixer (Thermo Fisher Scientific, MA) for 30 seconds to 2 minutes. This was always followed by placing the microcentrifuge tube(s) into a mini-centrifuge (Thermo Fisher Scientific, MA) and centrifuging for 1-2 seconds in order to ensure the complete volume could be collected. In this particular experiment, sixteen samples were mixed, with a volume of 100 μ L each. Half of these aliquots contained 3 M [^{13}C] sodium acetate and were mixed with either 1:1 v/v glycerol:water or 1:1 v/v deuterated glycerol: D_2O . The other half of said solutions were composed of 2 M [^{13}C] sodium acetate mixed in either 1:1 v/v DMSO: H_2O or 1:1 v/v deuterated DMSO: D_2O . Half of the samples containing glycerol:water were then doped with roughly 15 mM trityl, while the other half were doped with TEMPO. This last division concerning which samples were doped with which radical was repeated for each pair of solvents. Every sample was prepared the day before the experiment and stored in a -20°C freezer until the day of the experiment. On the day of the experiment, the samples were transported to the Advanced Imaging Research Center at The University of Texas Southwestern Medical Center (UTSW). Following transportation, the samples were placed in a $2^\circ\text{--}5^\circ\text{C}$ refrigerator until the beginning of the experiment.

All DNP experiments described herein were performed at UTSW using their HyperSense hyperpolarizer (Oxford Instruments, UK) – a commercial version of the dDNP system built by

Ardenjaer-Larsen et al. This particular system uses a 3.35 T superconducting magnet and is slightly modified by the addition of a roots pump vacuum system (Edwards Vacuum, UK) which is used to reduce the base temperature of the cryostat vacuum space from about 1.4 K to roughly 1.2 K. Furthermore, the HyperSense at UTSW makes use of a 100 mW ELVA microwave source (ELVA-1 Millimeter Wave Division, RU) in order to irradiate the interior of the sample space.

At the beginning of each DNP experiment discussed herein, the DNP sample was transferred into a polyetheretherketone (PEEK) DNP sample cup with a capacity of 200 μ L (Oxford Instruments, UK). This cup was then rapidly placed into the above mentioned HyperSense.

Half of these aliquots were individually polarized via the HyperSense in a manner that allowed the build-up of their polarization to be tracked. This meant irradiating the samples doped with TEMPO (trityl) at 94.105 GHz (94.088 GHz), the frequency at which its DNP spectrum had a P(+) peak. In tandem with this irradiation, the ^{13}C NMR signal intensity was recorded at 180 s intervals until the resulting curves had plateaued. These curves were each fit with the solution to equation (0.12). The NMR tuning box of the HyperSense was then quickly connected to a VNMRS 400 MHz NMR console (Agilent Technologies, CA) via a RG58 coax cable (Harbour Industries MIL-C-17/60C M17/60-RG142 27478, USA) with a SubMiniature version A (SMA) adaptor. This allowed the decay of the ^{13}C NMR signal to be monitored by irradiating the sample with a 2° pulse at 10 minute intervals up until the signal roughly reached zero.

The remaining half of the samples (identical in composition to the first half) were shipped to the National High Magnetic Field Laboratory (NHMFL) in Tallahassee, Florida, where they underwent EPR measurements. Specifically, ESR was performed in the W-band (which is the

name of the electromagnetic spectrum between 75 and 110 GHz) on a Bruker E680 EPR spectrometer (Bruker Biospin, Billerica, Massachusetts). This particular spectrometer made use of a Bruker TE₀₁₁ cylindrical cavity and a CF1200 helium flow cryostat (Oxford Instruments, UK) in order to manipulate the temperature of the sample cavity. With this system, the temperature dependence of the electronic spin-lattice and spin-spin relaxation rates of the trityl or TEMPO were recorded via saturation recovery. The temperature dependence of the ESR spectra of these two radicals was also determined by way of the field-swept electron spin-echo method (a method which refocuses the magnetization associated with spins via an electromagnetic pulse).

All data herein were analyzed, graphed and arranged with the use of Igor Pro version 6.2 (Wavemetrics, OR). All ¹³C decay data presented in this dissertation were acquired with VNMRJ software (Agilent Technologies, CA) and were analyzed first with an ACD Labs NMR processor (Advanced Chemistry Development, Canada) before undergoing analysis with Igor Pro. The build-up and decay curves were fit using equations (0.9) and (0.10), respectively. The ESR saturation recovery data were fit with a double exponential with the condition that whichever time constant was longer would represent the spin-lattice relaxation time of the electron, whereas the greater rate correlates with effects of electron-electron cross-relaxation. The temperature dependent electronic T_{1s} were then plotted together and the resulting curves were piece-wise fit with equation (0.4) to determine the coefficient β in different temperature intervals.

2.3 Results and Discussion

Throughout much of this dissertation, the relative ^{13}C DNP intensities were used as a measure of the relevant ^{13}C DNP efficiencies. This may be considered reasonable since these relative DNP intensities are proportional to the absolute polarizations [94]–[97].

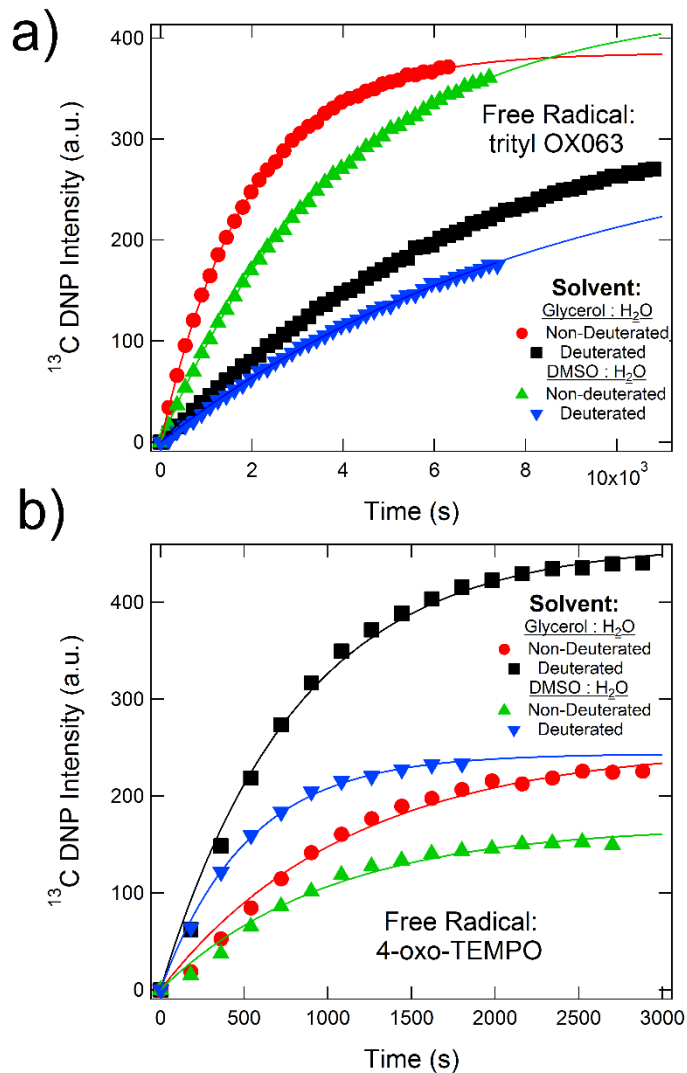


Figure 6: ^{13}C DNP build-up data of $[1-^{13}\text{C}]$ sodium acetate dissolved in one of four solvents such that the samples depicted were doped with a) trityl or b) TEMPO.

The build-up curves of [1- ^{13}C] acetate doped with either trityl or TEMPO, shown in Figure 6, further confirmed the results of Kiswandhi et al. [93] and Lumata et al. [92].

That is, as evident from Figure 6, glassing matrix deuteration led, in the case of trityl-doped samples, to reduced equilibrium polarizations and longer build-up times; meanwhile, when the solutions were doped with TEMPO, deuteration of the solvent resulted in increased magnetization maxima and faster build-up rates. Both of these results were previously explained by Lumata et al. [92] and Kiswandhi et al. [93] via noticing that, according to equation (0.11), the heat capacity of the nuclear Zeeman reservoir is proportional to the square of the gyromagnetic ratio. This means that if the heat capacity is $C_{NZ}({}^{13}\text{C}) + C_{NZ}({}^1\text{H})$, then replacing $C_{NZ}({}^1\text{H})$ by $C_{NZ}({}^2\text{H})$ will reduce the overall capacity because ${}^2\text{H}$ has a lower γ than ${}^1\text{H}$; on the other hand, if the heat capacity is given by $C_{NZ}({}^{13}\text{C})$, then adding $C_{NZ}({}^2\text{H})$ will increase the capacity. In the first instance, thermodynamics has that the smaller capacity will mean it will be easier to decrease the spin temperature of the resulting nuclear Zeeman system. In the second case, thermodynamics says that a higher heat capacity translates into a more difficult time decreasing the spin temperature. What separates these two cases is that, in the first, TM applies to both the ${}^{13}\text{C}$ and ${}^1\text{H}$ systems whereas, in the second, TM applies only to ${}^{13}\text{C}$. This is an instance in which the ESR linewidth of the radical is a determining factor: TEMPO has a sufficiently wide linewidth that it spans the Larmor frequency of the ${}^1\text{H}$; trityl though, has a narrower linewidth which only spans the Larmor frequency of ${}^{13}\text{C}$. Thus, when the sample is doped with TEMPO, TM applies to both ${}^1\text{H}$ and ${}^{13}\text{C}$ nuclei, but, when the sample is doped with trityl, TM applies only to the ${}^{13}\text{C}$ nuclei.

As mentioned in section 2.2, the acquisition of build-up data was quickly followed by tracking the decay of the ${}^{13}\text{C}$ NMR signal intensity of each sample. When doped with trityl, the

[1- ^{13}C] acetate decay data was significantly altered when deuterated, as seen in Figure 7 a). This occurred because the heteronuclear dipolar interactions between the glassing matrix and the ^{13}C nuclei, being proportional to $(\gamma_{^{13}\text{C}}\gamma_B)^2$ with $\gamma_{^{13}\text{C}}$ the gyromagnetic ratio of ^{13}C and γ_B the γ of nucleus B [98], decreased in magnitude with deuteration of the solvent. As such, deuteration led to the magnetic field fluctuations shrinking. In turn, this meant that the nuclei in the lower Zeeman energy level were less often exposed to photons containing sufficient energy to cause a spin-flip. As such, the ^{13}C nuclei tend to stay in the lower Zeeman energy level for a greater span of time.

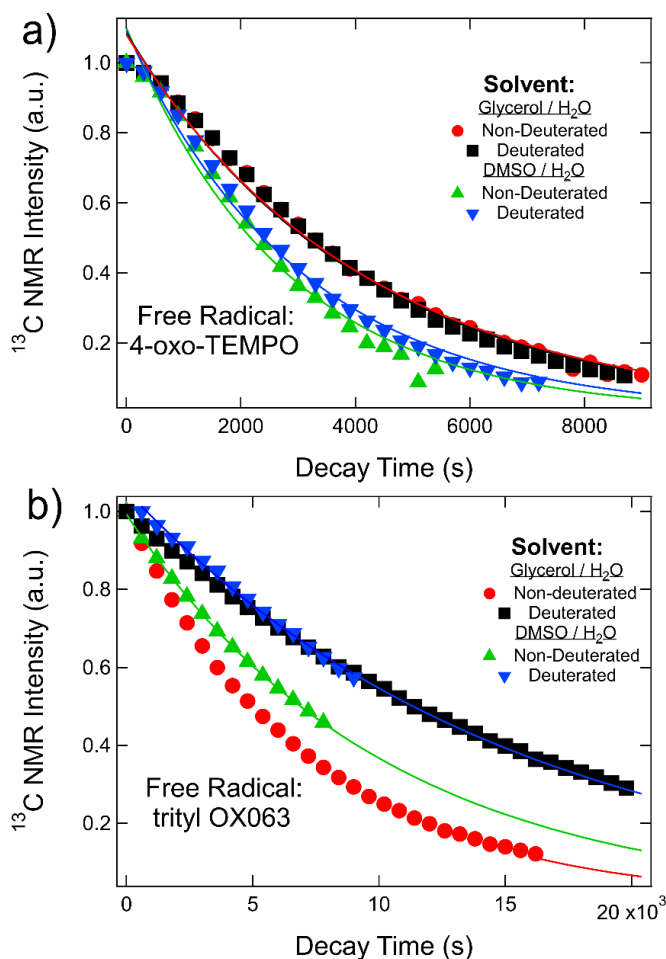


Figure 7: Data representing the decay of polarized ^{13}C NMR signals of [1- ^{13}C] acetate dissolved in one of four solvents and doped with a) 15 mM trityl or b) 40 mM TEMPO.

Now, T_1 describes a return to thermal equilibrium and thermal equilibrium here means that the two Zeeman energy levels contain roughly the same number of nuclei. Hence, this means that, upon deuteration, the rate of spin-lattice relaxation decreases for spins relaxing from the lower energy state to the higher Zeeman state. Therefore, deuteration of the solvent would be expected to result in a lengthening of the T_1 as compared to in the absence of solvent deuteration.

Now, as the above explanation should still apply when the samples were doped with TEMPO, we run into an apparent conundrum: Why do the decay curves in Figure 7 b) display nearly no change in their relaxation rate upon deuteration? The key to answering this question lies in the concentration of TEMPO used: the (optimal) concentration of TEMPO which was used was more than double that of trityl. This meant that there were more than double the concentration of paramagnetic ions and, so, the magnetic field fluctuations felt by the ^{13}C nuclei were much greater than those felt in the case that trityl was the dopant. As such, there were then more opportunities for the ^{13}C nuclei to absorb photons carrying energy on the order of the ^{13}C Larmor frequency. Hence, by a similar argument as outlined in the preceding paragraph, when the dopant is TEMPO (such that the optimal concentration is used) we would expect the average ^{13}C spin-lattice relaxation time to decrease to a lesser extent upon deuteration than would happen when using a (much) lower radical concentration. Therefore, one may qualitatively explain the results in Figure 7 based upon the current theory of relaxation in NMR involving heteronuclear dipolar coupling [98].

W-band ESR data was collected for both TEMPO and trityl at low temperatures by monitoring the EPR signal intensity as the frequency was varied at different temperatures. This was done in order to determine the effect of solvent deuteration upon the electronic T_1 s and T_2 s of

both radicals when dissolved in one of the four glassing matrices used in this particular experiment. The results are displayed in Figure 8. The ESR spectra gathered for trityl and for TEMPO, seen in Figure 8 a) and b), respectively, practically overlap. This suggests that deuteration did not have a significant effect on the ESR spectra at temperatures around 7.5 K. Furthermore, these results beg the question if, perhaps, glassing matrix deuteration in this scenario had no significant impact upon the EPR characteristics of trityl and TEMPO.

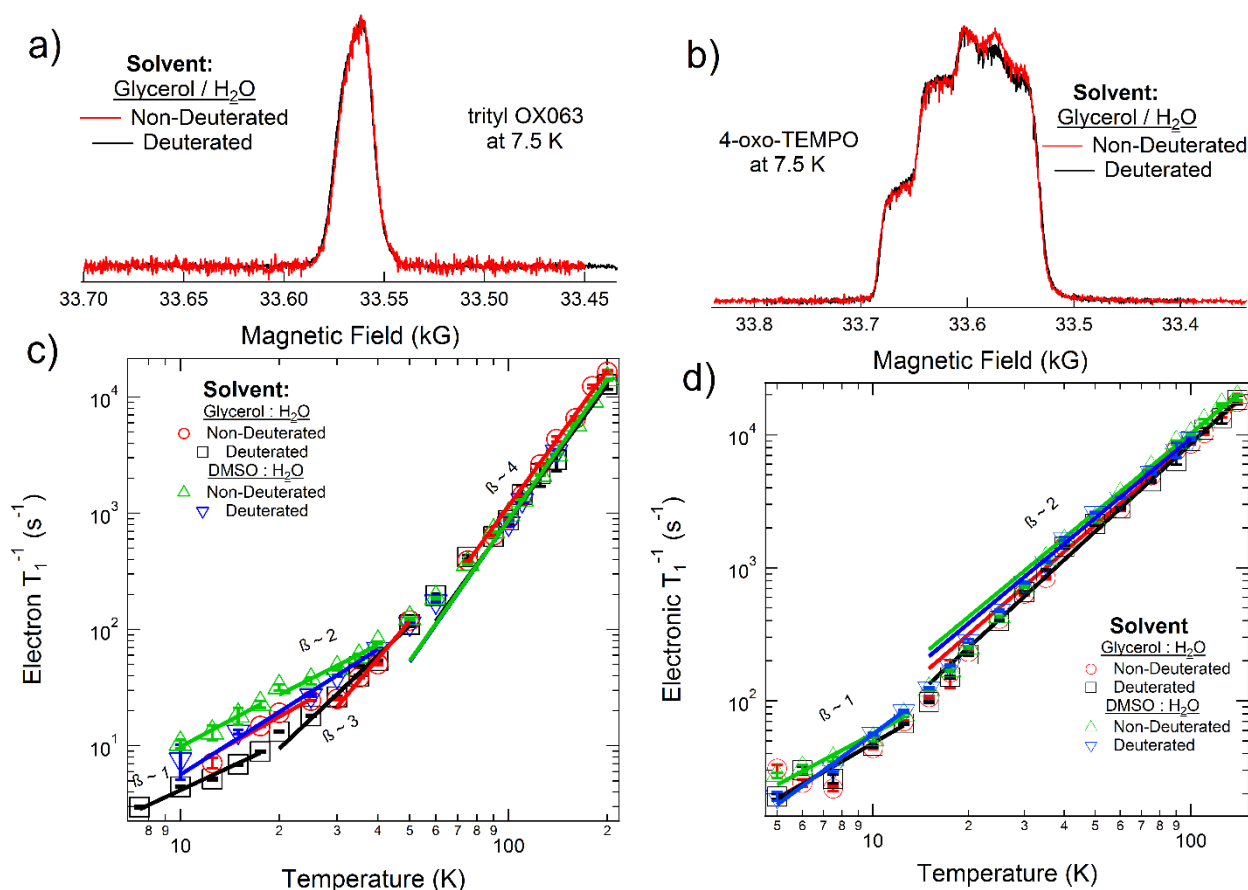


Figure 8: Top: The W-band frequency-swept ESR spectra of a) 15 mM trityl or b) 40 mM TEMPO dissolved in deuterated or non-deuterated variants of 1:1 v/v glycerol/H $_2$ O recorded at 7.5 K. Bottom: The electronic spin-lattice relaxation rates of c) 15 mM trityl or d) 40 mM TEMPO dissolved in one of four solvents and measured at varied temperatures between 5 K and 140 K.

This last possibility was inspected by finding the electronic spin-lattice relaxation rates, in terms of temperature, as described in section 2.2. As seen in Figure 8, bottom, the electronic longitudinal relaxation rates of neither c) trityl nor d) TEMPO showed significant differences upon deuteration. Such a lack of response in the electronic T_1 s and spectra may be explained once again by considering the magnitude of magnetic field fluctuations (since these fluctuations are largely responsible for energy exchanges between Zeeman energy levels): Said fluctuations of a field emanating from a magnetic dipole are proportional to the magnetic moment of the dipole [6]. Moreover the magnetic moment of a particle is proportional to the gyromagnetic ratio of said particle [2]. Now, trityl and TEMPO are molecules with the net spin of an electron – a particle that has a gyromagnetic ratio of $\gamma_{electron} = 28,025 \text{ MHz/T}$. In comparison, nuclei like ^1H and ^2H have much smaller gyromagnetic ratios: $\gamma_{^1\text{H}} = 42.577 \text{ MHz/T}$ and $\gamma_{^2\text{H}} = 6.536 \text{ MHz/T}$, respectively. As such, the difference between the Zeeman energy levels corresponding to the radicals is three to four times greater than the magnetic field fluctuations that can be produced by either the protons or the deuterons. This translates into the fact, illustrated in Figure 8, bottom, that deuteration should not significantly affect the T_1 s of free radicals.

Moreover, as seen in Figure 8 c), above 60 K, the T_1^{-1} s of trityl follows a $\beta \sim 4$ temperature dependence. This suggests that, at such temperatures, the 2-phonon Raman and Orbach processes dominate the relaxation of trityl [13], [14]. Between 20 K and 60 K, the spin-lattice relaxation rates of trityl obey either a $\beta \sim 3$ or a $\beta \sim 2$ temperature dependence, implying that, in this temperature regime, the relaxation of this radical behaves according to either the 2-phonon Raman process or both the 2-phonon Orbach and Raman processes [13], [14]. Above 15 K, the T_1^{-1} s of TEMPO

demonstrate a $\beta \sim 2$ temperature dependence as is demonstrated in Figure 8 d). Just as with the trityl T_1^{-1} s around this temperature regime, this means that, in this region, the mechanism of relaxation for TEMPO is the 2-phonon Raman process [13], [14].

Below 17.5 K or 15 K, the electronic relaxation rates of trityl, respectively TEMPO, obey a $\beta \sim 1$ temperature dependence. This implies that the 1-phonon direct process is the most likely mechanism underlying relaxation of these two radicals in this region of temperature [13], [14]. Now, 5 K was the base temperature of the EPR cryostat, so the electronic relaxation rates could not be determined below this temperature. However, based upon these power law trends, it is reasonable to expect that these relaxation rates will continue to be described by the direct process at temperatures less than 5 K. This means that, at cryogenic temperatures, just the two-state electron Zeeman system is needed to return excess heat to the lattice via phonons. In this manner, the electron Zeeman reservoir is able to reduce its spin temperature. According to Figure 8, at higher temperatures 2-phonon processes are needed for a correct description of the longitudinal relaxation rates of TEMPO and trityl. As such, at higher temperatures, the spin system would require more than two energy levels in order to radiate excess heat to be absorbed by the lattice. The need for at least three energy levels is incompatible with the spin-half Zeeman system composed of but two energy levels. However, the data in Figure 8 demonstrate that, in this experiment, trityl and TEMPO require but two energy levels in order to deposit extra energy in the lattice. Therefore, the findings of Figure 8 are consistent with the expectation that TM applies to the mono-radicals TEMPO and trityl at 1.2 K.

CHAPTER 3

THE EFFECT OF INTERMOLECULAR DEUTERATION AND ¹³C LOCATION UPON DNP

In the prior chapter, we discussed the effect of deuteration of the glassing matrix. Building upon this thought that deuteration may change the outcome of DNP, in this chapter, we describe the impact of deuteration of the ¹³C labeled compound as well as the influence of altering the location of the ¹³C isotope within said compound upon DNP. With this purpose, we first quickly review prior studies concerning the impact of varying the location of the isotope upon the ¹³C DNP and the role of acetate in (cancer) cellular metabolism. Secondly, we shall describe the experiment. Finally, we shall discuss in detail the results of this experiment. All data (and much of the information) in the last two sections of this chapter were reproduced from [99] C. Parish, P. Niedbalski, A. Kiswandhi, and L. Lumata, “Dynamic nuclear polarization of carbonyl and methyl ¹³C spins of acetate using 4-oxo-TEMPO free radical,” *J. Chem. Phys.*, vol. 149, no. 5, p. 054302, Aug. 2018, with the permission of AIP Publishing.

3.1 Background

In a similar prior study by Niedbalski et al., it was found that the maximum ¹³C magnetizations of various isotopic permutations of acetate were correlated with the solid-state ¹³C longitudinal relaxation times of these same variations when trityl was used as the radical [94]. The experiment discussed below differs from the study by Niedbalski et al. in that, here, the polarizing agent was TEMPO as opposed to trityl which was used in [94]. The difference lies in the concentration of the radical which results in optimal DNP, the EPR linewidth of the radical used and the nuclei which said radical can hyperpolarize.

Optimal DNP with trityl requires an electron concentration of between 15 and 20 mM [35], whereas that with TEMPO requires roughly 40 mM [37], [100]. This TEMPO concentration is at least double that of the optimal trityl concentration, meaning that, as discussed in the previous chapter, the use of TEMPO may lead to higher magnetic field fluctuations.

Additionally, the EPR linewidth of TEMPO is much greater at 3.35 T and 1.4 K than that of trityl. In particular, TEMPO has a linewidth that encompasses the Larmor frequencies of ^1H and all nuclei with lower magnitude gyromagnetic ratios. On the other hand, trityl has an EPR linewidth which just manages to encompass the Larmor frequency of ^{13}C and, so, all nuclei with smaller magnitude γ s. This means that, while TM applies to all nuclei with Larmor frequencies less than that of ^1H when the sample is doped with TEMPO, TM only applies to nuclei with Larmor frequencies less than that of ^{13}C when the sample is doped with trityl.

These differences between trityl and TEMPO demand that the two cases be treated as entirely separate, with quite possibly different results.

Now, acetate was chosen because of its frequent use in the DNP community. In turn, this is because of its significance in the metabolism of acetyl coenzyme A via the enzyme acetyl coenzyme A synthetase [101]. Acetyl coenzyme A is a supremely important compound used in the citric acid cycle [63], for fatty acid synthesis and metabolism [101], in the production of steroids [102], etcetera. As such, cancer cells, being hyperactive in their reproduction, would be expected to require greater concentrations of acetate than their regular counter-parts. Additionally, the brain readily absorbs acetate and the only cells that metabolize it in that region are the astrocytes [103]. This means that ^{13}C -labeled acetate is a promising bio-molecule for investigating cancer and, perhaps especially, glioblastoma. Since cancer is a leading cause of death world-wide,

this weakly suggests that a (slightly) greater percentage of researchers are interested in investigating and, in particular, treating it.

3.2 The Experiment

Three samples of 3 M ^{13}C -doped sodium acetate (Cambridge Isotope Laboratories, MA) in 100 μL of 1:1 v/v glycerol:H₂O were mixed for each variant of acetate. The carbon-13-enrichment of each sodium acetate variant were an element of the following list: [1- ^{13}C], [2- ^{13}C], [1- ^{13}C , $^2\text{H}_3$], [2- ^{13}C , $^2\text{H}_3$], [1,2- ^{13}C] and [1,2- ^{13}C , $^2\text{H}_3$] (Cambridge Isotope Laboratories, MA). Every aliquot was then doped with 40 mM TEMPO (Sigma-Aldrich, MO). These 18 solutions were mixed in eighteen 1.5 mL microcentrifuge tubes (Scientific USA, FL) via two minutes on a digital vortex mixer (ThermoFisher Scientific, MA) at least 12 hours prior to the experiment and stored in a -80° C New Brunswick U101 ultra-low temperature freezer (Eppendorf, NY) until the experiments were to begin. Prior to use, each sample was centrifuged for one to two seconds via a mini-centrifuge (ThermoFisher Scientific, MA) in order to ensure all the solution was at the bottom of the centrifuge tube.

The HyperSense used for this experiment was as discussed above (see section 2.2) and operated at 3.35 T and 1.4 K [104, p. 2].

The ^{13}C DNP build-up curve was measured per sample with the aid of a small flip angle radiofrequency pulse emitted at 180 second intervals. This was accomplished via the use of software built into the HyperSense. Now, when the polarization of the doubly-carbon-13-labeled permutations were recorded, the methyl and carboxyl ^{13}C NMR intensities tended to double over each other. As such, the area under their combined polarization peak was determined by integration. Yet, the strong dipolar contact between these two nuclei suggested that the polarization

of the two would rapidly equalize. In other words, one should be able to treat the polarization of each ^{13}C in a doubly labeled acetate as roughly equivalent. This treatment allowed accurate comparison between the doubly labeled and the singly labeled acetates: one must simply divide the net equilibrium polarization of the doubly-labeled acetates by two – the number of ^{13}C spins per molecule. As described above, this buildup data was fit to the solution of equation (0.12).

Once the build-up curves reached their maxima, the microwave irradiation was switched off and, as discussed above (see section 2.2), a coaxial cable was used to connect the NMR tuning box of the HyperSense to a VNMRS 400 MHz NMR console (Agilent Technologies, CA). This was immediately followed by monitoring the decay of the hyperpolarized ^{13}C NMR signal via an array of 1.54° radio-frequency pulses emitted every 300 seconds. The tuning frequency of the HyperSense was 35.908 MHz at the time of this experiment. The full-width at half maximum was recorded to be roughly 10 kHz. Finally, as portrayed previously (in section 2.2), the decay data was fit to equation (0.15).

Averages and their errors (standard deviations) of the solid-state equilibrium ^{13}C DNP polarizations and the longitudinal relaxation times were calculated for each ^{13}C sodium acetate permutation such that each variant had three trials.

3.3 Results and Discussion

As mentioned in the prior section, the build-up curves were acquired first. Figure 8 reveals that the acetates labeled at the carboxyl position, both nondeuterated and deuterated, approximately tied with the acetate labeled at the methyl position, which was also deuterated, for displaying the highest magnetization maxima. Further, the doubly labeled sodium acetates and the

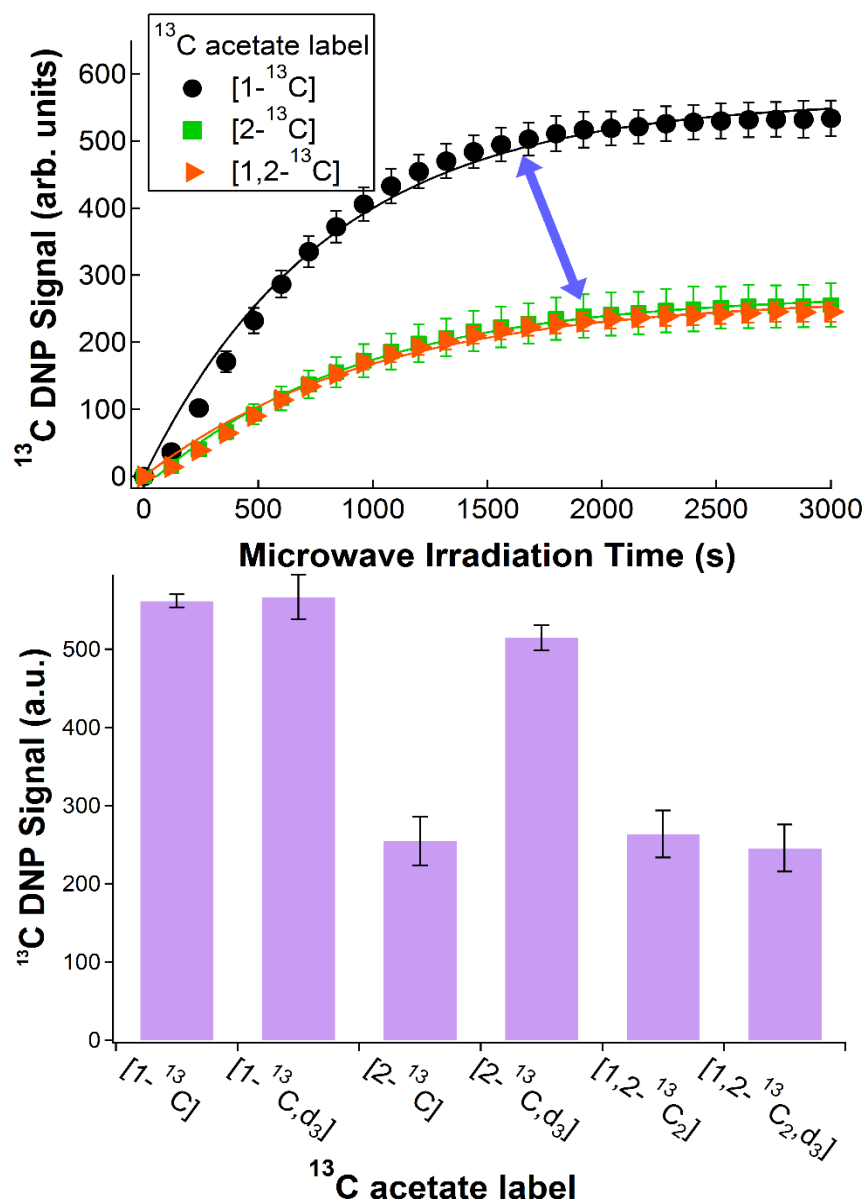


Figure 9: Top: The buildup curves of the non-deuterated ^{13}C -labeled sodium acetates. The arrow emphasizes the difference between labeling sodium acetate in the C1 position as opposed to in the methyl position or to fully enriching the molecule. Bottom: A bar graph displaying the average equilibrium polarizations corresponding to the buildup curves of the different (^{13}C) isotopic permutations of acetate acquired at 3.35 T and 1.4 K with a 100 mW microwave source. The standard deviations were acquired with a sample size of three. The bottom figure was reproduced from [99] C. Parish, P. Niedbalski, A. Kiswandhi, and L. Lumata, “Dynamic nuclear polarization of carbonyl and methyl ^{13}C spins of acetate using 4-oxo-TEMPO free radical,” *J. Chem. Phys.*, vol. 149, no. 5, p. 054302, Aug. 2018, with the permission of AIP Publishing.

acetate enriched at the methyl position (but which went nondeuterated) all had comparable equilibrium polarization – which, curiously, was roughly half that of the other three samples.

As the only significant differences between these samples lies in the isotopic location of (one or more) ^{13}C and in the replacement of protons with deuterons, the results in Figure 9 must be explainable via intra-molecular interactions:

Now, unlike the carboxyl ^{13}C spins, the methyl ^{13}C nuclei are surrounded by protons. As such, the nuclear leakage factor of equation (0.9) is likely higher for the methyl spins. Hence, the methyl spins would be expected to display a lower equilibrium polarization.

Furthermore, deuteration of the methyl group of $[2-^{13}\text{C}]$ acetate led to the ^{13}C polarization nearly doubling. This can be explained by invoking TM followed by using equation (0.11). That is, the heat capacity is lowered when replacing the protons of the methyl group with deuterons so that less energy is needed to affect a change in spin temperature. Thus, one expects that the final spin temperature of $[2-^{13}\text{C}, ^2\text{H}_3]$ acetate would be lower than that of $[2-^{13}\text{C}]$ acetate. Therefore, the equilibrium polarization would be expected to be higher for $[2-^{13}\text{C}, ^2\text{H}_3]$ than for $[2-^{13}\text{C}]$ acetate.

One might expect that this same argument should be applicable to $[1-^{13}\text{C}, ^2\text{H}_3]$ and $[1-^{13}\text{C}]$. Unfortunately, Figure 9 indicates that this is not so. This, at first glance, appears to contradict the observations discussed in Chapter 2, section 2.1. Such a paradox may be resolved by re-examining the concentration of deuterons in the samples involved in this experiment as compared to those involved in [92], [93]. In this study, the concentration of acetate was 3 M whereas the concentration of glycerol was 13 M and that of water was 55 M. As such, the concentration of deuterons in this case was much lower than when the solvents were deuterated in [92], [93].

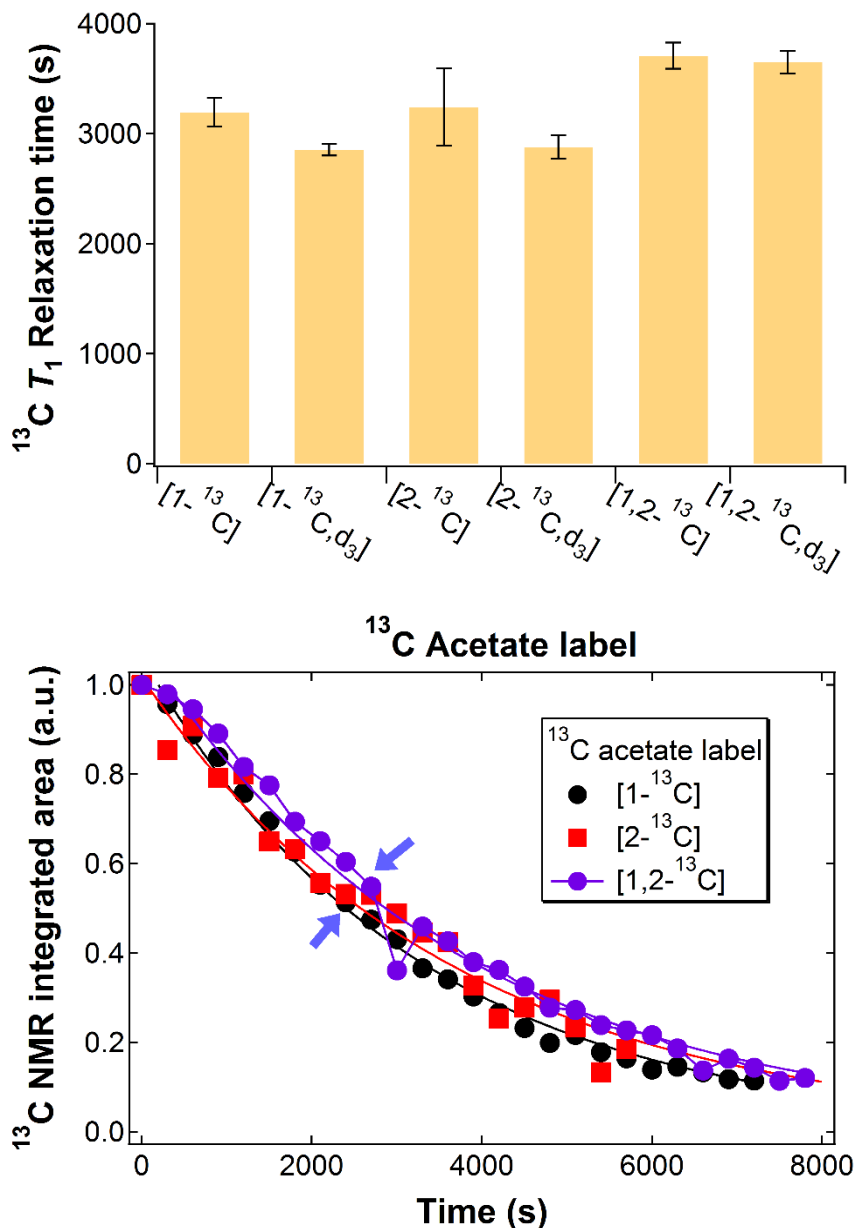


Figure 10: Top: A histogram of the average ^{13}C T_1 s acquired via recording the decay of the ^{13}C NMR signal of permutations of ^{13}C -enriched acetate at cryogenic temperatures and 3.35 T. The data were fitted to equation (0.15) which allowed the loss from spin-lattice relaxation and radio-frequency pulsing to be taken into account. This part of the figure was reproduced from [99] C. Parish, P. Niedbalski, A. Kiswandhi, and L. Lumata, “Dynamic nuclear polarization of carbonyl and methyl ^{13}C spins of acetate using 4-oxo-TEMPO free radical,” *J. Chem. Phys.*, vol. 149, no. 5, p. 054302, Aug. 2018, with the permission of AIP Publishing. Bottom: Example decay data of the non-deuterated acetates. The arrows indicate the lack of a significant difference between the decay data.

This suggests that we resort to a different reasoning behind the significant difference in behavior of [1- ^{13}C , $^2\text{H}_3$] and [2- ^{13}C , $^2\text{H}_3$] as compared to [1- ^{13}C] and [2- ^{13}C]: We instead consider the distance between hyperpolarized nuclei within each molecule.

Note that, when the carboxyl carbon is enriched, the ^{13}C is roughly two bond-lengths away from the protons/deuterons, whereas, when the methyl carbon is enriched, the ^{13}C is approximately one bond-length away from the protons/deuterons. As such, the heteronuclear interactions between the ^{13}C and ^1H or ^2H may be significantly involved in the DNP of the singly ^{13}C -labeled acetate isotopomers, at least when using a radical whose linewidth spans the Larmor frequency of ^1H .

Curiously, when both carbons were labeled, not only did deuteration have a negligible effect upon the nuclear equilibrium polarization, but both demonstrated roughly half the maximum magnetization relative to that of the singly-labeled carboxyl [1- ^{13}C] acetate. This strongly suggests the presence of a powerful homo-nuclear dipolar interaction between the ^{13}C nuclei within acetate [98]. Based upon Figure 9, one might even go so far as to say that doubly-labeling acetate with ^{13}C has an incredibly detrimental effect upon the resulting hyperpolarized ^{13}C NMR intensity.

Once the ^{13}C NMR signal of a sample had roughly plateaued, its decay was monitored in order to attain the corresponding T_1 . The data, shown in Figure 10, demonstrate that, when the samples were doped with TEMPO, there was relatively little variation (which was without statistical significance) in the ^{13}C longitudinal relaxation times upon changing the ^{13}C location or upon deuteration.

As was noted earlier, the concentration of TEMPO required for optimal DNP is at least twice the optimal concentration of trityl (40 mM compared to 15 mM). That, combined with the relative uniformity of the T_1 s displayed in Figure 10 and the enormous γ of electrons suggests

that the paramagnetic contributions from the highly concentrated TEMPO may have masked the contributions of the inter-nuclear dipolar interactions to the ^{13}C spin-lattice relaxation.

Overall, this chapter suggests that, when using 3 M acetate doped with TEMPO i) the acquirable maximum nuclear magnetizations are highly dependent upon the intramolecular magnetic environs of the ^{13}C spins and ii) it is desirable that the concentration of the paramagnetic dopant not be too great, else the resulting magnetic field fluctuations may significantly affect the T_1 of the acetate.

CHAPTER 4

THE IMPACT OF RADICAL MIXTURES ON DNP

In Chapter 3 we found the paramagnetic agent used in DNP to be quite significant. In fact, it was so important that while the use of trityl led to correlations between the equilibrium polarizations of various acetate permutations [94], use of TEMPO saw no correlations between the two whatsoever [99]. Continuing in this vein, in this chapter we discuss how the choice of radicals and, in particular, mixtures of radicals impact the outcome of DNP. With this in mind, we first define magic-angle spinning (MAS) DNP and then briefly summarize the previous DNP studies involving biradicals and monoradical-monoradical mixtures. Then, we shall discuss the two experiments that our group performed to investigate the effect that using a radical mixture had upon DNP. Thirdly, we shall detail the results of these two experiments.

4.1 Biradicals and Radical Mixtures

In liquids, the motion of the constituent molecules are typically isotropic [105]. These isotropic movements can average the anisotropic interactions which means that said interactions will not appear in the spectrum [105]. Such is desirable because these anisotropic interactions tend to broaden the spectrum, making it harder to identify the underlying structure of the sample [105]. However, this is not usually the case with solids. In order to attempt to remedy this, Andrew et al. tried increasing the motion of the elements of a solid sample by rotating it at a high rate of rotations per minute [105], [106]. This method, called MAS NMR, worked best when the angle between the rotation axis and the external magnetic field, θ , was given by $\cos^2 \theta = \frac{1}{3}$, because, at this “magic angle,” the average dipolar Hamiltonian becomes zero and the NMR spectrum narrows [105].

MAS DNP is essentially the combination of MAS NMR with hyperpolarization of the sample via DNP. However, in MAS DNP, the sample is not brought to cryogenic conditions (since that would defeat the purpose of spinning the sample); instead it is subjected to great temperatures and high microwave power [107].

Biradicals and radical mixtures are prevalent electron sources in MAS DNP [108]–[115]. This is because of previous optimization studies demonstrating that using such biradicals or radical mixtures frequently enables the experiment to proceed using lower concentrations of such radicals or radical mixtures [108]–[111]. It should be noted that this use of lower concentrations extends beyond the observation that, for some radicals, one biradical consists of two, connected monoradicals and, so, should need half the concentration: Sometimes, in MAS DNP, one biradical could be used at a concentration producing an optimal response that was less than half that of the monoradical [108], [109]. This also occasionally extends to radical mixtures [110], [111]. Furthermore, these lower optimal concentrations would, in some cases yield better nuclear equilibrium polarizations than those acquired when using a monoradical [108]–[111]. These enhancements are frequently ascribed to the possibility that such radicals may be engineered so that the CE conditions become satisfied [112]–[115].

Yet, one rarely encounters experiments in DNP using biradicals or mixtures doped with multiple monoradicals. This is likely related to the observation that those studies which have investigated such an optimization path have produced mixed results: When Muñoz-Gómez et al. investigated a biradical made up of a TEMPO and a perchlorinated trityl (called PTM-TEMPO), they found that it led to higher DNP polarization and efficiency when compared to the use of pure trityl [116]. Yet, Macholl et al. determined that, despite allowing use of a lower optimal

concentration, doping DNP samples with a trityl biradical resulted in both greater build-up times and a lesser hyperpolarization as compared to the results acquired when doping the DNP sample with the trityl monoradical [36].

Additionally, Pinto et al. found that using a BDPAesterTEMPO biradical in dDNP led to an enhancement of more than 50,000-fold [117]. In [117], Pinto et al. also suggested that the CE mechanism was likely behind this incredible enhancement. Muñoz-Gómez et al., in [116], also tested their PTM-TEMPO with dDNP and determined that, following dissolution, the signal enhancement was better preserved during the transport from hyperpolarizer to NMR magnet.

4.2 Two Experiments

While investigating the impact of mixtures of free radicals, we performed two experiments: In the first, we examined the impact of a TEMPO-trityl mixture upon DNP; specifically, we looked at the consequences of increasing the TEMPO concentration while the sample was already doped with the optimal concentration of trityl. In the second, we considered how simultaneously increasing the concentrations of BDPA and trityl affected DNP. We shall discuss each of the sample preparation, hyperpolarization and EPR components of the experiment involving trityl-TEMPO first to be followed by those of the experiment involving BDPA-trityl. This pattern shall be enforced in the other sections of this chapter as well.

Roughly 24.9 mg of [1-¹³C] sodium acetate (Cambridge Isotope Laboratories, MA) was measured into 23 microcentrifuge tubes (Scientific USA, FL). These were then mixed with 100 μ L of 1:1 v/v glycerol:deionized water (Sigma-Aldrich, MO) so that each tube contained approximately 3.04 M acetate. Said samples were then vortex mixed for 30 to 45 seconds at about 3000 rotations per minute using a Fisher Scientific Digital Vortex Mixer (ThermoFisher Scientific,

MA). Twenty-two (one sample, doped with 40 mM TEMPO, was a control) of these aliquots were then doped with 15 mM trityl (Oxford Instruments Biotoools, MA). These 23 samples were each doped with one of the following concentrations of TEMPO (Sigma-Aldrich, MO): 0 mM (in the case of the trityl controls), 0.5 mM, 1 mM, 2 mM, 3 mM, 4 mM, 10 mM, 15 mM, 20 mM, 30 mM and 40 mM. All samples were sonicated for a minimum of 10 minutes via a Bransonic CPX1800 ultrasonic bath (Bransonic, CT). Each aliquot was prepared at least 12 hours before the experiment and, so, were kept frozen in a -20° C freezer until roughly an hour prior to hyperpolarization.

Additionally, 15 microcentrifuge tubes were prepared such that 13 contained one of the following concentrations of BDPA (Sigma-Aldrich, MO): 5 mM, 5.5 mM, 6.25 mM, 6.88 mM, 7.5 mM, 9 mM, 10 mM, 11 mM, 12.5 mM, 15 mM, 17.5 mM or 20 mM. The remaining two centrifuge tubes were used for controls where one held 20 mM BDPA (and no trityl) while the other contained 20 mM trityl (without any BDPA). Each of these samples were mixed in 100 µL of 1:1 v/v [1-¹³C] acetic acid (Cambridge Isotope Laboratories, MA):sulfolane (Alfa Aesar, MA). These solutions were mixed for 30 seconds by way of a Fisher Scientific Digital Vortex Mixer, after which they were sonicated for ten minutes with a Bransonic CPX1800 ultrasonic bath. All aliquots, other than the controls, were then doped with the same concentration of trityl as they had been doped with BDPA. Every sample was then mixed for 30 seconds and sonicated for 10 minutes. All samples were kept in a -20° C freezer until within hours prior to the experiment.

When the day of the experiment arrived, all samples were moved to the Advanced Imaging Research Center (AIRC) at the UTSW. Upon arrival, all samples were stored in a 2°-5° C refrigerator until the beginning of the experiment. This experiment was performed at UTSW with the use of their HyperSense, which uses a 3.35 T superconducting magnet and is attached to a roots

blower pump vacuum system used to lower the temperature of the cryostat to 1.2 K. Significantly, this HyperSense uses a 100 mW ELVA microwave source which is such that the HyperSense can only record the P(+) peak of the DNP spectrum of sufficiently wide linewidth free radicals (like TEMPO).

Upon loading a sample into the PEEK DNP sample cup, and then into the HyperSense, its ^{13}C hyperpolarized NMR signal was monitored as the irradiation frequency was varied so that we could i) learn the values of the P(+) and P(-) peaks and ii) to identify how the DNP spectra depended upon the variable concentration of the paramagnetic agents. Said DNP profiles were acquired by irradiating the aliquots every 180 seconds at set frequencies, after which we recorded the response of the polarization. All DNP profiles were monitored with either a 5 or 10 MHz step size (depending upon the experiment and identity of the sample). Each DNP spectrum was then normalized to allow comparison. Through this method, we determined that, in the trityl-TEMPO experiment, the P(+) peak of trityl appeared at 94.090 GHz, whereas the P(-) peak of trityl occurred at 94.185 GHz. In the BDPA-trityl experiment, the P(+) peak of the radical mixture happened at 94.10 GHz, while the P(-) peak was determined to shift to greater frequencies as the composition of the radical mixture shifted from solely BDPA to equal parts BDPA and trityl to pure trityl.

^{13}C buildup data was then acquired for each aliquot via irradiation of, in the trityl-TEMPO case, the P(+) and P(-) peaks of trityl and, in the BDPA-trityl case, of the common P(+) peak. The DNP-enhanced ^{13}C NMR signal intensities were then measured every 180 seconds until they plateaued. The resulting curves were fitted with the solution of equation (0.12) so that the buildup times and equilibrium polarizations could be extrapolated.

ESR was then performed upon a total of six samples: Three aliquots were composed of approximately 3 M [$1-^{13}\text{C}$] sodium acetate mixed in 100 μL of 1:1 deionized water:glycerol doped with either 10 mM trityl, 10 mM TEMPO or both 10 mM trityl and 10 mM TEMPO; the other three aliquots were composed of 100 μL of 1:1 v/v [$1-^{13}\text{C}$] acetic acid:sulfolane doped with either 10 mM trityl, 10 mM BDPA or both 10 mM BDPA and 10 mM trityl. EPR was performed (by a collaborator) at the NHMFL using a Bruker E680 ESR spectrometer to examine the behavior of the samples in W-band. This EPR spectrometer has a Bruker TE_{011} cylindrical cavity and a CFR1200 helium flow cryostat so as to alter the temperature of the sample cavity. Such a system allowed us to determine the temperature dependence of the electronic $T_{1\text{S}}$ of the individual radicals and the radical mixtures through use of saturation recovery. The temperature dependence of the EPR spectra of each individual radical (BDPA, trityl and TEMPO) was measured, as well as the ESR spectra of both the BDPA and trityl mixture and the trityl and TEMPO mixture. This temperature dependence was identified with use of the field-swept electron spin-echo method.

Finally, the data was analyzed, arranged and graphed via Igor Pro version 6.2, except that any data involving a P(-) peak was altered so that the sign of the hyperpolarization would be accurate. That is, the HyperSense can only record the magnitude of the polarization. As such, since the polarization acquired when irradiating the sample at the P(-) peak should be opposite in sign to that gotten when irradiating the sample at the P(+) peak, the data retrieved was modified, typically by a sign. The data pertaining to the temperature dependence of the electronic spin-lattice relaxation rates was fit to a double exponential such that the longer time constant was taken to represent the T_1 of the electron [97]. (The shorter time constant is usually ascribed to electron-electron cross relaxation [118], [119].) This allowed the plotting of the electron $T_{1\text{S}}$ versus

temperature that, in turn, led to the (piece-wise) determination of the relevant exponents of equation (0.4).

4.3 Collective Results and Discussion

The hyperpolarized ^{13}C NMR signal intensity was recorded as the irradiating microwave frequency was changed. This allowed acquisition of the DNP spectra for both the trityl-TEMPO samples and the BDPA-trityl aliquots. Although, due to constraints of the HyperSense, we were unable to record the P(-) peak location of TEMPO (due to the limited range of the microwave source), we were able to record the P(+) peak locations of TEMPO as well as both the P(+) and P(-) peak locations of trityl when investigating the mixtures of trityl and TEMPO with varying

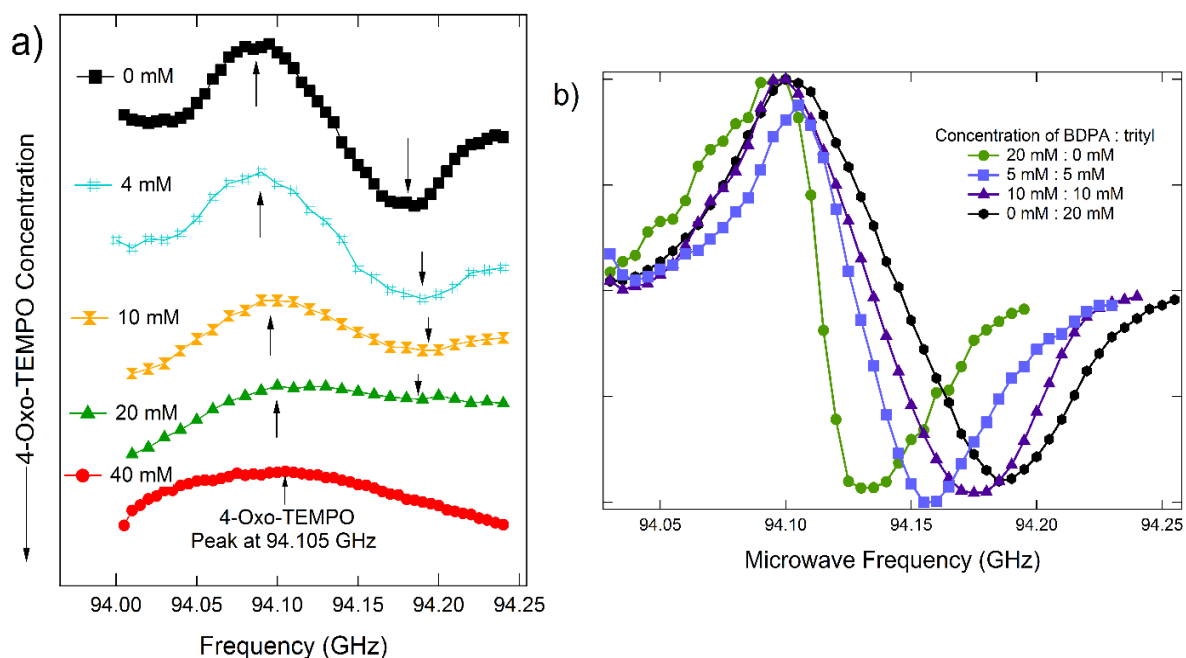


Figure 11: The result of observing the ^{13}C polarization for a given concentration of a) TEMPO in a solution already doped with 15 mM trityl (except for the 40 mM TEMPO, which was not doped with trityl) or of b) equal parts trityl and BDPA while sweeping the irradiation microwave frequency. All results were taken at 3.35 T and 1.2 K.

concentrations of TEMPO. While investigating the mixtures of BDPA and trityl, there were only two peaks per DNP spectrum – the P(+) and P(-) peaks – indicating that the DNP spectra of trityl

and BDPA became superimposed. As noticed in Figure 11 a), increasing the TEMPO concentration resulted in the P(+) peak becoming more and more prominent. Notice that as the TEMPO density rose, the P(-) peak of trityl decreased in size until it became nearly flat around 10 mM. This strongly suggests that there is a concentration of TEMPO at which the P(-) peak vanishes. Such a vanishing likely occurs because the polarization due to the optimal concentration of spin-down trityl paramagnetic centers cancels with the polarization arising from the corresponding density of spin-up TEMPO radicals.

As seen in Figure 11 b), while the BDPA-trityl mixtures shared their P(+) peak, such was not the case with their P(-) peaks. In fact, the location of their P(-) peaks was found to move in the direction of decreasing microwave frequency as the solutions changed from being composed purely of BDPA to being made up of equal parts BDPA and trityl to being pure trityl. The explanation of this effect shall require ESR data concerning the electronic longitudinal relaxation rates. As this data shall be introduced below, we will wait until then to explain the behavior.

With the knowledge of the locations of the P(+) and P(-) peaks in hand, we investigated the ^{13}C hyperpolarization buildups for each sample. Figure 12 a) shows the buildup data acquired when irradiating the samples about the P(+) peak in the trityl-TEMPO experiment. Now, Macholl et al. identified two processes at play in the case of monoradicals that were also in effect for the case of their trityl biradical: The enhanced ^{13}C NMR signal was affected by the density of polarizing agents and by any continuous changes in the average nuclear T_1 [36]. Now, presuming that these two processes also underlie the ^{13}C hyperpolarization involved in radical mixtures, we may put forth an explanation for the decreased polarization seen in Figure 12 a): First, as the solution already carries the optimal concentration of spin-up trityl radicals, the addition of spin-up

TEMPO centers should not lead to a significant change in the polarization. However, as the density of spin-up radicals is increased, there should be more paramagnetic centers about any particular ^{13}C nucleus. Now, a magnetic field about every paramagnetic ion will suffer fluctuations due to the rapid flipping and flopping of the electron spin. Additionally, interactions like dipole-dipole coupling between radicals and between nuclei and radicals lead to more fluctuations in the background magnetic field. These perturbations in the field strength should superimpose. As such, with the rising density of radicals, we expect to observe larger field fluctuations. Hence, the average ^{13}C nucleus should experience greater magnetic field fluctuations. Now, magnetic field fluctuations can be considered masses of (virtual) quanta carrying electromagnetic field energy either away from or towards the source of the field perturbations. Thus, magnetic field fluctuations with energy greater than or equal to that of the ^{13}C nuclear Larmor frequency should increase the probability that the average ^{13}C nucleus transition from one Zeeman energy level to another level. Now, since the samples were doped with an optimal concentration of trityl, most of the nuclei would have been aligned with the external field. This means that the average time interval for which any ^{13}C nucleus would stay parallel to the external field should fall. Therefore, the concentration of spins anti-parallel to the external field was expected to rise, which, in turn, implies that the polarization of the aliquot should have fallen.

Figure 12 b) displays the hyperpolarization buildup curves acquired when irradiating the samples at the P(-) of trityl. After correcting for the fact that the HyperSense only records the magnitude of the polarization, we found that, as the density of TEMPO rose, the equilibrium polarization of the solution also rose (from an initial negative value), passed through zero and plateaued with a positive value. In this particular situation, the rising equilibrium ^{13}C NMR signal

intensity is perhaps most easily explained via the part of the polarization that is affected just by the flipping/flopping of the free radicals – i.e., by the idea underlying DNP as opposed to that affected by the magnetic field fluctuations. That is, since the samples were, in this case, irradiated about the P(-) peak of trityl, the polarization started at a negative value and the average trityl radical was, thus, oriented anti-parallel to the external field. However, as the P(-) trityl peak is closer to the P(+) peak of TEMPO than to the P(-) peak of TEMPO, the mean TEMPO radical added to any sample had its spin oriented oppositely to that of the average trityl radical. As such, the addition of some number of TEMPO radicals then causes one nucleus to flip to being spin-up. Hence, as

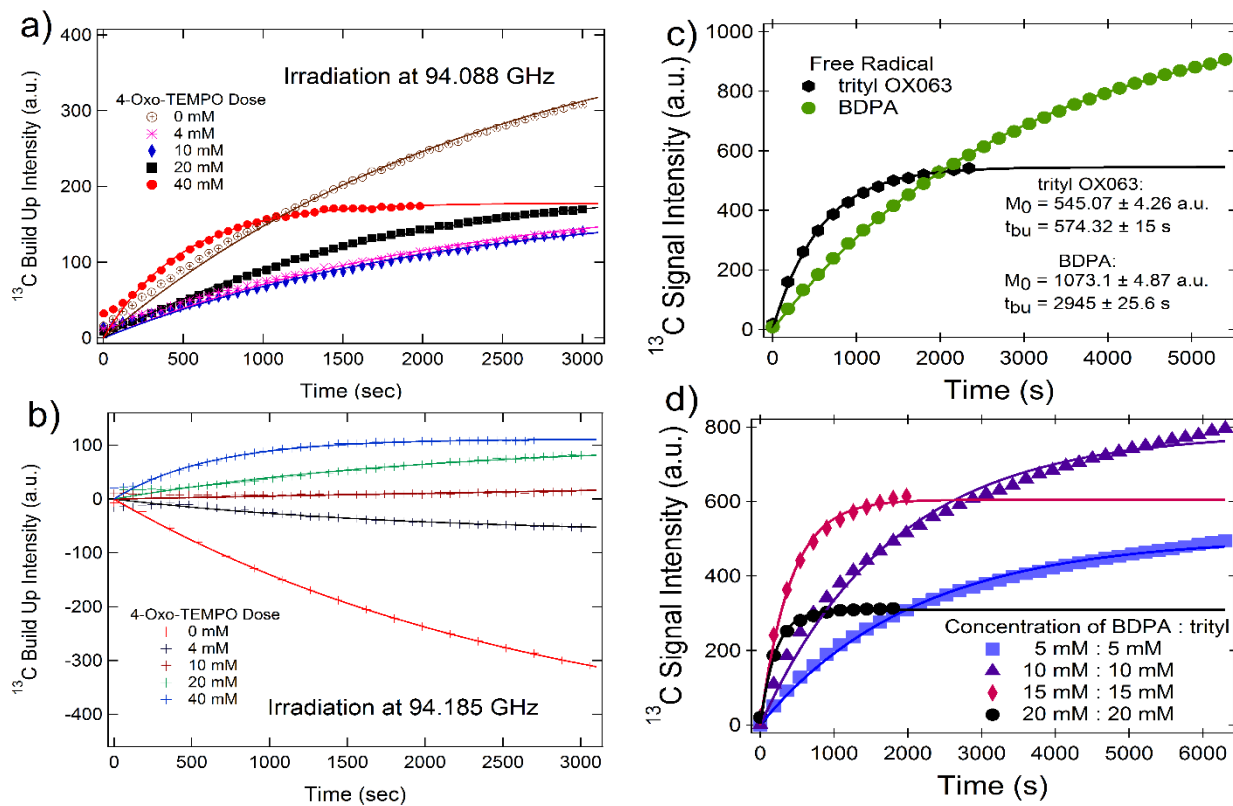


Figure 12: Left: Representative buildup curves of the trityl-TEMPO radical mixture when irradiated at the a) P(+) or b) P(-) peak of trityl. Right: Representative buildups of c) the trityl and BDPA controls or d) of various concentrations of 1:1 trityl:BDPA.

the concentration of TEMPO radicals rises, the density of spin-up nuclei increases until there are roughly equivalent amounts of spin-up nuclei as spin-down nuclei at which point the polarization is approximately zero. This pattern then continues so that the polarization increases from zero until plateauing.

Figure 12 c) displays the buildup data of trityl and BDPA as well as their buildup times and equilibrium polarizations. As shown, trityl had nearly half of the maximum magnetization and roughly a fifth the buildup time of BDPA. Similarly, Figure 12 d) depicts the buildup data of representative samples doped with equal parts BDPA and trityl. The behavior of the buildup equilibrium polarization and buildup times shall be explained momentarily. Here we merely notice [see Figure 12 d)] that use of the 10 mM : 10 mM trityl : BDPA dopant led to the highest polarization whereas use of 15 mM : 15 mM trityl : BDPA dopant resulted in the smallest buildup time interval.

Via fitting the buildup data of Figure 12 we were able to extrapolate the equilibrium ^{13}C polarizations and buildup times. These are shown in Figure 13. In Figure 13 a), we see the magnetization maxima corresponding to the buildup data in Figure 12 a) and b) – i.e., the buildup data corresponding to the experiment involving a mixture of TEMPO and trityl. As such, we refer the reader to the two paragraphs immediately before Figure 12 (the third and fourth paragraphs in this section) for a qualitative explanation of Figure 13 a). Figure 13 b) depicts the ^{13}C buildup time versus TEMPO concentration when the samples were irradiated at the P(+) or P(-) peaks of trityl. Notice that the buildup times fell as the TEMPO concentration increased. Such may be qualitatively explained as follows: as the density of TEMPO radicals increase, the average ^{13}C nucleus is more likely to be closer to some radical. Yet, as discussed above, nuclei that are closer

to radicals experience greater fluctuations in the magnetic field, at least when the spins of the radicals are rapidly flipping and flopping. Nuclei surrounded by more radicals are more likely to receive a photon with enough energy to flip themselves and, significantly, will probably have the chance to absorb a photon characterized by their Larmor frequency more frequently.

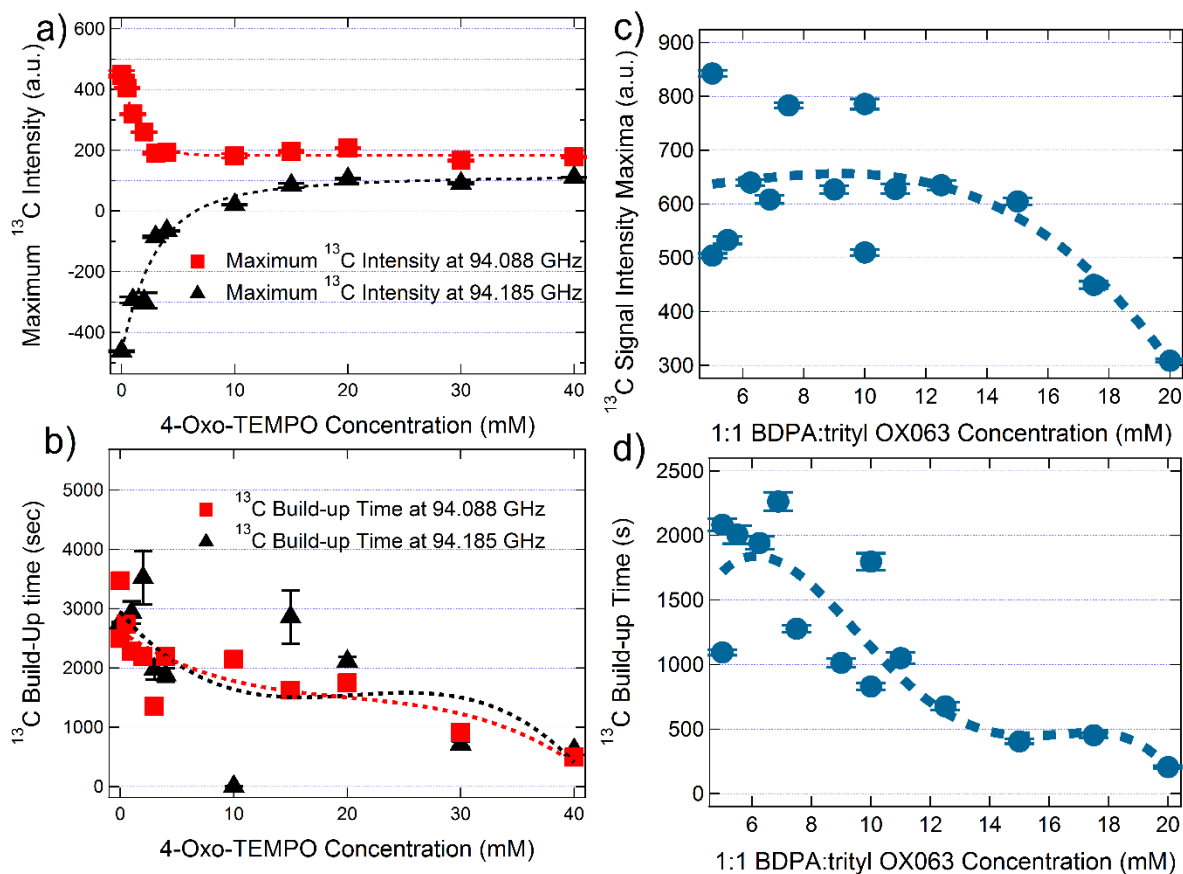


Figure 13: Left: The a) equilibrium ^{13}C polarization and b) corresponding ^{13}C buildup times for the trityl P(+) [black triangles] and P(-) [red squares] peaks acquired for differing concentrations of the TEMPO-dopant. Right: The c) maximum ^{13}C magnetizations and d) ^{13}C buildup times extrapolated from the buildup data gotten for varying dopant concentrations of equal parts BDPA and trityl. The data in part a) was acquired from the corrected buildups, such as those shown in Figure 12 a) and b).

Once the equilibrium polarizations were extrapolated from Figure 12 c) and d), the results were graphed and fit with 4th degree, offset polynomials. Figure 13 c) demonstrates these ^{13}C signal

intensity maxima of the 1:1 v/v ^{13}C acetic acid : sulfolane as a function of the concentration of 1:1 trityl : BDPA. This fit suggests that the concentration of 1:1 trityl : BDPA at which the optimal polarization can be attained is between 10 mM and 12 mM of equal parts BDPA and trityl. After this critical concentration, however, the polarization falls for exactly the same reasons that the equilibrium polarization declines in the case that the sample is doped with a single radical. One such reason is that when the concentration of radicals rises, the amount of volume of the sample which is encompassed by the spin diffusion barrier rises [17]. This means that more nuclei will be within the diffusion barrier where the super-hyperfine interaction prevents spin diffusion to or from said nuclei [11]. Furthermore, as discussed immediately above Figure 13, this rise in radical concentration leads to the average nuclear T_1 falling. This has a negative impact on the net ^{13}C NMR signal intensity.

Figure 13 d) displays the ^{13}C buildup times of 1:1 ^{13}C acetic acid : sulfolane when doped with different concentrations of 1:1 BDPA : trityl. This data was also fit with a fourth degree polynomial. The fit suggests that either 15 mM : 15 mM trityl : BDPA or 20 mM : 20 mM BDPA : trityl has the shortest, and so the best, buildup time. These results may be traced back to the effect of radicals upon the polarization (via spin flips and flops as opposed to their effect via fluctuating magnetic fields). That is, as the radical concentration increases, the number of radicals per unit volume of the sample rises. As such, more ^{13}C nuclei are getting flipped per second within each such volume. Hence, ignoring the contributions from other possible sources of polarization, the increased flipping of spins means a greater gain of ^{13}C NMR intensity in each region. Gaining more and more ^{13}C NMR signal intensity in every unit volume translates into a quickening of the

^{13}C polarization buildup rate. Therefore, the buildup time is expected to decrease, which was indeed seen in this experiment.

Thus, our results demonstrate that, if one were to use the radical mixture 1:1 trityl : BDPA, the optimal concentration would be between 11 mM : 11 mM and 15 mM : 15 mM of trityl : BDPA. Specifically, it was shown that although the 11 mM : 11 mM concentration of trityl : BDPA had the best equilibrium polarization (roughly 800 a.u.), it also had a buildup time of around 1000 s; on the other hand, the 15 mM : 15 mM concentration of BDPA : trityl had the best buildup time (about 500 s) while also having a polarization around 600 a.u. (The concentration that actually had the best buildup time was 20 mM : 20 mM trityl : BDPA – about 250 s; but it had a signal intensity of less than 400 a.u. Due to its poor ^{13}C signal intensity, this concentration was not considered on a competitive basis with the previously mentioned concentrations.) When these buildup times and equilibrium polarizations are compared with those of pure trityl [see Figure 12 c)], one finds that although pure trityl (or BDPA for that matter) would be cheaper, 15 mM : 15 mM BDPA : trityl seems to perform slightly better than either alone. However, as to whether such a small difference is worth the cost of the two radicals probably depends upon the experiment and the resources available to the experimenter.

In an effort to better comprehend the behavior of the radicals, we examined their coupling to the phonons in the lattice via considering the temperature dependence of their spin-lattice relaxation time and we investigated the ESR lineshapes of the radicals both separately and together. The data in Figure 14 b) and d) were placed in log-log scale and piecewise fit to equation (0.4). In all cases, the radical concentrations were 10 mM or, when in a radical mixture, 10 mM : 10 mM.

Figure 14 a) shows the ESR spectra of TEMPO, trityl and a TEMPO-trityl mixture at 10 K. If we presume that TM is applicable, then said EPR spectra may help explain the differences in behavior among the different mixtures of free radicals: Both the Borghini model [equation (0.7)] and modified Borghini models [e.g. equation (0.8)] are heavily dependent upon the ESR lineshape and its magnitude. As seen in Figure 14 a), the EPR lineshape of the mixture of trityl and TEMPO

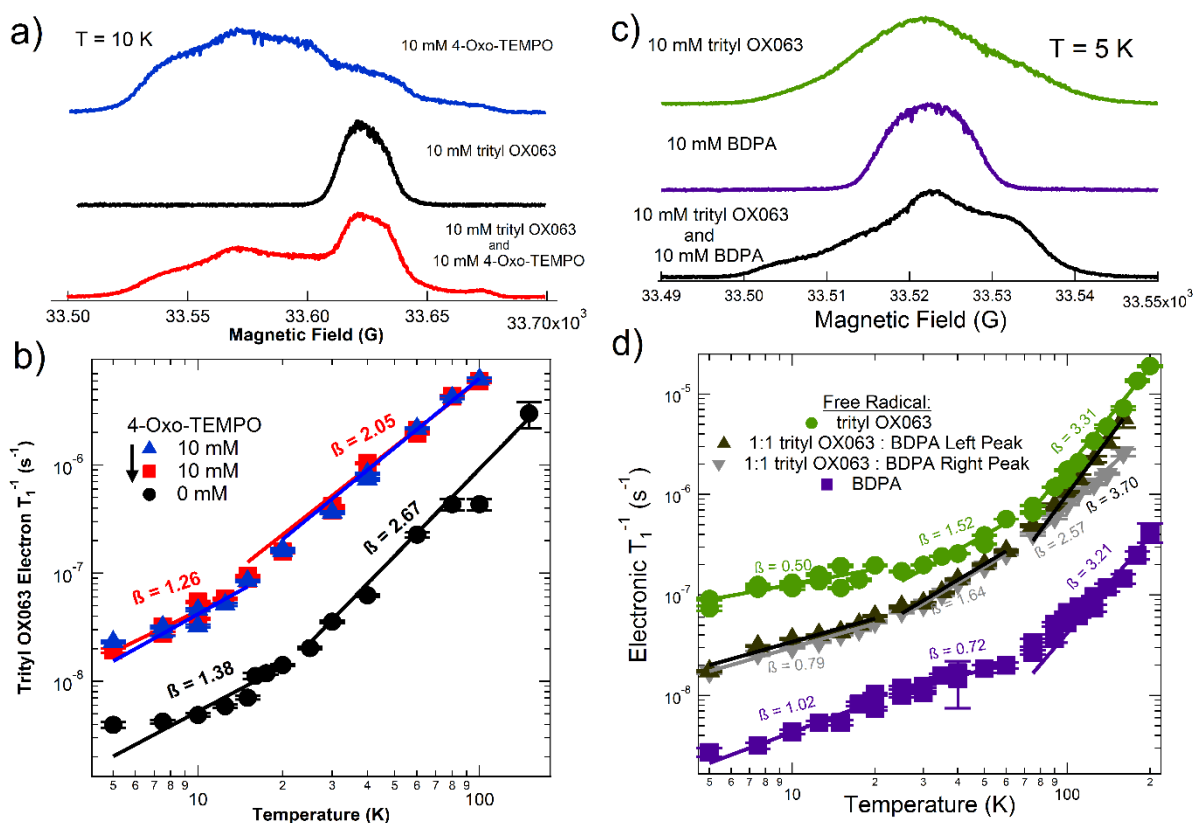


Figure 14: Left: The a) W-band EPR spectra of 10 mM TEMPO (blue), 10 mM trityl (black) and 10 mM : 10 mM trityl : TEMPO (red); and b) the temperature dependence of the electronic spin-lattice relaxation rates of those same dopants in 3 M sodium acetate in 1:1 v/v glycerol : water. Right: The c) W-band ESR spectra of 10 mM trityl (green), 10 mM BDPA (purple) and 10 mM : 10 mM trityl : BDPA (black); and d) the temperature dependence of the radical longitudinal relaxation rates of these dopants in samples of 1:1 v/v [1- ^{13}C] acetic acid : sulfolane. The ESR spectra in a) were acquired at 10 K while those in c) were recorded at 5 K. Additionally, aside from the log-log plots in b) and d), the value of β is given for each fit near the respective fits.

seems to be essentially a superposition of the lineshape of trityl and the lineshape of TEMPO. Thus, adding TEMPO to a sample previously doped with an optimal concentration of trityl impacts the resulting equilibrium polarization. This strongly suggests that the results displayed in Figure 13 a) and b) can be at least partly explained by Borghini's model.

But first, notice that, in Figure 14 b), at temperatures higher than 25 K, the spin-lattice relaxation rate of trityl obeys $\beta \approx 3$ implying that a combination of the 2-phonon Raman and Orbach processes represented the dominant electronic spin-lattice relaxation mechanisms in this temperature range [13], [14]. Meanwhile, when the temperature was less than or equal to 20 K, this relaxation rate for trityl instead followed a $\beta \approx 1$ dependence meaning that the 1-phonon direct process appeared to be the most prominent process within this range of temperatures [13].

When using the TEMPO-trityl radical mixture, it was determined that the electronic relaxation rate above 15 K was proportional to the temperature squared ($\beta \approx 2$). This meant that the 2-phonon Raman process dominated the electron spin-lattice relaxation at such high temperatures [13]. Below 15 K, however, $\beta \approx 1$ so that the direct process dominated [13]. Inspection of Figure 14 b) reveals that the electron spin-lattice interaction occurring in a solution containing TEMPO without trityl obeyed a similar temperature dependence as when trityl was also included.

Now, while the base temperature of the cryostat was 5 K (i.e., we were unable to measure the electronic spin-lattice relaxation rate below 5 K) the fits mentioned above suggest that, below 5 K, $\beta \approx 1$ or $\beta \approx 0$ is still true. This would mean that around temperatures where DNP is performed, the direct process plays the dominant role in the radical spin lattice interactions. Such indicates that, at low temperatures, one only requires the two energy level electron Zeeman system

to interact with the lattice via emitting excess heat as phonons that are then absorbed by nuclei. I.e., at higher temperatures, where two or more -phonon processes are invoked for the electron spin lattice interactions, more than two energy levels would be required for the spin temperature of the radicals to be cooled via transfer of heat to the lattice. If this experiment were to be performed at such higher temperatures, there would then be no way for an electron Zeeman system of just two levels to be cooled by sending heat to the lattice. As such, TM would be inapplicable. However, the data in Figure 14 b) strongly suggests that such is not the case and, so, reinforces the possibility that TM is applicable.

Figure 14 c) depicts the W-band ESR spectra of 10 mM trityl, 10 mM BDPA and 10 mM : 10 mM trityl : BDPA. As with the trityl-TEMPO results, we notice that the EPR spectrum of the radical mixture of BDPA and trityl is essentially a superposition of the ESR spectra of either alone. Now, if we may presume that TM applies to this mixture at about 1.4 K and below, then, according to Borghini (as discussed by Abragam and Goldman in [20]), Wenckebach [27], and Serra et al. [26], [28], [29], the nuclear polarization at equilibrium is heavily dependent upon the EPR lineshape. As such, that the combination of trityl and BDPA is mostly a superposition of either alone suggests that just mixing trityl and BDPA contributes to the equilibrium polarization acquired in DNP.

Figure 14 d) shows a log-log plot of the electronic spin-lattice relaxation rate versus temperature of 10 mM BDPA, 10 mM trityl and 10 mM : 10 mM trityl : BDPA. When considering temperatures greater than 60 K, the relaxation rates of all three samples followed a $\beta \approx 3$ temperature dependence except for the left peak of the mixture which obeyed $\beta \approx 4$. Hence, when considering temperatures above 60 K, all three non-trivial variations of 10 mM trityl or BDPA

display behavior consistent with an electronic spin-lattice relaxation dominated by a combination of the 2-phonon Raman and Orbach processes [13], [14]. Between 60 K and 25 K, the electronic relaxation times of both the 10 mM trityl and the monoradical mixture had a temperature dependence given roughly by T^2 . This means that, in this interval, the 2-phonon Raman process was the predominant mechanism behind the spin-lattice relaxation of trityl and of the trityl-BDPA mixture [13]. The BDPA-doped solution, on the other hand, approximately followed a $\beta \approx 1$ trend. As such, the mechanism behind the spin-lattice relaxation of BDPA was the direct process [13].

At temperatures less than 25 K, the electronic spin-lattice relaxation rates of all of the non-trivial permutations of 10 mM BDPA or trityl were proportional to T^1 ; this means that, between 5 K and 25 K the main mechanism behind the spin lattice relaxation of the radicals was the direct process. Extrapolating this trend implies that it is reasonable to expect that the 1-phonon direct process was dominant at cryogenic temperatures below 5 K – a temperature range which includes that at which DNP is performed. In turn, such suggests that, under conditions conducive to DNP, the electron Zeeman system is able to interact with the lattice without needing either a virtual energy level or both the creation and annihilation of a phonon [11]. This also means that the heat transfer from the electron Zeeman system to the lattice is heavily dependent upon the EPR frequency [11]. Thus, as argued above, the electron Zeeman reservoir is all that is needed to transfer heat to the lattice. Therefore, as there is no need for a more complicated method to dump the excess heat, these results reinforce that TM is applicable.

These modified models of the nuclear polarization by Serra et al. [26], [28], [29], and Wenckebach [27], are all also very dependent upon the radical spin-lattice relaxation rate. As such, the electronic spin-lattice relaxation rates in Figure 14 d) could explain why the P(-) peaks in the

DNP spectra in Figure 11 b) shift towards the P(+) peaks: As shown in Figure 14 d), the radical longitudinal relaxation rates increases by roughly an order of magnitude as the sample dopant goes from pure BDPA to the mixture to consisting of pure trityl. Furthermore, Figure 11 b) shows that the radical with the smallest distance between P(+) and P(-) was BDPA, then the 1:1 BDPA : trityl mixture and then the pure trityl dopant. Now, according to equation (0.8), if the electronic spin-lattice relaxation rate increases, then the rate at which the nuclear polarization changes falls. If the rate at which the nuclear polarization changes falls, then the DNP spectrum is expected to widen. Thus, our results for the electronic longitudinal relaxation rates in Figure 14 d) qualitatively explain the shifting of the P(-) peaks in Figure 11 b).

Overall, that the ESR spectra of a mixture of monoradicals seems to be approximately a superposition of that of either suggests that treating the monoradicals in the mixture as one would treat them if they were the only radical in the sample may be viable. This is, to some extent, supported by the following argument, with which we shall end this chapter.

Furthermore, suppose that we may take Khutsishvili's treatment of the spheres of influence at face value and, hence, expect that, within each diffusion barrier, the nuclear spin-lattice relaxation effects due to other radicals may be ignored [17]. This means that every unit volume may be divided into some number (not necessarily integer) of smaller spheres of influence, each centered about differing radicals, so that the number of divisions is roughly equal to the optimal concentration of that particular radical. (This may be quickly made apparent by considering the definition of concentration of radicals, followed by the definition of optimal concentration with the number of radicals set equal to one, reflecting the requirement that only one radical impact the

nuclei in any sphere of influence: this results in $V_{\text{Optimal}} = \frac{1}{c_{\text{Optimal}}}$ so that

$\frac{\text{unit Volume}}{V_{\text{Optimal}}} = \frac{1}{\frac{1}{c_{\text{Optimal}}}} = c_{\text{Optimal}}$.) Now, from studies on mono-radicals we know that at

concentrations greater than the optimal, the free radicals become so tightly packed that nearby nuclei start to experience more magnetic field fluctuations as well as a greater range of such fluctuations. That is, if we try to fit one radical into a volume, V , smaller than the optimal volume, the corresponding concentration, C , exceeds the optimal concentration (

$c_{\text{Optimal}} = \frac{\text{unit Volume}}{V_{\text{Optimal}}} < \frac{\text{unit Volume}}{V} = c$) which, by the definition of c_{Optimal} , means that the spins

must begin to relax faster. Furthermore, as $V < V_{\text{Optimal}}$, the shapes corresponding to each optimal sphere of influence must intersect at this new concentration. Thus, to some extent, finding an optimal concentration for some free radical may be likened to packing optimal volumes inside some unit volume.

This suggests that, if we may take the optimal concentration of 1:1 BDPA:trityl to be roughly 10 mM : 10 mM [which is suggested by Figure 12 c)], then we can reason as follows: First note that both BDPA and trityl have roughly the same optimal concentration – 20 mM – which suggests that they have similarly sized spheres of influence. In turn, this implies that the maximum number of spheres of influence that can be packed into some unit volume of a glass may remain roughly the same regardless of the percentage of trityl or BDPA in the solution. That is, since both radicals have similar spheres of influence, the optimal concentration should be nearly equivalent to that of either alone. If we suppose that we may approximate this concentration in a radical-

mixture as that of one radical plus that of the other radical, then the optimal concentration of the “single radical” is 20 mM. This strongly suggests that, when mixing equal parts BDPA and trityl, the optimal concentration of the mixture is $20/2$ mM : $20/2$ mM, or 10 mM : 10 mM.

The above hypothesis leads the author to the following two ideas: first to test this hypothesis concerning how to determine the optimal concentration via geometry by mixing together mono-radicals with differing optimal concentrations or by mixing the mono-radicals together in a manner that, though they are not 1:1, their proportion stays constant throughout the experiment; and second to (theoretically) consider how a corresponding packing dimension might apply.

CHAPTER 5

CONCENTRATION DEPENDENCE OF DNP HYPERPOLARIZATION

In the past chapters, we have considered optimization concerning the nature of the radical, the state of deuteration of the solvent and the state of deuteration of the solute; however, we have not so far examined the concentration dependence of the polarization and how such may be used to further optimize a sample for DNP or dDNP. In this chapter, we determined how the DNP polarization changed with a varying concentration. Keeping this goal in mind, we first briefly, but formally, recall DNP-assisted spin diffusion as described by Wenckebach. Then we detail the experiment. Finally, we summarize the results and their implications for optimization purposes.

5.1 DNP-assisted Spin Diffusion

As discussed earlier, DNP-assisted spin diffusion sees the polarization moving away from the free radical in the form of one nucleus flipping such that the resulting photon is absorbed by a nearest neighbor – i.e., the spin appears to perform a random walk directed generally away from the electron [11]. Alone, this suggests that a macroscopic, discrete variant of diffusion applies. To make this discrete notion continuous, one may look to the motion of the quanta involved: The energy, or loss thereof, seems to travel outward (parallel to the apparent motion of the spin-states). As such, one expects that the quanta carrying this electromagnetic field energy travel outward as well. Hence, one may associate to the discrete motion of the spin-states a continuous motion of quanta. Thus, one may ascribe to this random walk a continuous diffusion equation concerning the magnetization (or, more precisely, its field):

$$\frac{\partial}{\partial t} P_S = \sum_{i,j=1}^3 D_{ij} \frac{\partial}{\partial x^i} \frac{\partial}{\partial x^j} P_S \quad (0.17)$$

where P_S is the polarization as in equation (0.3) and D_{ij} are the components of the diffusion tensor [11]. When looking at this kind of spin diffusion in a simple cubic nuclear lattice, $D_{ij} = D\delta_{ij}$ with $D = W_{\text{Flip-Flop}} a^2$ such that a is the lattice spacing and $W_{\text{Flip-Flop}}$ is the dipolar transition probability [11], [16]. Specifically, when the lattice is treated as continuous, $W_{\text{Flip-Flop}}$ is given by:

$$W_{\text{Flip-Flop}} = \frac{1}{16} \gamma^4 \hbar^2 \frac{(1 - 3 \cos^2 \theta)^2}{r^6} \frac{\lambda}{T_2} \quad (0.18)$$

with λ a numerical factor that has an order of magnitude of one, r is the distance between some particular nucleus chosen as the center and other nuclei in the sample and where θ is the angle between the external magnetic field and another nucleus in the sample [16]. In order to correctly represent the flip-flop transition probability felt by the nucleus chosen to be at the center of the coordinate system, $W_{\text{Flip-Flop}}$ must be averaged over all spins. As such, using spherical coordinates, one finds that:

$$\begin{aligned} D &\cong \frac{a^2 \gamma^4 \hbar^2}{16} \frac{\lambda}{T_2} \int_a^\infty \frac{dr}{r^4} \int_0^{2\pi} (1 - 3 \cos^2 \theta)^2 \sin \theta d\theta \int_{-\frac{\pi}{2}}^{\frac{\pi}{2}} d\phi \\ &\propto \frac{\pi \gamma^4 \hbar^2}{48a} \frac{\lambda}{T_2} \\ &\propto \frac{1}{aT_2} \end{aligned} \quad (0.19)$$

where we have treated the volume of the sample as so large compared to $\frac{4\pi}{3} a^3$ that we may approximate the sample as having infinite volume. For this reason we were able to use spherical

coordinates as opposed to the cylindrical coordinates which the shape of the finite PEEK cup would otherwise require.

Regardless, if we suppose that $P_{S,z} \mapsto P$, where P was defined by equation (0.6) and $P_{S,z}$ is the z-component of \vec{P}_S which was defined in equation (0.3), then we may combine equation (0.17) and derivation (0.18) to predict the approximate ratio of buildup rates for two differing concentrations of the same substance: Suppose that the buildup time, τ_{bu} , may be considered approximately the average time needed for any spin-state to diffuse to the edge of the cup with radius r_{cup} . Then, using the discrete variant of equation (0.17) (since we are considering the diffusion of the polarization as opposed to that of the magnetization), we have:

$$\begin{aligned}
\frac{\frac{e-1}{e}}{\tau_{bu}} &= \frac{\frac{e-1}{e} \max P}{\tau_{bu}} \\
&= \frac{P(\tau_{bu}) - P(0)}{\tau_{bu}} \\
&\cong D \frac{P(2r_{cup}) - 2P(r_{cup}) + P(r=0)}{(r_{cup})^2} \\
&= D \frac{P(r=0) - 2P(r_{cup})}{(r_{cup})^2} \\
&= -D \frac{P(r_{cup})}{(r_{cup})^2} \\
&= -D \frac{\frac{e-1}{e} \max P}{(r_{cup})^2}
\end{aligned}$$

$$= -D \frac{e-1}{e(r_{\text{cup}})^2} 1 \quad (0.20)$$

where we used that: $\max P = 1$ in line 1; that the polarization starts very close to zero in line 2; the discrete diffusion equation in line 3; that the polarization outside the cup vanishes in line 4; that the definition of polarization is non-local in line 5 – i.e., that once the polarization has effectively spread throughout the sample, its value is the same everywhere within the sample (it is a macroscopic quantity); that the polarization at the buildup time is, by definition, $\frac{e-1}{e} \max P$ in line 6; and that the maximum possible value of the polarization given by equation (0.6) is unity in the last line. Now, given two copies of derivation (0.19), we may assign to each a different concentration, say concentration C_1 and concentration C_2 . Then, upon dividing the two resulting equations, we get:

$$\begin{aligned} \frac{\left(\tau_{bu}|_{C_1}\right)^{-1}}{\left(\tau_{bu}|_{C_2}\right)^{-1}} &\cong \frac{D_{C_1}}{D_{C_2}} \\ &\approx \frac{a_{C_2}}{a_{C_1}} \end{aligned} \quad (0.21)$$

with C_i the i^{th} concentration for $i \in \{1, 2\}$. Thus, the ratio of buildup rates is related to the inverted ratio of the average distances between the nuclei.

Furthermore, since the lattice spacing changes with the concentration, the average number of ^{13}C nuclei within a sphere of volume $\frac{4\pi}{3} a_{C_i}^3$ is constant for any particular concentration, C_i . As such, we must have that $C_i \frac{4\pi}{3} a_{C_i}^3 = C_j \frac{4\pi}{3} a_{C_j}^3$ for all i and j . Thus, Bloembergen's theory of

spin diffusion predicts that the buildup rates for two differing concentrations are related by way of a ratio of the two concentrations:

$$\left(\tau_{bu|C_1}\right)^{-1} \approx \left(\frac{C_1}{C_2}\right)^{\frac{1}{3}} \left(\tau_{bu|C_2}\right)^{-1}. \quad (0.22)$$

In section 5.3 below, we shall compare this result with experiment.

Now, according to both Horvitz and Wolfe, the free radical – the electron – is the source of spin diffusion [18], [120]. Significantly, this suggests that spin diffusion is generally directed radially away from the radical. Horvitz also concluded that spin diffusion occurs at different rates within and without the spin diffusion barrier – a region about each free radical with radius given by:

$$r \propto \left(1 - 3 \cos^2 \theta\right)^{\frac{1}{3}} \quad [11], [18]. \quad (0.23)$$

Specifically, diffusion within the diffusion barrier is slow whereas such outside the diffusion barrier is fast [18]. Furthermore, according to Hovav, Feintuch and Vega, the polarization of nuclei that are distant from free radicals builds up slower than nuclei that are nearer to the un-paired electrons [50]. This last is especially important since it suggests that the probability that two nuclei, or a nucleus and an electron, exchange a photon carrying their nuclear Larmor frequency is lower the more distant the two particles are from each other. Such is expected considering that the two particles are magnetic dipoles and the electromagnetic interaction between magnetic dipoles is inversely proportional to r^6 [6].

5.2 Methods

We prepared eleven 50 μ L samples which were each doped with 20.4 mM trityl (Oxford Instruments, MA, USA) and a varying concentration of $[1-^{13}\text{C}]$ pyruvic acid (Sigma Aldrich, MO).

The possible (uncorrected) concentrations of [1-¹³C] pyruvic acid were: 0 M (natural abundance), 0.055 M, 0.1125 M, 0.225 M, 0.45 M, 0.9 M, 1.8 M, 3.6 M, 7.2 M, 10.8 M and 14.4 M. Samples at these concentrations were attained by mixing various volumes of 14.4 M [1-¹³C] pyruvic acid with different volumes of unlabeled (i.e., natural abundance) pyruvic acid. 20.4 mM trityl was used because, as the optimal concentration of trityl roughly plateaus between 15 mM and 20 mM [96], use of about 20 mM trityl allowed speedier data acquisition. Each aliquot was mixed immediately prior to the experiment.

The HyperSense used for this experiment was as discussed above (in section 4.2) and operated at 3.35 T and 1.2 K [121].

The ¹³C DNP buildup data was recorded for each sample via a small flip angle radiofrequency pulse sent at 180 s intervals. This was accomplished via a software which comes with the commercial HyperSense. These results were fit with equation (0.12) as described before [122].

After the DNP buildup curves had roughly plateaued, the ¹³C polarization decay curves were acquired as discussed above in section 3.2 and before in [99]. The decay data was fit with the aid of equation (0.15).

The data was analyzed as described in section 2.2. However, the concentrations listed above had to be adjusted to reflect the presence of ¹³C-labeled pyruvic acid in the natural

abundance pyruvic acid by use of: $C_{\text{Corrected}} = C_{\text{NA}} + \frac{V_{99\% \text{ } ^{13}\text{C}}}{V_{\text{Total}}} (\max\{C_{\text{UnCorrected}}\} - C_{\text{NA}})$ with $C_{\text{Corrected}}$

the corrected concentration, C_{NA} the concentration of [1-¹³C] pyruvic acid in unlabeled pyruvic acid (herein this was found to be 0.16 M), $\max\{C_{\text{UnCorrected}}\}$ the concentration of [1-¹³C] pyruvic

acid in the 99% ^{13}C -enriched pyruvic acid (in this experiment this was 14.4 M), V_{Total} the total volume and where $V_{99\% \text{ } ^{13}\text{C}}$ is the volume of 99% ^{13}C -enriched $[1\text{-}^{13}\text{C}]$ pyruvic acid.

5.3 Results and Discussion

As discussed in section 5.2, the buildup data was acquired first; this is shown in Figure 15 a) by way of example buildup curves. Acquisition of the decay curves followed, as depicted in Figure 15 b) which contains representative decay results. The trends represented by Figure 15 a) and b) shall be explained around Figures 16, 17 and 18 in which the equilibrium polarizations per $[1\text{-}^{13}\text{C}]$ pyruvic acid molecule, buildup times and ^{13}C spin-lattice relaxation times, respectively, are plotted versus ^{13}C concentration.

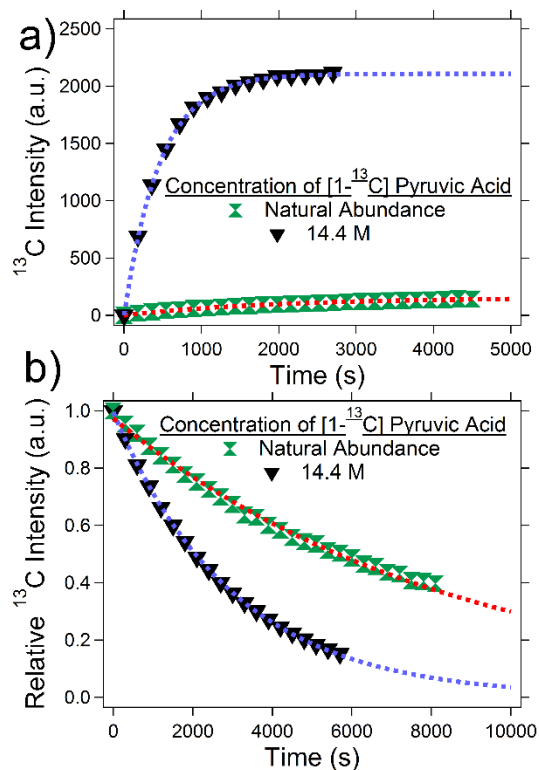


Figure 15: Representative a) buildup or b) decay curves; the extremal concentrations are shown – i.e., 14.4 M $[1\text{-}^{13}\text{C}]$ and natural abundance pyruvic acid (which, when corrected for the presence of 1.1% $[1\text{-}^{13}\text{C}]$ pyruvic acid, becomes 0.16 M). This data was measured at 3.35 T and 1.2 K.

Examination of all the buildup curves [not just those shown in Figure 15 a)] combined with use of approximation (0.21) allowed a comparison of the experimentally acquired ratio of buildup times and the theoretically expected (approximate) values. These ratios are listed in Table 1 such that the first column is composed of the concentrations examined; the second and third columns are composed of the theoretical values or experimental values, respectively. The final column is made up of the errors between the experimental and theoretical values, in percentages.

Table 1: A comparison of the theoretically expected values and the experimentally acquired values for the ratio of the buildup time corresponding to 14.4 M and the buildup times of the other concentrations used in this experiment. The last column represents the error between theory and experiment. In the cases in which multiple trials were performed for a single concentration, the multiple buildup times were averaged.

C	$\left(\frac{C}{14.4 \text{ M}}\right)^{\frac{1}{3}}$	$\frac{\tau_{bu} _{14.4 \text{ M}}}{\tau_{bu} _C}$	$\left \frac{\left(\frac{C}{14.4 \text{ M}}\right)^{\frac{1}{3}} - \frac{\tau_{bu} _{14.4 \text{ M}}}{\tau_{bu} _C}}{\left(\frac{C}{14.4 \text{ M}}\right)^{\frac{1}{3}}} \right \cdot 100\%$
10.84 M	0.909680594	0.920825126	1.225103853
7.28 M	0.796629337	0.930507303	16.80555312
3.72 M	0.636883722	0.652109893	2.390730003
1.94 M	0.512640696	0.482289219	5.920613988
1.05 M	0.417774828	0.365397698	12.53716738
0.605 M	0.347640976	0.264818579	23.82411831
0.3825 M	0.298370798	0.24896198	16.5595353
0.27125 M	0.266073988	0.233909377	12.0885963
0.215625 M	0.246478404	0.241495265	2.021734786
0.16 M	0.223144317	0.249293897	11.71868529

Considering that the average error is roughly 10.51%, one may argue that the theory and experiment are in good agreement. Further, when one considers that the theory used was designed as an order of magnitude theory [16], – i.e., a somewhat phenomenological theory – and was originally intended for crystals (which are more orderly than frozen liquids, even than glasses), it appears that an error of merely ~11% is rather remarkable.

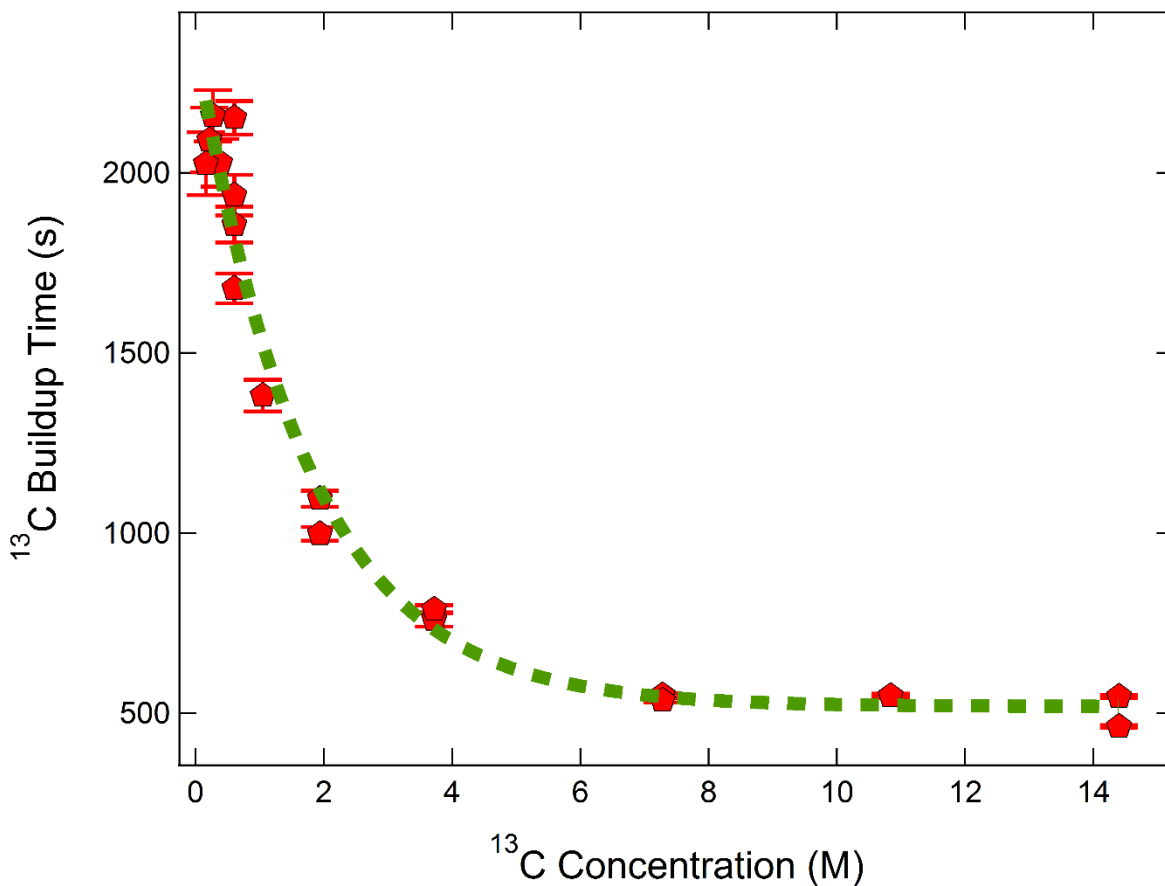


Figure 16: A graph of the ^{13}C hyperpolarization buildup time versus ^{13}C concentration recorded for the DNP of $[1-^{13}\text{C}]$ pyruvic acid. The data was measured under the conditions of 3.35 T and 1.2 K.

Once the buildup curves were recorded, we extrapolated the buildup time of each curve and plotted them as a function of concentration. The result was found to be qualitatively consistent

with the results of Hovav, Feintuch and Vega: when the nuclei were more distant from each other, the buildup time was longer, as seen in Figure 16.

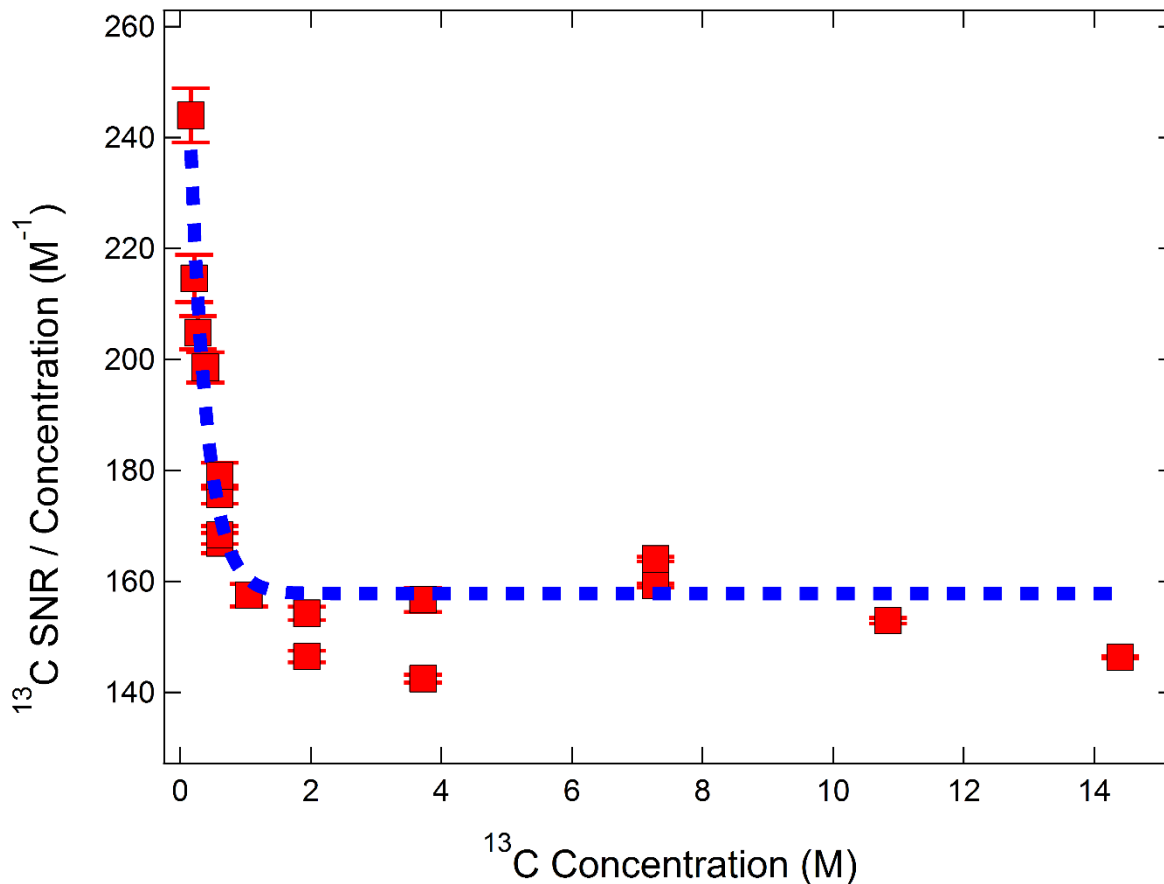


Figure 17: A plot of polarization – as defined in equation (0.2) – as a function of the concentration of $[1-^{13}\text{C}]$ pyruvic acid. This data was extrapolated from buildup curves recorded at 3.35 T and 1.2 K.

This behavior of the buildup times was to be expected: As the interactions which lead to flip-flops and flip-flips are essentially dipolar and as such dipolar interactions are inversely proportional to the distance between the spins, increasing the inter-nuclear distance means that the interaction becomes weaker. If the (electromagnetic) dipolar interaction weakens, then typically there is less energy contained in the field carrying said interaction. If the field overall contains less

energy, then it likely contains less energy per photon. As such, the probability that any one photon carries energy corresponding to the Larmor frequency, or greater, should fall. Hence, the frequency at which flip-flops or flip-flips occur must decrease as well. Thus, it is reasonable to expect that the rate of polarization would fall. This, in turn, means that the buildup time need rise.

Upon measuring the buildup of the ^{13}C hyperpolarization, we also extrapolated their equilibrium polarizations. Figure 17 displays the ^{13}C NMR signal strength divided by the concentration (that is, the polarization per $[1-^{13}\text{C}]$ pyruvic acid molecule) versus the concentration. Intriguingly, the fit departs from a flat line and becomes exponential near 1 M. This suggests that either equation (0.2) fails at sufficiently low concentrations (if the polarization is independent of concentration), or that the polarization becomes highly dependent upon the concentration at this juncture.

The behavior of the polarization for concentrations lower than about 1 M, shown in Figure 17, may be qualitatively explained as follows: The spin-down ^{13}C nuclei in the sample, occupying the higher Zeeman energy level, cannot transition to a higher Zeeman level. Now, according to equation (0.18), the probability that a flip-flop transition occurs is inversely dependent upon r^6 . This means that, as the average inter-nuclear distance increases, the likelihood of a transition decreases and, so, the likelihood that a ^{13}C nucleus which has transitioned to the upper Zeeman level relaxes shrinks. Hence, such far out nuclei should end up staying in the spin-down state longer. This should lead to more nuclei becoming simultaneously spin-down. Thus, a falling ^{13}C concentration should result in a rising polarization [since we are using the definition of polarization in equation (0.2)].

However, in order for this to happen, any contrary forces (like the magnitude of magnetic field fluctuations originating from the radicals and the other nuclei) must be less influential than the impact of the slowing spin diffusion. This may explain the plateau: Suppose, for the moment that we may ignore all influences other than that of the magnetic field fluctuations from the radicals and nuclei and the impact of spin diffusion. Then, since the magnetic field fluctuations emanating from the radicals and nuclei are heavily inversely distance dependent, we would expect that the average magnitude of magnetic field fluctuations from the radicals and the nuclei would decrease with increasing inter-nuclear distance. As such, the frequency of ^{13}C spin-lattice relaxation would

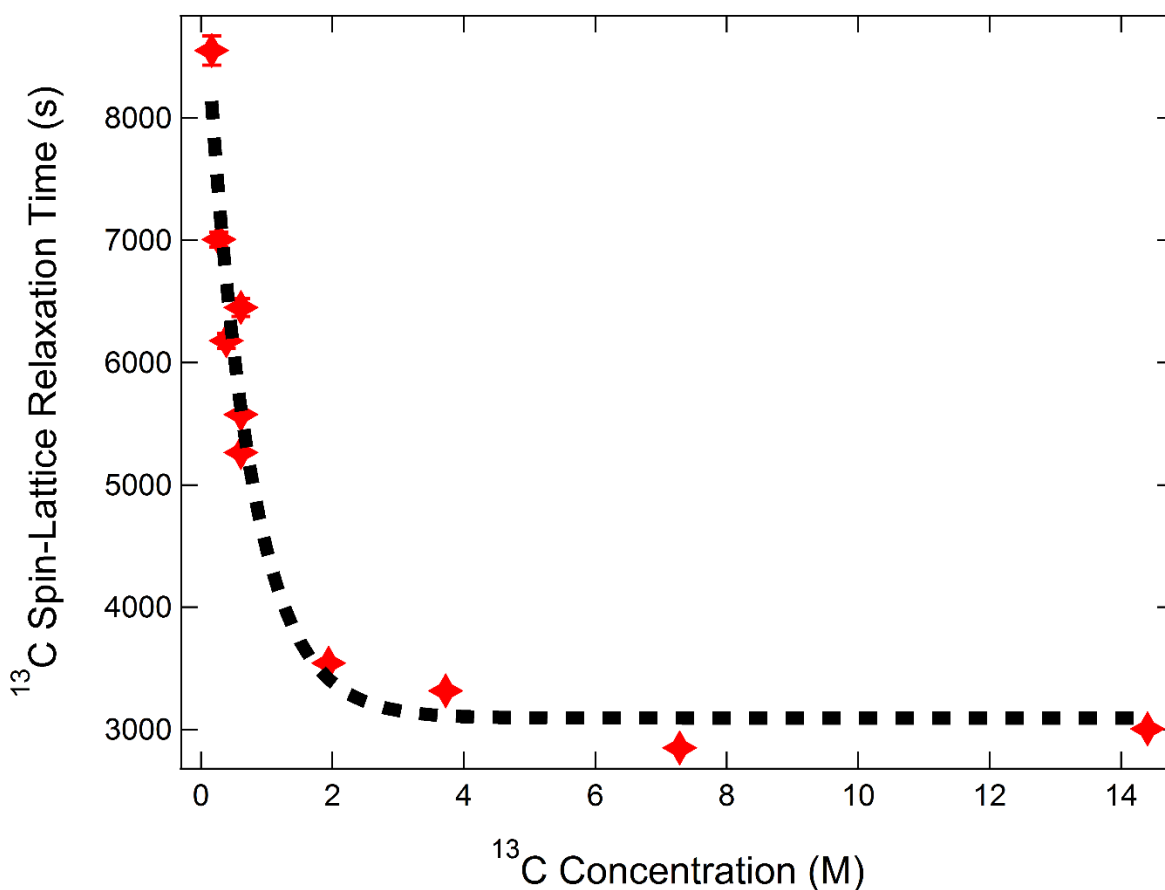


Figure 18: A graph of the behavior of the ^{13}C longitudinal relaxation times as the concentration of $[1-^{13}\text{C}]$ pyruvic acid was varied. This data was acquired under conditions conducive to DNP (at 3.35 T and 1.2 K).

be expected to fall. Now, the [1- ^{13}C] pyruvic acid molecules are more closely spaced than that between the radicals and the ^{13}C nuclei. Hence, while we expect that fewer flip-flop transitions occur per second due to spin diffusion, such transitions would be expected to continue occurring. Thus, under these assumptions, there should (theoretically) be a critical average inter-nuclear distance at which the average magnetic field fluctuations emanating from either the nuclei or the radicals typically have insufficient magnitude to cause the receiving nucleus to relax. This is confirmed in Figure 18 where the concentration dependence of the ^{13}C spin-lattice relaxation times stays at a plateau until roughly 2 M when it starts to asymptote.

CHAPTER 6

AMINO ACID CHARACTERIZATION

Throughout the past four chapters, we have focused upon attempts to optimize DNP and dissolution DNP. In the following two chapters we finally approach an application of DNP: investigating possible biomarkers of cancer. In particular, in this chapter, we intend to characterize the ten amino acids mentioned in Chapter 1. Our characterizations herein are intended to determine which of these ten amino acids are optimal for dissolution DNP.

Table 2: The solubilities of ten amino acids in water and in 1:1 v/v water:glycerol. These solubilities were determined by attempting to mix 5 M aliquots of the amino acids in each solvent; if the sample dissolved, then “Y” was entered into the column representing a solubility of 5 M. If, however, the sample did not dissolve, then an “N” was entered in said column and the sample was diluted until it would represent the concentration in the next column. Then this process would repeat.

	Maximum Concentrations in a Solution of 1:0 DI Water:Glycerol - Y if soluble and N if not soluble																											
Amino Acid	5 M	4.5 M	4 M	3.5 M	3 M	2.5 M	2 M	1.5 M	1 M	0.95 M	0.9 M	0.85 M	0.8 M	0.75 M	0.7 M	0.65 M	0.6 M	0.55 M	0.5 M	0.45 M	0.4 M	0.35 M	0.3 M	0.25 M	0.2 M	0.15 M	0.1 M	0.05 M
Glycine	N			Y																								
Proline	Y														N													
Alanine	N					Y																						
Serine	N			Y																	N							
Arginine	N				Y																N							
Glutamine	N											Y																
Leucine	N													Y														
Isoleucine	N													Y														
Valine	N										Y																	
Methionine	N											Y																
	Maximum Concentrations in a Solution of 1:1 DI Water:Glycerol - Y if soluble and N if not soluble																											
Glycine	N			Y																								
Proline	N	Y														N												
Alanine	N					Y																						
Serine	N			Y																	N							
Arginine	N				Y																N							
Glutamine	N											Y																
Leucine	N													Y														
Isoleucine	N													Y														
Valine	N										Y																	
Methionine	N											Y																

First we examined the solubility of the different amino acids in: water, 1:1 v/v water : glycerol, 1:1 v/v 12 M NaOH : glycerol, 12 M NaOH, 12 M hydrochloric acid and 1:1 v/v 12 M HCl acid : glycerol. The solubilities of those amino acids which dissolved readily in water and 1:1 v/v water:glycerol were not examined in any of the other solutions. Similarly, the solubilities of

Table 3: The solubilities of a) five or b) two amino acids in a) 12 M HCl and 1:1 v/v 12 M HCl : glycerol and b) 12 M NaOH and 1:1 v/v 12 M NaOH : glycerol. These solubilities were determined in the same manner as described in the caption to Table 2, but with different solvents.

a)

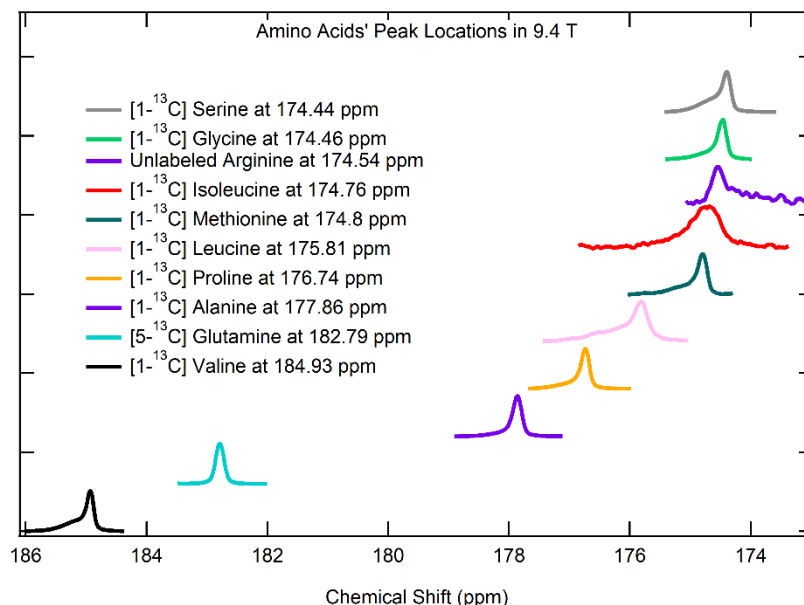
	Maximum Concentrations in a 12 M HCl Solution - Y if Soluble and N if not Soluble																									
Amino Acid	5M	4.5M	4M	3.5M	3M	2.5M	2M	1.5M	1M	0.95M	0.90M	0.85M	0.80M	0.75M	0.70M	0.65M	0.60M	0.55M	0.50M	0.45M	0.40M	0.35M	0.30M	0.25M		
Leucine	N				Y																					
Isoleucine	N								Y																	
Methionine	N			Y																						
Valine	N				Y																					
Arginine	Y												Y													
Glutamine	N									Y																
	Maximum Concentrations in a 1:1 Glycerol:12 M HCl Solution - Y if Soluble and N if not Soluble																									
Leucine	N								Y																	
Isoleucine	N								Y																	
Methionine	N								Y																	
Valine	N					Y																				
Arginine	N		Y																							
Glutamine	N												Y													

b)

	Maximum Concentrations in a 12 M NaOH Solution - Y if Soluble and N if not Soluble									
Amino Acid	5 M	4.5 M	4 M	3.5 M	3 M	2.5 M	2 M	1.5 M	1 M	0.5 M
Glutamine	Y									
Valine	N	Y								
	Maximum Concentrations in a 1:1 Glycerol:12 M NaOH Solution - Y if Soluble and N if not Soluble									
Glutamine	N				Y					
Valine	N				Y					

those amino acids which readily dispersed in 1:1 v/v 12 M hydrochloric acid:glycerol and 12 M HCl acid were not considered in either 12 M NaOH or 1:1 v/v 12 M NaOH:glycerol. The results of this characterization of solubilities are shown in Tables 2 and 3 below.

Table 4: Top: Graphical display of the peak locations of ten amino acids. Bottom: The ^{13}C NMR chemical shift locations of the various amino acids. All of the amino acids were labeled at the C1 position except for glutamine which was labeled at the C5 position. Additionally, the values in yellow rectangles were acquired from hyperpolarized natural abundance samples (which contain but 1.109% labeled carbons), meaning that such values are less reliable than peak locations of labeled samples. The glutamine peak locations marked by a “*” were acquired from a mixture of 50% alanine and 50% glutamine. All values measured were in units of parts per million (ppm). Red entries signify the absence of data.



Amino Acids	Peak Locations (in ppm)						
	9.4T				1T		
	Without Solvent Deuteration				With Solvent Deuteration		With Solvent Deuteration
	Without Gd ³⁺ or Ho ³⁺	With Gd ³⁺	With Ho ³⁺	Without Gd ³⁺ or Ho ³⁺	Without Gd ³⁺ or Ho ³⁺		
Using TEMPO	Using trityl	Using trityl	Using trityl	Using TEMPO	Using TEMPO	Using trityl	
Proline	175.7	176.18	175.7	175.56		176.02	
Alanine	176.83	177.31	176.79	176.96		177.1	
Glycine	172.08	173.895	173.5	173.32		173.78	173.82
Serine		173.84		173.28		173.75	
Leucine	175.14	175.325		174.42		175.79	
Isoleucine		174.13		173.18	174.96	174.32	
Methionine	157.92	174.25		173.4		174.4	
Valine		184.385	184.11		175.055	174.46	
Glutamine	180.26*	183.3*	182.94				
	182.79*	184.10*	183.89				
	183.73*	185.155*					
Arginine	174.54						

The results shown in Table 2 indicate that the amino acids glutamine, leucine, methionine, valine and isoleucine can achieve a concentration of at most 0.15 M. As discussed in the introduction, the signal-to-noise ratio is at least linearly dependent upon the concentration. Hence, such low concentrations are less conducive to DNP than desirable. Seeking better solubility, we tried to dissolve these five amino acids in, first, an acid (12 M HCl). When that did not lead to sufficiently high concentrations for two of the amino acids (valine and glutamine), we tried to dissolve them in a base (12 M NaOH) as shown in Table 3.

After identifying these solubilities, we learned that, on rare occasions, 12 M HCl could damage the NMR magnet. As such, we tried to minimize use of acid in the solvent. Within a year of developing these tables, we determined that leucine, methionine and isoleucine were soluble in 12 M NaOH such that a solution containing a concentration of around 1 M could be prepared. However, for the most part, Table 3 a) continues to represent roughly optimal solubilities.

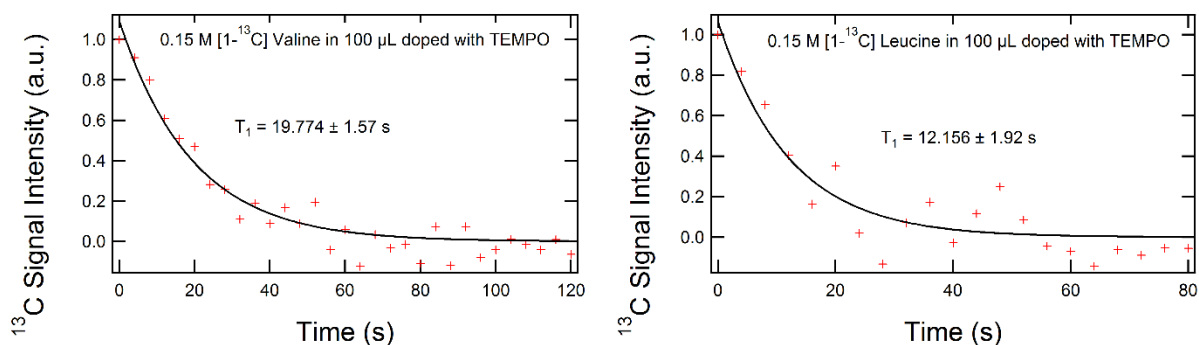
The next step was to identify roughly where the spectral peaks of each amino acid were located. This step involved both hyperpolarization of various amino acid samples and use of thermal equilibrium spectra acquired with a large number of scans (so that the SNR would rise). These results are shown in Table 4.

Notice that the $^{13}\text{C}_1$ peak locations of glycine and serine were incredibly close to each other. This is a sign of a possible issue: According to [123], glycine tends to be metabolized into serine by serine hydroxymethyl transferase (SHMT); as such, if the carbon-13 stays in the C1 position during the reaction, then it may be nigh impossible to distinguish between reactant and product – even if hyperpolarization is used! Unfortunately, the ^{13}C nucleus does stay in the C1 position

throughout said reaction. This suggested that we table examining the serine and glycine metabolism in cancer cells.

After determining the ^{13}C spectral peak locations, we examined the T_1 s of these ten amino acids under a small set of differing conditions. Table 5 lists the T_1 s of the various amino acids we

Table 5: Top: Two examples of the decay of the polarization seen during spin-lattice relaxation. Bottom: The different T_1 values measured for each of the ten amino acids investigated. As with Table 4, the yellow boxes contain values acquired from samples in which only about 1.109% of the carbons were labeled. (The green boxes contain T_1 s recorded from samples in which over 99% of the carbons were enriched.) This means that one should consider the data in yellow to be less reliable than that in green. The red rectangles represent an absence of data.



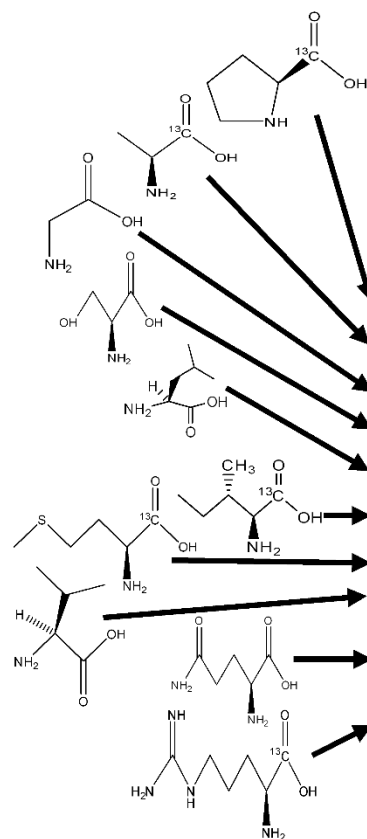
	Spin-Lattice Relaxation Time (T_1 in seconds)					
	9.4 T				1 T	
	Without Solvent Deuteration				With Solvent Deuteration	
	Without Gd^{3+} or Ho^{3+}		With Gd^{3+}		Without Gd^{3+} or Ho^{3+}	
Amino Acids	Using TEMPO	Using trityl	Using trityl	Using trityl	Using TEMPO	Using trityl
Proline	27.04 \pm 0.17	35.49 \pm 0.04	16.82 \pm 0.05	43.08 \pm 0.20	43.86 \pm 0.18	
Alanine	18.18 \pm 0.69	32.49 \pm 0.31	8.59 \pm 0.07	32.08 \pm 0.08	32.69 \pm 0.79	
Glycine	26.42 \pm 0.04	37.39 \pm 0.19	9.35 \pm 0.05	45.98 \pm 0.09	28.63 \pm 0.29	39.82 \pm 0.39
Serine		29.31 \pm 0.27		31.22 \pm 0.02	27.95 \pm 0.14	
Leucine	14.85 \pm 0.05	14.46 \pm 0.22		10.76 \pm 0.01	12.16 \pm 1.92	
Isoleucine		12.64 \pm 0.31		10.76 \pm 0.01	22.99 \pm 2.01	
Methionine	9.20 \pm 2.01	13.79 \pm 0.19		10.44 \pm 0.02	11.67 \pm 2.75	
Valine		18.14 \pm 0.09	27.59 \pm 0.23		19.77 \pm 1.57	
Glutamine	28.17 \pm 0.07	27.07 \pm 0.04	26.75 \pm 0.09			
Arginine	14.49 \pm 1.69					

investigated. Such allowed us to determine which amino acids would work better under the conditions of dissolution DNP. This is because, under dissolution DNP, the magnetic-

environment-dependent T_1 of the ^{13}C nuclei plays a large role in the decay of the ^{13}C NMR signal, as seen in equation (0.15).

These results suggest that it may be advisable to avoid using methionine or isoleucine in dissolution DNP: their T_1 s are all dreadfully small which would limit the extent of the reaction that could be observed. While leucine and valine were also on the border between being lousy choices and being useful, we shall find out in Chapter 7 that glioblastoma and *PC-3* have a strong affinity for these two compounds.

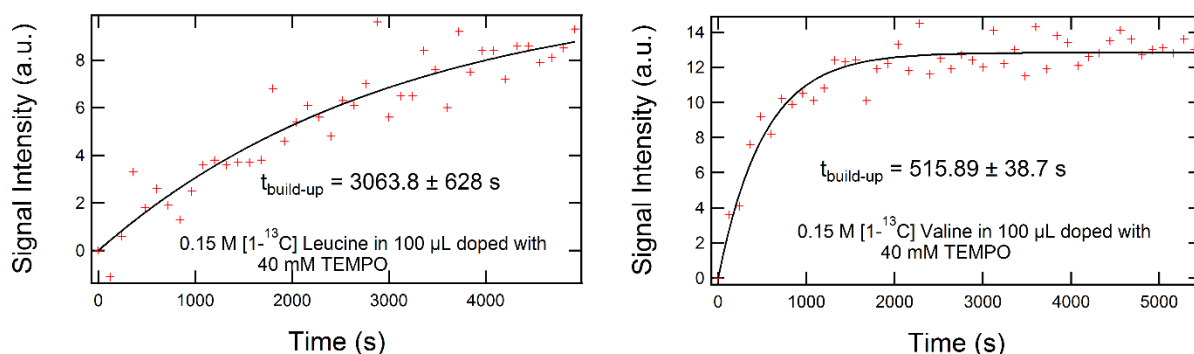
Table 6: Left: Chemical structures of the amino acids discussed in this dissertation. Right: Liquid-state enhancements for the ten amino acids chosen for this dissertation measured under varying conditions. Again, the yellow entries, having been acquired from hyperpolarizing non-enriched compounds, are less reliable. The “*” mark indicates that the compound was labeled in the C5 position as opposed to the C1 position. All red rectangles represent the absence of data.



Amino Acids	Enhancements						
	9.4T				1T		
	Without Solvent Deuteration			With Solvent Deuteration		With Solvent Deuteration	
	Without Gd ³⁺ or Ho ³⁺	With Gd ³⁺	With Ho ³⁺	Without Gd ³⁺ or Ho ³⁺	Without Gd ³⁺ or Ho ³⁺		
	Using TEMPO	Using trityl	Using trityl	Using trityl	Using TEMPO	Using TEMPO	Using trityl
Proline	24,262.79	8,624.26	9,268.10	42,223.95		211,067.60	
Alanine	6,970.72	9,360.54	13,039.45	23,371.73		137,602.50	
Glycine	9,560.44	7,289.65	3,072.45	58,951.38		253,273.80	336,650.10
Serine		3,950.69		35,952.75		274,896.50	
Leucine	1,836.14	1,055.51		6,755.93		47,595.88	
Isoleucine		433.46		5,406.91	706.51	132,850.09	
Methionine	86.86	357.15		4,873.24		48,926.89	
Valine		2,776.12	8,959.66		959.93	63,865.86	
Glutamine	3654.81*		12,661.94				
Arginine	715.70						

Upon acquisition of the dissolution DNP decay data (which allowed identification of the T_{1s}), we calculated the enhancements via equation (0.16). Such enhancements will tell us how much signal improvement to expect; if the signal improvement is too low, the chances of being able to detect either all reactants or all of the reactions which occur decreases. The resulting enhancements for our ten amino acids are listed in Table 6 above.

Table 7: Top: Two examples of the buildup of polarization which occurs during DNP. Bottom: ^{13}C NMR intensity buildup times for the ten amino acids considered in this work acquired under various conditions. The units of each entry are seconds. This data was all recorded via the 3.35 T HyperSense at UTSW. All red rectangles represent a lack of data.



	DNP Build-Up Times (in seconds)			
	Without Solvent Deuteration		With Solvent Deuteration	
	With Gd^{3+}	With Ho^{3+}	Without Gd^{3+} or Ho^{3+}	
Amino Acids	Using trityl	Using trityl	Using TEMPO	Using trityl
Proline		3,097.9 ± 64.8	2,587.8 ± 240.0	
Alanine		2,300.5 ± 322.0	837.9 ± 111.0	
Glycine		2,269.6 ± 61.5	1,040.2 ± 144.0	2,154.2 ± 493.0
Serine		3,503.9 ± 299.0	1,304.3 ± 71.9	
Leucine		1,916.5 ± 174.0	3,063.8 ± 628.0	
Isoleucine		2,046.1 ± 178.0	735.9 ± 44.5	
Methionine		1,617.8 ± 174.0	627.5 ± 44.5	
Valine	5,000.6 ± 745.0		515.9 ± 38.7	
Glutamine	4,714.9 ± 329.0		1,734.1 ± 183.0	
Arginine				

It should be briefly noted that enhancements acquired within our lower field (1 T) NMR system tended to be much higher, as seen on the right hand side of Table 6 above; however, our 1 T NMR system had severe limitations when detecting ^{13}C NMR signals which were not present in

the 9.4 T NMR magnet. As such, we shall limit our discussion to results recorded using the 9.4 T NMR system.

Still, the liquid-state enhancements acquired at 1 T, shown in Table 6, are contrary to expectations, and so must be explained since the polarization at low temperatures is proportional to the magnetic field. As such, these rather large liquid-state enhancements seen in Table 6 might be understood by remembering that 1), when recording ^{13}C NMR signals at 1 T, the thermal polarization is typically quite low, 2) deuteration of the solvent can be expected to have improved the hyperpolarization to some extent and 3), that much of the signal enhancement occurred under a higher magnetic field. It could be interesting to test if these enhancements were to hold up under further trials.

As with the T_{1S} , isoleucine and methionine displayed poorer enhancements than the other amino acids. Although the enhancements of valine and leucine were higher than those of methionine and isoleucine, they were still relatively low. Yet, as emphasized above, we shall find in Chapter 7 that the reaction taking leucine into and from alpha-ketoisocaproate and that taking valine into and from alpha-ketoisovaleric acid are prominent in certain cancer cell lines.

The last items we investigated at length were the buildup times of each labeled amino acid under various conditions (see Table 7). These values are significant in that they may be used to predict a minimum amount of time required for a dissolution DNP experiment. That is, an average time of at least twice the buildup time will be required for the polarization to almost reach the equilibrium polarization (specifically, it will reach about $\frac{e^2-1}{e^2} \cdot 100\%$ of the maximum magnetization).

Notice that, when doped with trityl and mixed in a non-deuterated, Holmium-doped solvent, the buildup time of leucine is shorter than any of the other amino acids tested under these conditions. Additionally, observe that when doped with TEMPO and mixed in a deuterated glassing matrix, valine had the shortest buildup time of all the samples examined. Ideally these two notes would not be significant factors because, ideally, we would have an indefinite amount of time to perform each dissolution. However, in reality, our group was renting the HyperSense system from UT Southwestern. As such, constraints on the amount of time with the HyperSense meant that compounds which could be quickly polarized were preferable so long as a reasonable equilibrium polarization could be reached.

This data suggests that proline and alanine are perhaps the best amino acids to hyperpolarize: both had higher solubilities, $T_{1\rho}$ s and enhancements. Glutamine would be a nice third candidate if not for the fact that it tends to spontaneously form glutamate in solution. This would make the task of understanding the reaction more difficult. This means that, when these results are combined with the information laid out in the next chapter, valine and leucine appear to be the second best amino acids (out of this group of ten) to hyperpolarize.

However, alanine tends to be converted into pyruvate and then lactate in cancers; that is, as hyperpolarization of pyruvate is well studied in various cancers [124], [125], the motivation to hyperpolarize alanine (which would most likely just convert into pyruvate and so on) is lessened. Additionally, valine and leucine are both branched chain amino acids, suggesting that they may display some pattern. Thus, we decided to prioritize investigating leucine and valine in glioblastoma and prostate cancer.

CHAPTER 7

CANCER METABOLISM OF ALPHA-KETOISOCAPROATE (ALPHA-KETOISOVALERIC ACID) AND LEUCINE (VALINE)

In the last chapter, we determined that, when the data collected therein is combined with information from this chapter, leucine and valine should be prioritized in this dissertation. We begin this chapter with background information on the relationship between leucine, valine and their products and cancer cells. In the first section, we shall detail some of the prior studies investigating said relationship. In the second section, we shall summarize what we actually did in the experiment so far. Finally, we shall discuss our current results and, by combining them with the information gathered in the first section of this chapter, we shall advance a hypothesis as to part of the reason that prostate cancer cells (specifically, *PC-3*) and glioblastoma (*SfXL* in particular) seem to like leucine and valine.

7.1 Leucine Metabolism in Cancer

Sifting through the literature reveals that, in some cases, such as with pancreatic cancer, high leucine concentrations in the blood were indicative of malignancy [86]. However, in others, like lung [126], gastric [85] and bladder [88] cancers or leukemia [127], glioblastoma [128, p. 1] and lymphoma [129], cells are heavily dependent upon the expression of an enzyme called branched-chain amino acid aminotransferase, or BCAT, for the intracellular production of certain amino acids such as leucine. Significantly, one also learned that, according to Tee and Wang et al., some cancers, such as those in the prostate, import large concentrations of leucine in exchange for lots of nutritious amino acids such as glutamine – an alternative energy source for cancerous cells [87], [130]. According to Eden and Benvenisty, mammalian cell lines experience inhibited

growth and apoptotic effects at sufficiently high concentrations of alpha-ketoisocaproate (KIC) [131]. Furthermore, Hattori et al., showed that inhibition of BCAT in leukemia led to intracellular levels of KIC and leucine rising and falling, respectively [132].

7.2 The Experiment

In this experiment, we tracked the metabolism of [$1\text{-}^{13}\text{C}$] KIC (Cambridge Isotope Laboratories, MA) and [$1\text{-}^{13}\text{C}$] leucine (Cambridge Isotope Laboratories, MA) in prostate cancer cells [using the *PC-3* (American Type Culture Collection, VA) cell line] as well as [$1\text{-}^{13}\text{C}$] KIC, [$1\text{-}^{13}\text{C}$] alpha-ketoisovaleric acid (KIV) (Cambridge Isotope Laboratories, MA) and [$1\text{-}^{13}\text{C}$] leucine in glioblastoma [via the *SfXL* (American Type Culture Collection, VA) cell line] primarily by way of cell extracts. The protocol for performing cell extracts is listed in appendix B. In order to perform the cell extracts we had to prepare ten micro-centrifuge tubes (there were two plates per time point) per direction of the reaction being investigated, each containing enough [$1\text{-}^{13}\text{C}$] compound that, once mixed in 15 mL, would result in a concentration of 10 mM. When extracts were performed using *SfXL* glioblastoma cells, this protocol was changed in the following two ways: i) the plates were doped with 5 mM, as opposed to 10 mM, ^{13}C -labeled compounds so as to save resources; and ii) each point of time was represented with one plate instead of two. Other than the change in concentrations, these two modifications should not have made a significant difference to the results (so long as the resulting NMR samples were still doped with 10 mM ^{13}C urea (Cambridge Isotope Laboratories, MA)).

Following lyophilization of the samples, each sample was mixed with 800 μL of D_2O doped with 10 mM ^{13}C urea. The ^{13}C urea was added to provide a reference in regard to both chemical shift and to determine relative concentrations. Additionally, all cell extracts done in this

dissertation spanned a time of 48 hours; this means that by the end of the extracts discussed herein, the cell lines were often over-confluent, having been growing on the same plate for roughly 72 hours.

We also performed “media extracts” when working with the *PC-3* cell line in this experiment – that is, instead of discarding the media before killing the *PC-3* cells with 12% perchloric acid, we keep it, kill the few cells alive in the media with about 10 mL of 12% perchloric acid and subject the media to the same steps that normal cell extracts are put through after the cells are killed. This was done in order to monitor the extra-cellular environs. When performing the extracts using *SfXL*, on the other hand, no media extracts were performed due to two considerations: first, when neutralizing and lyophilizing media extracts, the time required to completely prepare the media extracts is, in our experience, around double the time required to prepare cell extracts; and second, the media extracts, although somewhat useful, typically provide far less information than the cell extracts. As such, while the media for each extract was generally kept, most of such media samples were never prepared for NMR.

After the extracts were doped with ^{13}C urea, 400 μL to 500 μL of the resulting solutions were transferred into 5 mm NMR tubes (Wilmad-LabGlass, NJ). These tubes were then inserted in a 600 MHz NMR magnet (Bruker Biospin, Billerica, Massachusetts) and run, overnight for a minimum of 2048 scans (this meant about two hours per sample). The software directing the magnet then emailed the results (one PDF and one file containing the data) to whoever had loaded the samples into the magnet. The data files were then opened and analyzed using the software MestReNova (Mestrelab Research, S.L., A Coruña, Spain).

After tracking said metabolism via extracts, we performed a western blot procedure upon a confluent plate of *SfXL* and a confluent plate of normal human astrocytes (NHA) (American Type Culture Collection, VA). Said procedure is listed in Appendix A. The western blot procedure results in a stain, of sorts, whose area and location correlates to the concentration and identity of enzymes (such as BCAT). The area of the stain must be compared to that of a reference protein, such as beta-actin, in order that the amount of BCAT can be quantified.

Due to time constraints, we were unable to perform dDNP such that ^{13}C KIC, leucine, valine or KIV became hyperpolarized and were mixed with *SfXL* cells in order to monitor the resulting reactions.

7.3 Results and Discussion

First, we monitored the two reaction directions (KIC to leucine and leucine to KIC) via carbon-13 NMR of *PC-3* cell and media extracts using 10 mM urea as a reference in regards to both its chemical shift and its concentration. The first thing we noticed was that, in the media, the spectra of which are shown in Figure 19 parts a) and c), the concentrations of KIC and leucine frequently dwarfed that of urea whereas, in the cells, the spectra of which are shown in Figure 19 parts b) and d), these concentrations were often lower than that of urea. Second, we observed that, in the leucine to KIC direction, the leucine concentration stayed fairly constant, whereas, in the other direction, we saw KIC convert to leucine. This suggested that perhaps the BCAT in *PC-3* has a preferred direction in the two reaction directions between KIC and leucine. This is important because it would imply that, if BCAT were overexpressed in *PC-3*, then injecting a high concentration of the main reactant (which appears to be KIC) would produce a large concentration

of (in this case) leucine in and about the malignant tumor, allowing chemical shift imaging to non-invasively determine the presence of said tumor.

Plotting the normalized concentrations versus time confirmed that the concentrations of both reactant and product were generally higher in the media than within the cells, as seen through comparison of the different parts of Figure 20. This is realized in the case of the dopant because the extract process involves doping the media. While the reason that the media contains more leucine [see Figure 20, parts b) and d)] is clearly that the cells are exporting it in great amounts,

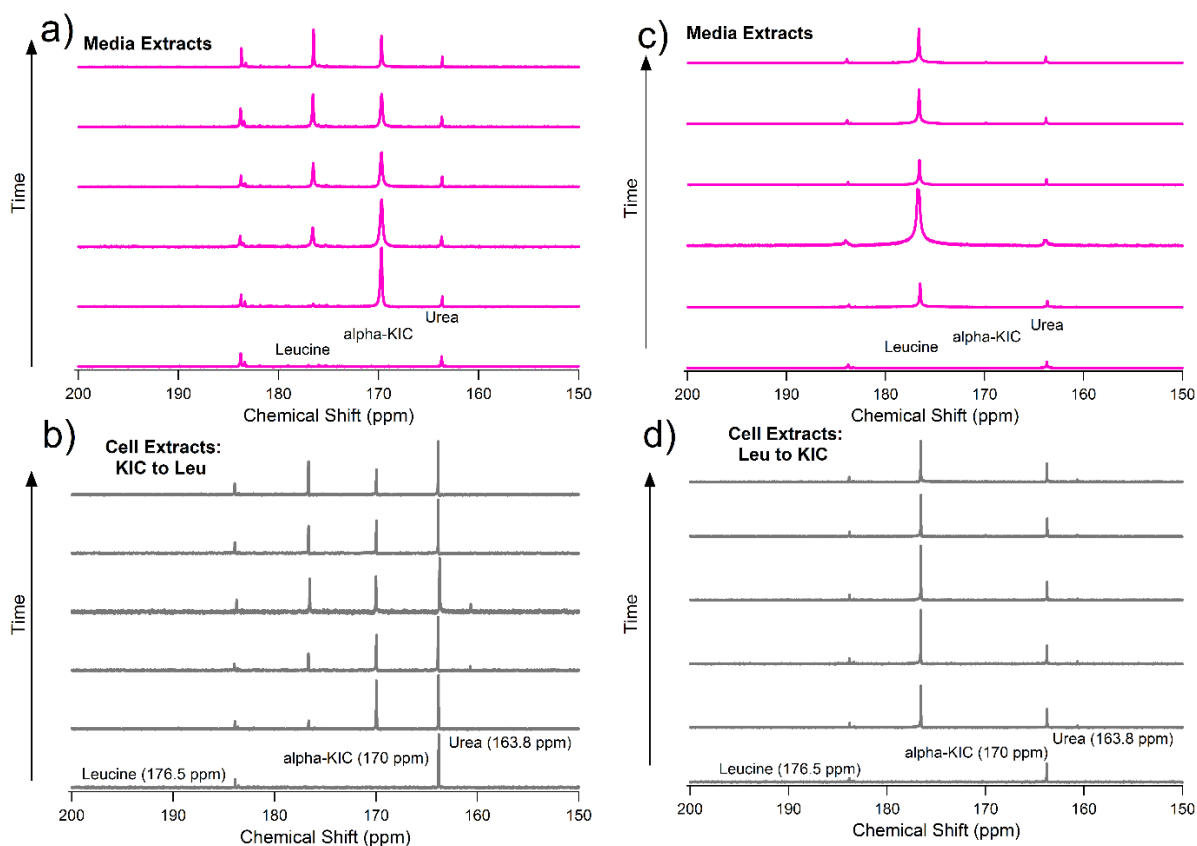


Figure 19: The spectra acquired from ^{13}C NMR of cell and media extracts arranged such that time is increasing from the second spectrum to the top spectrum. The bottom spectrum of each graph is that of the control. (This arrangement shall be referred to as a waterfall plot.) Waterfall plots of PC-3 cell and media extracts corresponding to a) and b) the KIC to leucine (Leu) direction and to c) and d) the leucine to KIC direction. The media extracts are at the top in pink and the cell extracts are at the bottom in grey.

the explanation for why the cells might do this is more complicated and required integrating information from section 7.1 with these results. Before we form our hypothesis, we should also notice that, when the media was doped with $[1-^{13}\text{C}]$ leucine, the cells did not really seem to convert leucine into KIC. This strongly suggests that KIC is a possible biomarker for the presence of *PC-3*.

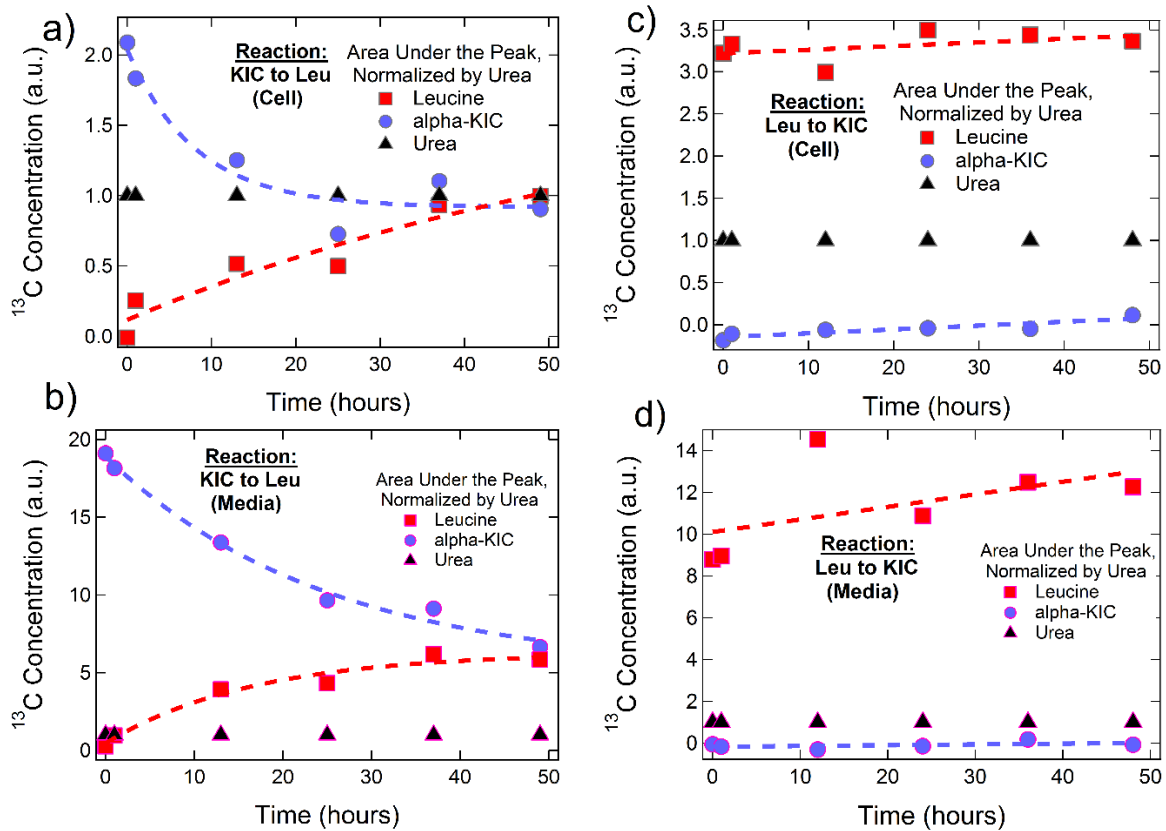


Figure 20: Curves which describe the time dependence of two directions of the reaction between leucine (Leu) and KIC. The top plots [parts a) and c)] show this reaction taking place in the cells, whereas the bottom graphs [parts b) and d)] show the presence of leucine or KIC in the media which surrounded the cells.

Suppose that the results of Hattori et al. may be reliably extended from applying to leukemia to applying to *PC-3* (and, perhaps, to *SfXL*). Further, we assume that the conclusion of Wang et al, in which *PC-3* imports a large amount of leucine in exchange for amino acids in order

to stimulate cell growth [130], may be applied to *SfXL* as well. (If this is not so, then we restrict attention of our hypothesis solely to *PC-3*.) Consideration of the data acquired and the conclusion arrived at by Eden and Benvenisty as well leads one to suggest the following (complex) hypothesis

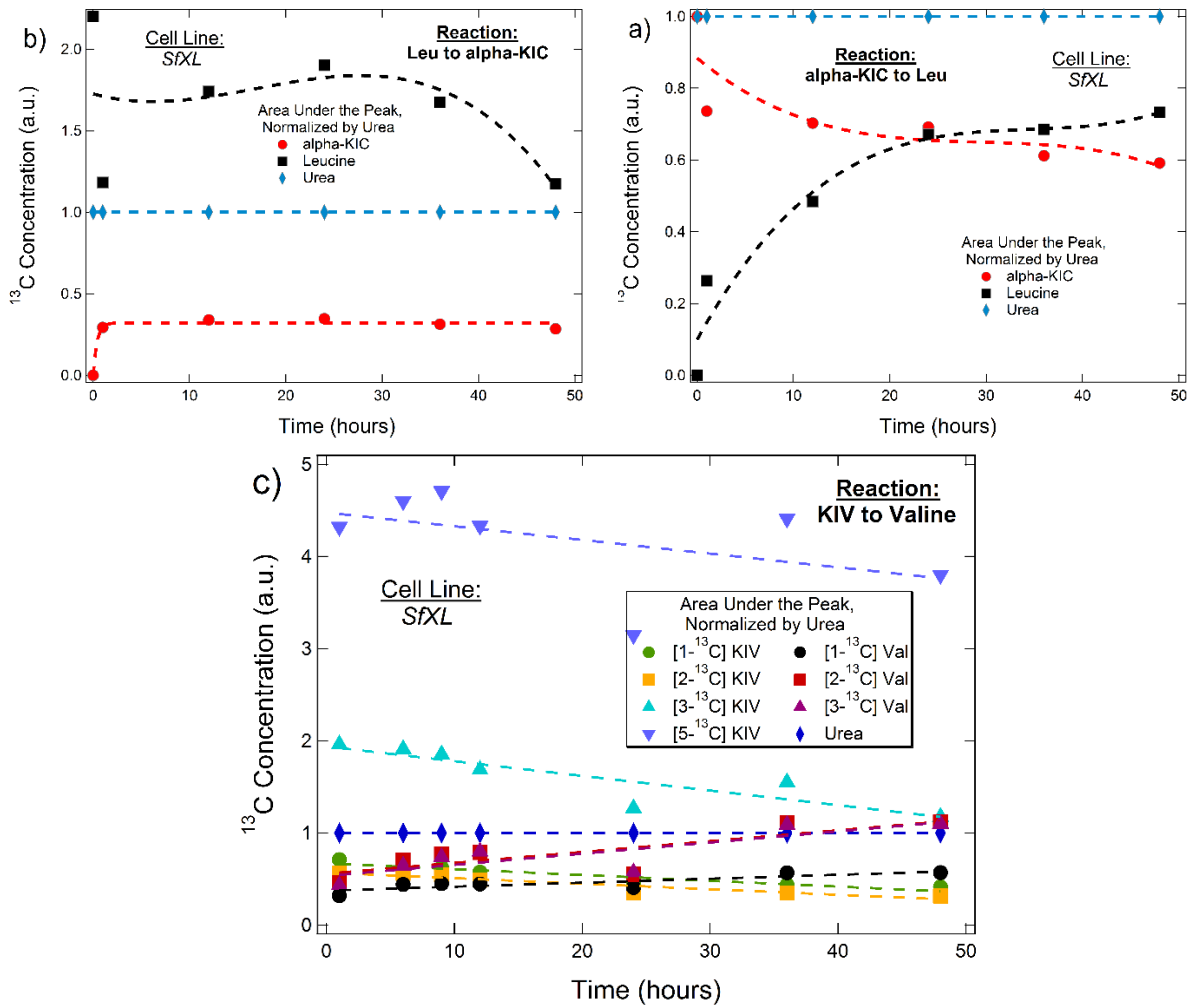


Figure 21: Parts a) and b) represent the KIC to leucine and leucine to KIC reaction directions, respectively, such that the ^{13}C -doped compounds were introduced into the environs of *SfXL* glioblastoma cells. Part c) represents the data acquired so far for the KIV to valine (which is denoted as “Val” in the legend) direction.

concerning the behavior of these cells with respect to leucine and KIC: To decrease the chances of an environment containing high concentrations of KIC, the *PC-3* or *SfXL* cells import KIC (as well

as leucine) and convert it to leucine via BCAT. This comes with the benefit that intracellular leucine seems to promote cell growth by way of its activation of mTOR kinase. However, this also comes with a loss of amino acids which were exchanged for said KIC. As such, the malignant cells export a portion of their now abundant supplies of leucine so as to regain nutrients such as glutamine.

Next, we monitored the two reaction directions between KIC and leucine and between KIV and valine in the *SfXL* cell line through ^{13}C NMR cell extracts. As can be seen in Figure 21 parts

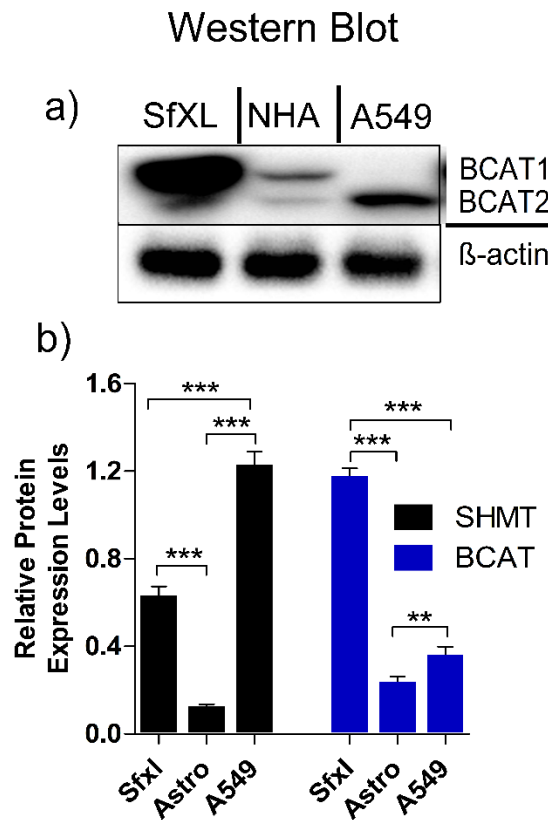


Figure 22: The results of a western blot performed upon SfXL, NHA (labeled “Astro” in the figure) and A549 (a lung cancer cell line). The results for A549 are not relevant to this dissertation. Part a) displays the stains which show the expression of BCAT 1 and 2 in SfXL and in NHA as well as the stain representing beta-actin. Part b) shows the area of the stains for the enzymes being investigated relative to that of the beta-actin in a bar plot. The data on the right side of this histogram represents the results for BCAT.

a) and b), *SfXL* seems to successfully convert KIC into leucine. Yet, when the glioblastoma cells were exposed to [1-¹³C] leucine to test the opposite direction, the leucine concentration fell. This suggests that leucine may be getting exported out of the cell; while this would be consistent with our hypothesis, this interpretation is put in doubt by the large uncertainty between the initial concentration of leucine and the leucine concentration at one hour as well as by the plateau in the KIC concentration.

Part c) of Figure 21, indicates that, in *SfXL*, the metabolism of KIV into valine is dramatically different than the metabolism of KIC into leucine: The KIV generally did not convert into valine, whereas the KIC clearly transformed into leucine. While we have collected data for the valine to KIV reaction direction, it would i) only represent 2-3 points and, so, would not reflect the reaction accurately and ii) said 2-3 points were acquired for an extract that spanned a total of 48 hours, whereas all the curves in Figure 21 were acquired in extracts that spanned a total of 72 hours. As such, interpretation of this information concerning KIV must await collection of more data on the valine to KIV direction.

After examining the reactions between leucine and KIC and (to some extent) between valine and KIV, we, with the help of a collaborator, performed a western blot upon one plate of confluent *SfXL* and one plate of 60% - 80% confluent NHA. The results, both quantitative and qualitative, are shown in Figure 22.

As shown in Figure 22 a), the expression of BCAT1 in *SfXL* was much greater than in NHA. This is demonstrated in that the stain corresponding to *SfXL* and occurring at roughly 43 kiloDaltons (which is what the BCAT1 protein is expected to weigh) is much greater in size than the blot corresponding to NHA at the position corresponding to a similar weight. Now, BCAT1

resides in the cytoplasm of a cell, whereas BCAT2 is located within mitochondria [133]. As such, while BCAT2, at roughly 39 kDa, is also darker and covers more area when considering *SfXL* compared to NHA, BCAT2 must here be considered less of an indication of the presence, and thus expression, of the BCAT enzyme which converts branched-chain alpha-keto acids into branched-chain amino acids. This smaller BCAT2 blot may be affected depending upon the strength of RIPA buffer and, to a much lesser extent, the efficiency of the cell scraper with regard to breaking down mitochondrial membranes. It might be interesting to try using a stronger buffer in order to see if the size of the blot representing BCAT2 changes while that for BCAT1 stays constant.

Furthermore, as can be seen in Figure 22 b), BCAT is expressed nearly six times as much in *SfXL* as in NHA. This suggests that the BCAT enzyme is over-expressed in *SfXL*. In turn, such weakly implies that this overexpression may be tied to the hyperactivity of glioblastoma cells. This conclusion is further buttressed by the fact that human cells seem to be unable to produce branched-chain alpha-keto acids (such as KIC or KIV) from scratch [133]. Regardless of how this overexpression of BCAT figures into the metabolism of glioblastoma, this dramatic increase in expression by a factor of (approximately) six strongly supports the idea that KIC is an excellent possible biomarker for glioblastoma and prostate cancer, particularly for *SfXL* and *PC-3*.

CHAPTER 8

CONCLUSIONS

In conclusion, we have proven that, when using the wide ESR linewidth free radical TEMPO, not every ^{13}C isotopic location in sodium acetate results in equal DNP efficiency. We have also shown that, although mixing TEMPO with an optimal concentration of trityl results in an interesting competition between the radicals, it does not improve the DNP performance. Mixing trityl and BDPA, on the other hand, led to a benefit over using either BDPA or trityl alone, at least when irradiating at the common spin-up peak of BDPA and trityl. Intriguingly, we showed that, as the concentration of ^{13}C in the C1 position of pyruvic acid decreases to that of natural abundance, the net DNP polarization asymptotes, as do the solid-state ^{13}C spin-lattice relaxation and build-up times. This interesting finding would acquire more of a practical hue if the result was found to remain valid in an experiment identical to the one we performed, but with all three carbons in pyruvic acid being enriched as opposed to just the C1 position. Additionally, deuteration of the glassing matrix used was demonstrated to result in a longer T_1 when using the narrow EPR-linewidth radical trityl and to have no measurable effect when using the wide ESR-linewidth radical TEMPO. Lastly, we have measured and stitched together disparate data in order to prove that ^{13}C KIC has excellent potential as a biomarker for detecting glioblastoma in a non-invasive manner.

APPENDIX A
WESTERN BLOT PROCEDURE

- i. Preparing the Lysate
 - 1 Aspirate the media from a 60-80% confluent plate.
 - 2 Wash the plate with ice-cold PBS; aspirate; repeat once.
 - 3 Suspend the cells in the plate by pipetting 1 mL of 4° C RIPA buffer containing recently added protease inhibitors (RIPA+PI). The RIPA+PI stock should be kept in an ice bath when not being used.
 - 4 Tilt the plate to make sure said RIPA+PI covers the whole plate and then use a cold cell scraper to scrape the cells to the bottom of the plate.
 - 5 Pipette the resulting suspension into one cold 1.5 mL microcentrifuge (MC) tube.
 - 6 Place several ice packs upon the rocker (to keep temperature of the centrifuge tube around 4° C) and then rock (i.e., mix) the centrifuge tube for 30 minutes.
 - 7 Centrifuge the MC tube at ~13,000 rpm (about 20,000 g) for 20 minutes. This centrifugation must be done such that the sample stays near 4° C throughout the process.
 - 8 There should now be an amorphous precipitant sitting near the bottom; Pipette the supernatant into a new ice-cold MC tube and keep this MC tube (call it “S”) in an ice bath; Be careful not to pipette the precipitant into S.
 - 9 Repeat for each plate or cell line. Keep everything on ice.

- ii. Conducting the Bradford assay
 - 1 Prepare the standards according to the instructions which come with the kit:
 - a. Label MC tubes “A” through “I”.
 - b. Pipette 300 μ L of the BSA stock into tube A.
 - c. Pipette 375 μ L of the BSA stock into B and mix with 125 μ L of the RIPA+PI stock.
 - d. Pipette 325 μ L of the BSA stock into C and mix with 325 μ L of the lysis buffer (the RIPA+PI stock).
 - e. Transfer 175 μ L of B into D and mix with 175 μ L of the lysis buffer.
 - f. Transfer 325 μ L of C into E and mix with 325 μ L of the lysis buffer.
 - g. Transfer 325 μ L from E into F and mix with 325 μ L of the lysis buffer.
 - h. Transfer 325 μ L from F into G and mix with 325 μ L of the lysis buffer.
 - i. Pipette 100 μ L from G into H and mix with 400 μ L of the RIPA+PI stock.
 - j. Transfer 400 μ L of the lysis buffer into I.
 - 2 For 1 replicate and N samples, one needs $3 \times 1.8 \text{ mL} + 0.2 \times N \text{ mL}$ of the BCA working reagent.
 - 3 Mix BCA reagent A with BCA reagent B so as to acquire a A:B mixture of 50:1, i.e., for one sample, mix roughly 1.961 mL A with approximately 0.039 mL B.
 - 4 Transfer 25 μ L of each standard into a separate well in one 96-well microplate.

- 5 Pipette 25 μL of each sample (from the S's, for instance) into the same microplate but in a different row.
- 6 Transfer 200 μL of the A:B mixture into each occupied well.
- 7 Place the microplate on a plate shaker and shake for 30 seconds.
- 8 Cover the microplate with tinfoil and incubate at 37° C for 30 minutes.
- 9 Remove the microplate from the incubator and let it sit at room temperature for 5-15 minutes.
- 10 Using a microplate reader that can read a substance's absorbance, measure the absorbance of the content of each well, using the endpoint option, at 562 nm. Remember to define the blank.
- 11 Copy the numbers upon paper and plot the resulting curves in IgorPro (professional graphing software). Keep in mind that the x-axis is concentration in $\mu\text{g/mL}$. Additionally, the curve should be fit with a line.
- 12 Invert the equation so that the input is the absorbance and the output concentration. Plug-in the absorbance of each sample to determine their protein concentrations.
- 13 Put in 20-50 μg of protein

iii. Gel electrophoresis

- 1 Adjust the protein levels such that each lysate has roughly equal protein concentration. That is, one wants the mass of proteins in one lysate aliquot to equal the mass of proteins in any other lysate aliquot. As such, since we will be using 20 μL aliquots to load into the gels, one should set the volume

of the sample that had the lowest protein concentration to 10 μL and set the product of said concentration with said volume equal to the concentration-volume product for any other sample. This will result in a set of volumes that has as its maximum 10 μL . For example, given the set of concentrations $\{a_1, a_2, a_3\}$, we calculate the volumes necessary to equalize the protein levels, $\{V_{a_1}, V_{a_2}, V_{a_3}\}$, as follows:

$$\min \{a_1, a_2, a_3\} \cdot \max \{V_{a_1}, V_{a_2}, V_{a_3}\} = a_j \cdot V_{a_j} \forall j \in \{1, 2, 3\} \quad (0.24)$$

and solve this equation for V_{a_j} .

- 2 Continuing to use this example, one now mixes $10 - V_{a_j}$ μL of DI H_2O with V_{a_j} μL of sample j . Then, the resulting aliquot is mixed with 10 μL of 1X sample buffer. This is repeated for all j .
- 3 Heat the samples for 5-10 minutes at $95^\circ\text{-}100^\circ\text{ C}$. This should denature the proteins.
- 4 Remove the MC tubes containing the samples from the heating device and allow the samples to reach close to room temperature.
- 5 Place the pre-made gel in the electrophoresis tank (E-tank).
- 6 Fill the upper (front) and lower (back) compartments of the E-tank with 1X running buffer.
- 7 Load the first 2 wells and the last well with 5-10 μL of the protein ladder per well.

- 8 Carefully load the (previously heated) protein samples into the wells of the gel. The volume added to each well depends upon the protein concentration and can vary from roughly 10 μL to 30 μL
 - 9 Apply 200 Volts for 30-45 minutes.
 - 10 Once the dye front reaches the bottom, cease the electrophoresis.
- iv. Dry Protein Transfer (Note: this will not always transfer high molecular weight proteins.)
- 1 Unseal the transfer stack.
 - 2 Set the top stack aside.
 - 3 Set the tray in the iBlot2 and make sure the electrical contacts are aligned.
 - 4 Using gloves, carefully remove the gel from the cassette and place on the membrane in the stack. Note that there is a plastic divider that comes in the stack which is situated atop the membrane. This divider must be removed, else the iBlot2 will not run.
 - 5 Soak the iBlot filter paper with DI H_2O .
 - 6 Place the previously soaked filter paper atop the gel and carefully smooth out/remove air bubbles via a roller.
 - 7 Place the top stack on the filter paper and remove any air bubbles with the roller.
 - 8 Put the absorbent pad on the top of the stack and ensure that the electrical contacts are aligned.

- 9 Choose the desired program and press start. (When relatively high molecular weight proteins are involved, choose a program that takes longer so that the proteins have a greater chance of transferring successfully.)
 - 10 Press “Done” to stop the program once it has finished.
 - 11 Discard the absorbent pad, top stack, gel and the filter paper in a biohazard waste bin.
 - 12 Carefully remove the membrane via tweezers and place it in either DI H₂O or a milk solution.
 - 13 Perform Ponceu staining in order to confirm that the transfer was indeed successful. (The materials should be able to be purchased from Sigma Aldrich.) If the transfer worked, the bands representing the proteins will take on a red tint. If the transfer was faulty, return to step i.1. Otherwise, wash the membrane with TBS-T between one and three times.
- v. Blocking the Membrane
- 1 Prepare a blocking solution made of TBS-T and roughly 5% nonfat (previously dry) milk. This solution shall be called “TBS-T+M.”
 - 2 Immerse/submerge the membrane in some of the TBS-T+M.
 - 3 Place the container holding the membrane on a rocker for 1-2 hours at room temperature.
 - 4 Do not wash the membrane. Instead, pipette out the TBS-T+M. This is very important!
- vi. Probing with Antibodies

- 1 Dilute the primary antibody (PA) in some of the TBS-T mixed with 5% bovine serum albumin (BSA). This mixture of TBS-T and BSA shall henceforth be called “TBS-T+BSA”.
- 2 If using the original PA (which comes in a concentration of 1 mg/mL), then the solution resulting from 1 should be either 1:1,000 PA:TBS-T+BSA or 1:10,000 PA:TBS-T+BSA. Basically, add roughly 5 μ L primary antibody solution to 5 mL of TBS-T+BSA. This results in the “PA+TBS-T+BSA” solution.
- 3 Once the PA+TBS-T+BSA is prepared, add to the blocked membrane in its container.
- 4 Incubate the membrane in PA+TBS-T+BSA on the shaker overnight at 4°.
- 5 Either throw out or recycle the PA. If recycling the PA+TBS-T+BSA solution, one may recycle the solution 3-4 times.
- 6 Wash the membrane 3 times with TBS-T.
- 7 Dilute the secondary antibody (SA) to 1:50,000 in a TBS-T+BSA solution to make a SA+TBS-T+BSA solution. This 2ndary antibody should be HRP-conjugated
- 8 Add the SA+TBS-T+BSA to the container holding the membrane.
- 9 Incubate the membrane in this SA+TBS-T+BSA solution on the shaker for 1 hour.
- 10 Wash the membrane 3 times with TBS-T.

vii. Detection (This step must be performed immediately following vi.)

- 1 Follow the instructions in the Pierce BCA protein assay kit.
- 2 Lay out a large plastic wrap sheet topped by a paper towel. Place the membrane upon this paper towel.
- 3 Add the solution from the last step to the membrane and incubate the membrane for 1 minute. When incubating, the membrane should be wrapped in the paper towel and plastic wrap.
- 4 Dab the membrane on a separate paper towel using tweezers. This is to remove left-over solution.
- 5 Cut a clear plastic bag along its sides. Place the membrane between the two halves of the plastic bag.
- 6 Use the imager to image the blot. Keep in mind that the exposure time affects the band intensities.

vi. Quantification

- 1 Use the beta-actin, or some other housekeeping gene, in order to determine the relative area of the blots.

APPENDIX B

CELL EXTRACT PROCEDURE

i. Cell Culture

- 1 Pre-warm one bottle of complete media, one bottle of trypsin and one bottle of phosphate buffer solution (PBS) to $\sim 37^{\circ}$ C via a warm water bath.
- 2 Open the hood, spray the bottom surface with 70% ethanol and wipe with a paper towel.
- 3 Spray/Drench each container with 70% ethanol, wipe with a paper towel and place in the cell-hood.
- 4 Remove an 80-100% confluent plate from the incubator and gently place in the cell-hood; turn on the aspirator; and re-spray your gloved hands with 70% ethanol.
- 5 Aspirate the media from the plate; wash the plate with 5 mL PBS; and aspirate the PBS from the plate.
- 6 Pipette 2-4 mL of trypsin into the plate; label N+1 new plates with the cell line, the date that the cells were frozen in a cryovial before being thawed and propagated, the date, your initials, the passage number of the cells and either the time of doping or that the plate is a control; and monitor the (old) plate(s) containing trypsin.
- 7 Once the cells have detached from the (old) plate(s), quickly pipette an amount of media which is 3x the amount of trypsin that was placed in the plate, into the plate; wash the plate; and, once the cells have made their way to the a corner

of the plate, transfer the cell-trypsin-media (CTM) solution into a centrifuge tube large enough to contain the CTM solution.

8 Count the cells; this should result in an average number of cells per mL, c , which is used in the following calculation: $c \cdot V_{\text{CTM}} = 5 \times 10^6$ cells, with V_{CTM} the volume of the CTM solution that should be added to each new plate.

9 Transfer V_{CTM} of the CTM solution into each labeled plate; add $25 \text{ mL} - V_{\text{CTM}}$ complete media into each 15 cm plate; gently mix by rocking the plates 10 times forwards and backwards, 10 times side-to-side and repeat once; and place in the incubator.

10 If n is the number of time-points desired in the extract, then repeat until there are at least $n+1$ plates in the incubator.

ii. Doping Plates

1 24 hours after completing step i., pre-warm one bottle of (possibly “special”) complete media and one bottle of PBS; spray/drench with 70% ethanol, wipe away the ethanol with a paper towel and move into the cell-hood after having sprayed and wiped the bottom surface of the cell hood.

2 Remove all plates prepared in i. from the incubator and move them into the cell hood; turn on the aspirator; and spray your gloved hands with 70% ethanol before beginning work in the cell hood.

3 Aspirate the media from all plates; pipette 5 mL of PBS into the corner of each dish and tilt each plate so that the PBS has covered the entire plate; aspirate the PBS from each plate.

4a If using regular complete media (RM), pipette 15 mL of complete media into all dishes except for the plate corresponding to 48 hours; transfer 14 mL complete media into said plate; retrieve a pre-prepared micro-centrifuge tube containing an amount of ^{13}C -labeled substance which will become either 5 or 10 mM when mixed in 15 mL media, spray gingerly with 70% ethanol and bring into the cell hood; mix 1 mL of media in said micro centrifuge tube for at least 10 seconds and centrifuge the solution for 1-2 seconds; and pipette the resulting solution into the plate representing 48 hours.

4b If using special media, pre-prepare a volume equal to $15 \times n$ mL of the non-standard media containing the desired concentration of ^{13}C -labeled metabolite; this media shall be referred to as 13CM. If possible, this concentration should be equivalent to the concentration of natural abundance metabolite which normally comes in the regular/standard media. Additionally, pre-prepare $15 \times n$ mL of the special media with the same concentration of natural abundance metabolite as was used for the previously mentioned ^{13}C -labeled media solution; this solution shall be referred to as NAM. Now, transfer 15 mL of the NAM into each plate except for that corresponding to 48 hours and pipette 15 mL of the 13CM into the plate for 48 hours.

5 Mix all plates via sliding the plates back and forth 10 times and side-to-side 10 times and repeating. Return the plates to the incubator.

6a Let the next time point be # hours. Then, 48-# hours after having doped the 48 hours plate, pipette 1 mL of RM from the plate labeled for # hours into a pre-

prepared micro-centrifuge tube containing enough of the ^{13}C -labeled compound to result in a concentration of 5 or 10 mM once mixed in 15 mL of solvent, mix (for a minimum of 10 s) and centrifuge (for 1-2 s). Transfer the resulting media back into the plate; mix the solution in the plate (via a back and forth motion); and return the plate to the incubator.

6b Let the next time point be # hours. Then, 48-# hours after having doped the 48 hours plate, if using special media, pre-warm the 13CM and PBS to $\sim 37^\circ\text{C}$; spray, wipe and place in the cell hood. Aspirate the NAM from the # hours plate; wash with 5 mL PBS; aspirate the PBS; and add 15 mL of 13CM into the corner of the plate. Mix the solution in the plate (via a back and forth motion); and return the plate to the incubator.

7 Repeat step 6 for each time-point # desired.

iii. Collecting the Extracts

1 Once 48 hours has passed, immediately transfer all the plates involved in the extract into the cell hood. Remove the media either by aspiration (if one is not intending to analyze media extracts) or by transferring the media from each plate into a single 50 mL, labeled centrifuge tube (if one intends to analyze the environs of the cells). The centrifuge tubes should be labeled with the same information as the plates, plus an identifier as to whether they represent media or cells.

2 Since the plates and cells need no longer be kept in sterile conditions, move the cells into a chemical hood (we will be using 12% perchloric acid the vapor of which can cause brain damage). Pipette 5 mL of 12% perchloric acid into each plate

and, if intending to perform media extracts, pipette the same into each centrifuge tube containing media. Tilt the plates to ensure that the acid has covered the entirety of each plate. Mix any media-containing centrifuge tubes and place in a freezer.

3 Use a cell scraper to carefully scrape the cells of each plate into a corner. (Eye protection and a water-slick lab coat should be used for this step since the acid can easily end up on the person scraping.) Without un-tilting the plate, use a serological pipette to transfer the cell-acid solution into a pre-labeled centrifuge tube. Repeat for each plate.

4 Pipette 5 mL of HPLC grade water into each plate and wash the plate. While keeping the plate tilted, transfer the water plus cell remnants into the corresponding centrifuge tube (which should already contain the cell-acid solution). Repeat for each plate. Freeze the resulting centrifuge tubes.

iv. Removing the Large Compounds

1 Centrifuge each 50 mL centrifuge tube at 4000 rpm for 10 minutes.

2 If there is precipitant, transfer the supernatant into a new, pre-labeled 50 mL centrifuge tube.

3 Repeat steps 1 and 2 until the amount of precipitant is sufficiently small. At such a point, cease repetitions and freeze the samples.

v. Neutralization [If the RM, or 13CM with phenol red, was used, then neutralization should be slightly easier: as the phenol red acts as a pH indicator, the task is to turn each solution light pink or slightly yellow. That is, when the sample is purple, it is highly basic (usually with a pH > 10) and when the sample is yellow, it is highly

acidic (typically with a pH <3). However, this is easier to do for someone who has done this neutralization step for at least 12 or so samples. As such, a beginner should stick to the steps below while keeping track of any color changes in the samples.]

1 Thaw all cell/media extract centrifuge tubes in a warm water bath. From here on, the goal is to bring the pH of each sample between 6 and 8. If this is not done properly, then the lyophilization step could harm anyone who enters the room containing the lyophilizer.

2 Once the samples have fully thawed, add 100-200 μL of 8 M NaOH (NAOH) to each centrifuge tube. This is done because the samples start out being very acidic (often with a pH < 1).

3 Mix for at least 5 s. Check the pH using a properly calibrated pH sensor (Oakton Instruments, Vernon Hills, IL).

4a If the pH remains below 1, add 100 μL NaOH. Else if the pH is around 1.5, add 20-50 μL NaOH. Else if the pH is around 2, add 10-20 μL NaOH. If the pH is around 3, but less than 5, add less than or as much as 5 μL NaOH. Finally, if the pH is greater than 4 or 5, add less than 1 μL NaOH. (The point is that the amount of NaOH added should be titrated down to small volumes somewhat quickly because, once the pH hits 1.5 or 2, only a very small amount of NaOH can be added before the sample becomes highly basic.)

4b If the pH is already above 8, but below 9, add at most 5 μL of 12% perchloric acid (PCA). Else if the pH is above 9 but below 10, add 10-20 μL PCA. Else if the

pH is around 10 or 11, add 20-50 μL PCA. If the pH is higher than, say, 11.5, add 100 μL PCA to the sample.

5 Repeat step 3. Repeat step 4 as needed until the pH of any particular sample is between 6 and 8. (If the media contained phenol red, then, starting from the beginning, one should have noticed that as the acidic solution approached the desired pH, a purple color appeared with greater and greater volume as the base was added. Once the solution turned purple, a yellow color should then start appearing with increasing presence the nearer the solution got to a neutral pH.)

6 Repeat until all samples are “neutralized” – i.e., have a pH between 6 and 8. Re-freeze the samples.

vi. Lyophilization [The point of this step is to freeze-dry the samples. Such will result in a residual powder that represents a concentrated version of what was in the cells (if doing a cell extract) or about the cells (if doing a media extract).]

1 Remove the caps from each 50 mL centrifuge tube containing an extract. Place a KimWipe (Kimberly-Clark Professional, Roswell, GA) over the opening and use a rubber band to keep the KimWipe in place.

2 Turn on the lyophilizer. Push the alarm button and clear the entries. Press “Synoptic,” followed by “Freeze.”

3 Wait for the lyophilizer interior to reach roughly -50°C . Once this point has been reached, place the centrifuge tubes upright in the lyophilizer; press “Vacuum” on the lyophilizer panel and turn on the attached vacuum pump.

4 This freeze-drying process will take a few days. Every day, someone should check the status of the samples. Once all samples in the lyophilizer do not appear to contain any more (frozen) liquid, turn off the vacuum pump and press the “Vacuum” button on the lyophilizer console.

5 Vent the lyophilizer so that the vacuum inside vanishes. Remove the samples.

vii. Preparation for NMR

1 Pre-prepare a 15 mL centrifuge tube containing enough ^{13}C urea to reach a concentration of 10 mM in $800 \cdot (n+1) + 100$ μL . Call this sample S.

2 Mix S with $800 \cdot (n+1) + 100$ μL of D_2O .

3 Crush the powder in each 50 mL centrifuge tube containing an extract. Make sure not to accidentally mix the powder remnants of one sample with that of another sample.

4 Pipette 800 μL of the urea-doped D_2O into each 50 mL centrifuge tube containing an extract. Mix for 10-30 s.

5 Transfer 400-500 μL of each sample into a labeled 5 mm NMR tube. If one is dealing with the cell extracts, one can pipette an exact amount of each sample into an NMR tube. However, when dealing with media extracts, the solution will not completely dissolve in the 800 μL of solvent and it may be quite difficult to transfer even 400 μL into the NMR tube.

REFERENCES

- [1] Tom Lancaster and Stephen J. Blundell, *Quantum Field Theory for the Gifted Amateur*. Oxford, UK: Oxford University Press, 2014.
- [2] J. J. Sakurai and Jim Napolitano, *Modern Quantum Mechanics*, 2nd ed. Boston: Addison-Wesley, 2011.
- [3] I. I. Rabi, J. R. Zacharias, S. Millman, and P. Kusch, “A New Method of Measuring Nuclear Magnetic Moment,” *Phys. Rev.*, vol. 53, no. 4, pp. 318–318, Feb. 1938.
- [4] F. Bloch, “Nuclear Induction,” *Phys. Rev.*, vol. 70, no. 7–8, pp. 460–474, Oct. 1946.
- [5] E. M. Purcell, H. C. Torrey, and R. V. Pound, “Resonance Absorption by Nuclear Magnetic Moments in a Solid,” *Phys. Rev.*, vol. 69, no. 1–2, pp. 37–38, Jan. 1946.
- [6] J. Jackson, *Classical Electromagnetism*, 3rd ed. United States: John Wiley & Sons, Ltd.
- [7] Malcolm H. Levitt, *Spin Dynamics: Basics of Nuclear Magnetic Resonance*, 2nd ed. West Sussex: John Wiley & Sons, Ltd, 2008.
- [8] V. I. Bakhmutov, “How and Why Nuclei Relax,” in *Practical NMR Relaxation for Chemists*, John Wiley & Sons, Ltd, 2004, p. 11.
- [9] Paul A. Tipler and Ralph A. Llewellyn, *Modern Physics*, 5th ed. New York: W. H. Freeman, 2008.
- [10] K. Golman and J. S. Petersson, “Metabolic Imaging and Other Applications of Hyperpolarized $^{13}\text{C}1$,” *Acad. Radiol.*, vol. 13, no. 8, pp. 932–942, Aug. 2006.
- [11] Tom Wenckebach, *Essentials of Dynamic Nuclear Polarization*. Netherlands: Spindrift Publications, 2016.
- [12] Franz Schwabl, *Statistical Mechanics*, 3rd ed. Berlin, Heidelberg: Springer-Verlag, 2000.
- [13] K. N. Shrivastava, “Theory of Spin–Lattice Relaxation,” *Phys. Status Solidi B*, vol. 117, no. 2, pp. 437–458, Jun. 1983.
- [14] R. Orbach, “Spin-Lattice Relaxation in Rare-Earth Salts,” *Proc. R. Soc. Lond. Math. Phys. Eng. Sci.*, vol. 264, no. 1319, pp. 458–484, Dec. 1961.
- [15] Horst Friebolin, *Basic One- and Two-Dimensional NMR Spectroscopy*, 2nd ed. Weinheim: VCH Verlagsgesellschaft, 1993.

- [16] N. Bloembergen, “On the interaction of nuclear spins in a crystalline lattice,” *Physica*, vol. 15, no. 3, pp. 386–426, May 1949.
- [17] G. R. Khutsishvili, “SPIN DIFFUSION,” *Sov. Phys. Uspekhi*, vol. 8, no. 5, p. 743, 1966.
- [18] E. P. Horvitz, “Nuclear Spin Diffusion Induced by Paramagnetic Impurities in Nonconducting Solids,” *Phys. Rev. B*, vol. 3, no. 9, pp. 2868–2872, May 1971.
- [19] C. Ramanathan, “Dynamic Nuclear Polarization and Spin Diffusion in Nonconducting Solids,” *Appl. Magn. Reson.*, vol. 34, no. 3, p. 409, Aug. 2008.
- [20] A. Abragam and M. Goldman, “Principles of dynamic nuclear polarisation,” *Rep. Prog. Phys.*, vol. 41, no. 3, p. 395, 1978.
- [21] U. L. Günther, “Dynamic Nuclear Hyperpolarization in Liquids,” in *Modern NMR Methodology*, H. Heise and S. Matthews, Eds. Springer Berlin Heidelberg, 2011, pp. 23–69.
- [22] C. F. Hwang and D. A. Hill, “New Effect in Dynamic Polarization,” *Phys. Rev. Lett.*, vol. 18, no. 4, pp. 110–112, Jan. 1967.
- [23] C. F. Hwang and D. A. Hill, “Phenomenological Model for the New Effect in Dynamic Polarization,” *Phys. Rev. Lett.*, vol. 19, no. 18, pp. 1011–1014, Oct. 1967.
- [24] Y. Hovav, A. Feintuch, and S. Vega, “Theoretical aspects of dynamic nuclear polarization in the solid state – The cross effect,” *J. Magn. Reson.*, vol. 214, pp. 29–41, Jan. 2012.
- [25] S. T. Goertz, “The dynamic nuclear polarization process,” *Nucl. Instrum. Methods Phys. Res. Sect. Accel. Spectrometers Detect. Assoc. Equip.*, vol. 526, no. 1–2, pp. 28–42, Jun. 2004.
- [26] S. C. Serra, A. Rosso, and F. Tedoldi, “Electron and nuclear spin dynamics in the thermal mixing model of dynamic nuclear polarization,” *Phys. Chem. Chem. Phys. PCCP*, vol. 14, no. 38, pp. 13299–13308, Oct. 2012.
- [27] W. T. Wenckebach, “Dynamic nuclear polarization via thermal mixing: Beyond the high temperature approximation,” *J. Magn. Reson.*, vol. 277, pp. 68–78, Apr. 2017.
- [28] S. C. Serra, M. Filibian, P. Carretta, A. Rosso, and F. Tedoldi, “Relevance of electron spin dissipative processes to dynamic nuclear polarization via thermal mixing,” *Phys. Chem. Chem. Phys.*, vol. 16, no. 2, pp. 753–764, Dec. 2013.
- [29] S. C. Serra, A. Rosso, and F. Tedoldi, “On the role of electron–nucleus contact and microwave saturation in thermal mixing DNP,” *Phys. Chem. Chem. Phys.*, vol. 15, no. 21, pp. 8416–8428, May 2013.

- [30] J. Heckmann, W. Meyer, E. Radtke, G. Reicherz, and S. Goertz, "Electron spin resonance and its implication on the maximum nuclear polarization of deuterated solid target materials," *Phys. Rev. B*, vol. 74, no. 13, p. 134418, Oct. 2006.
- [31] Y. Hovav, A. Feintuch, and S. Vega, "Theoretical aspects of dynamic nuclear polarization in the solid state – spin temperature and thermal mixing," *Phys. Chem. Chem. Phys.*, vol. 15, no. 1, pp. 188–203, 2013.
- [32] S. Reynolds and H. Patel, "Monitoring the Solid-State Polarization of ^{13}C , ^{15}N , ^2H , ^{29}Si and ^{31}P ," *Appl. Magn. Reson.*, vol. 34, no. 3–4, pp. 495–508, Aug. 2008.
- [33] L. Lumata, A. K. Jindal, M. E. Merritt, C. R. Malloy, A. D. Sherry, and Z. Kovacs, "DNP by Thermal Mixing under Optimized Conditions Yields >60 000-fold Enhancement of ^{89}Y NMR Signal," *J. Am. Chem. Soc.*, vol. 133, no. 22, pp. 8673–8680, Jun. 2011.
- [34] L. Lumata, M. Merritt, C. Malloy, A. D. Sherry, and Z. Kovacs, "Fast Dissolution Dynamic Nuclear Polarization NMR of ^{13}C -Enriched ^{89}Y -DOTA Complex: Experimental and Theoretical Considerations," *Appl. Magn. Reson.*, vol. 43, no. 1–2, pp. 69–79, Jul. 2012.
- [35] J. Wolber *et al.*, "Generating highly polarized nuclear spins in solution using dynamic nuclear polarization," *Nucl. Instrum. Methods Phys. Res. Sect. Accel. Spectrometers Detect. Assoc. Equip.*, vol. 526, no. 1, pp. 173–181, Jun. 2004.
- [36] S. Macholl, H. Jóhannesson, and J. H. Ardenkjaer-Larsen, "Trityl biradicals and ^{13}C dynamic nuclear polarization," *Phys. Chem. Chem. Phys.*, vol. 12, no. 22, pp. 5804–5817, May 2010.
- [37] F. Kurdzesau *et al.*, "Dynamic nuclear polarization of small labelled molecules in frozen water–alcohol solutions," *J. Phys. Appl. Phys.*, vol. 41, no. 15, p. 155506, 2008.
- [38] J. H. Ardenkjaer-Larsen, S. Macholl, and H. Jóhannesson, "Dynamic Nuclear Polarization with Trityls at 1.2 K," *Appl. Magn. Reson.*, vol. 34, no. 3–4, pp. 509–522, Aug. 2008.
- [39] L. Lumata *et al.*, "BDPA: An Efficient Polarizing Agent for Fast Dissolution Dynamic Nuclear Polarization NMR Spectroscopy," *Chem. – Eur. J.*, vol. 17, no. 39, pp. 10825–10827, Sep. 2011.
- [40] W. de Boer, "Dynamic orientation of nuclei at low temperatures," *J. Low Temp. Phys.*, vol. 22, no. 1–2, pp. 185–212, Jan. 1976.
- [41] A. Karabanov *et al.*, "Dynamic nuclear polarisation by thermal mixing: quantum theory and macroscopic simulations," *Phys. Chem. Chem. Phys.*, vol. 18, no. 43, pp. 30093–30104, Nov. 2016.

- [42] L. Lumata *et al.*, “Electron spin resonance studies of trityl OX063 at a concentration optimal for DNP,” *Phys. Chem. Chem. Phys.*, vol. 15, no. 24, pp. 9800–9807, May 2013.
- [43] J. H. Ardenkjaer-Larsen *et al.*, “Increase in signal-to-noise ratio of > 10,000 times in liquid-state NMR,” *Proc. Natl. Acad. Sci. U. S. A.*, vol. 100, no. 18, pp. 10158–10163, Sep. 2003.
- [44] B. van den Brandt, P. Hautle, J. A. Konter, and F. Kurdzesau, “Dynamic Nuclear Polarization – from Polarized Targets to Metabolic Imaging,” *Appl. Magn. Reson.*, vol. 34, no. 3–4, pp. 475–481, Aug. 2008.
- [45] V. A. Atsarkin, “Dynamic nuclear polarization: Yesterday, today, and tomorrow,” *J. Phys. Conf. Ser.*, vol. 324, no. 1, p. 012003, 2011.
- [46] R. G. Griffin and T. F. Prisner, “High field dynamic nuclear polarization—the renaissance,” *Phys. Chem. Chem. Phys.*, vol. 12, no. 22, pp. 5737–5740, May 2010.
- [47] P. Niedbalski, Q. Wang, C. Parish, F. Khashami, A. Kiswandhi, and L. Lumata, “Magnetic-Field-Dependent Lifetimes of Hyperpolarized ^{13}C Spins at Cryogenic Temperature,” *J. Phys. Chem. B*, vol. 122, no. 6, pp. 1898–1904, Feb. 2018.
- [48] A. Kiswandhi *et al.*, “Construction and ^{13}C hyperpolarization efficiency of a 180 GHz dissolution dynamic nuclear polarization system,” *Magn. Reson. Chem.*, vol. 55, no. 9, pp. 828–836, 2017.
- [49] A. Kiswandhi, P. Niedbalski, C. Parish, Q. Wang, and L. Lumata, “Assembly and performance of a 6.4 T cryogen-free dynamic nuclear polarization system,” *Magn. Reson. Chem.*, vol. 55, no. 9, pp. 846–852, 2017.
- [50] Y. Hovav, A. Feintuch, and S. Vega, “Dynamic nuclear polarization assisted spin diffusion for the solid effect case,” *J. Chem. Phys.*, vol. 134, no. 7, p. 074509, Feb. 2011.
- [51] L. Lumata, Z. Kovacs, C. Malloy, A. D. Sherry, and M. Merritt, “The effect of ^{13}C enrichment in the glassing matrix on dynamic nuclear polarization of [1- ^{13}C]pyruvate,” *Phys. Med. Biol.*, vol. 56, no. 5, p. N85, 2011.
- [52] A. Karabanov, D. Wiśniewski, I. Lesanovsky, and W. Köckenberger, “Dynamic Nuclear Polarization as Kinetically Constrained Diffusion,” *Phys. Rev. Lett.*, vol. 115, no. 2, p. 020404, Jul. 2015.
- [53] M. Gužvić and C. A. Klein, “The Biology of Cancer Metastasis,” in *The Impact of Tumor Biology on Cancer Treatment and Multidisciplinary Strategies*, M. M. MD, P. V. M. MA, C. N. MD, and M. S. A. M. FACRO FACR, Eds. Springer Berlin Heidelberg, 2009, pp. 117–128.

- [54] C. M. Croce, “Oncogenes and Cancer,” *N. Engl. J. Med.*, vol. 358, no. 5, pp. 502–511, Jan. 2008.
- [55] S. B. Baylin and J. E. Ohm, “Epigenetic gene silencing in cancer – a mechanism for early oncogenic pathway addiction?,” *Nat. Rev. Cancer*, vol. 6, no. 2, pp. 107–116, Feb. 2006.
- [56] M. J. Atkinson and S. Tapio, “Tumorigenesis,” in *The Impact of Tumor Biology on Cancer Treatment and Multidisciplinary Strategies*, M. M. MD, P. V. M. MA, C. N. MD, and M. S. A. M. FACRO FACR, Eds. Springer Berlin Heidelberg, 2009, pp. 1–17.
- [57] A. G. Knudson, “Two genetic hits (more or less) to cancer,” *Nat. Rev. Cancer*, vol. 1, no. 2, pp. 157–162, Nov. 2001.
- [58] L. M. F. Merlo, J. W. Pepper, B. J. Reid, and C. C. Maley, “Cancer as an evolutionary and ecological process,” *Nat. Rev. Cancer*, vol. 6, no. 12, pp. 924–935, Dec. 2006.
- [59] D. Hanahan and R. A. Weinberg, “The Hallmarks of Cancer,” *Cell*, vol. 100, no. 1, pp. 57–70, Jan. 2000.
- [60] D. Hanahan and R. A. Weinberg, “Hallmarks of Cancer: The Next Generation,” *Cell*, vol. 144, no. 5, pp. 646–674, Mar. 2011.
- [61] P. Diaconis and F. Mosteller, “Methods for Studying Coincidences,” *J. Am. Stat. Assoc.*, vol. 84, no. 408, pp. 853–861, Dec. 1989.
- [62] C. Bernstein, A. R. Prasad, V. Nfonsam, and H. Bernstein, “DNA Damage, DNA Repair and Cancer,” *New Res. Dir. DNA Repair*, May 2013.
- [63] Gertrude McKee and James R. McKee, *Biochemistry: The Molecular Basis of Life - 3rd edition*, 3rd ed. Boston: McGraw-Hill Publishing Company, 2003.
- [64] E. Buxbaum, “Amino acids,” in *Fundamentals of Protein Structure and Function*, Springer US, 2007, pp. 3–11.
- [65] I. Wagner and H. Musso, “New Naturally Occurring Amino Acids,” *Angew. Chem. Int. Ed. Engl.*, vol. 22, no. 11, pp. 816–828, Nov. 1983.
- [66] A. Ambrogelly, S. Palioura, and D. Söll, “Natural expansion of the genetic code,” *Nat. Chem. Biol.*, vol. 3, no. 1, pp. 29–35, Jan. 2007.
- [67] D. Cota *et al.*, “Hypothalamic mTOR Signaling Regulates Food Intake,” *Science*, vol. 312, no. 5775, pp. 927–930, 2006.
- [68] K. A. Massey, C. H. Blakeslee, and D. H. S. Pitkow, “A review of physiological and metabolic effects of essential amino acids,” *Amino Acids*, vol. 14, no. 4, pp. 271–300, Dec. 1998.

- [69] J. K. Stechmiller, B. Childress, and L. Cowan, "Arginine Supplementation and Wound Healing," *Nutr. Clin. Pract.*, vol. 20, no. 1, pp. 52–61, Feb. 2005.
- [70] J. C. Aledo, "Glutamine breakdown in rapidly dividing cells: waste or investment?," *BioEssays*, vol. 26, no. 7, pp. 778–785, Jul. 2004.
- [71] Mariia Yuneva, Nicola Zamboni, Peter Oefner, Ravi Sachidanandam, and Yuri Lazebnik, "Deficiency in glutamine but not glucose induces MYC-dependent apoptosis in human cells," *J. Cell Biol.*, vol. 178, no. 1, pp. 93–105, 2007.
- [72] J. T. Brosnan, "Interorgan Amino Acid Transport and its Regulation," *J. Nutr.*, vol. 133, no. 6, pp. 2068S-2072S, Jun. 2003.
- [73] D. Nelson and M. Cox, *Principles of Biochemistry*, 4th ed. New York: W. H. Freeman, 2005.
- [74] G. Wu, "Amino acids: metabolism, functions, and nutrition," *Amino Acids*, vol. 37, no. 1, pp. 1–17, Mar. 2009.
- [75] M. Akram, "Citric Acid Cycle and Role of its Intermediates in Metabolism," *Cell Biochem. Biophys.*, vol. 68, no. 3, pp. 475–478, Sep. 2013.
- [76] Y. Li and D. Zhao, "Basics of Molecular Biology," in *Molecular Imaging*, Springer Berlin Heidelberg, 2013, pp. 541–601.
- [77] E. Buxbaum, "Protein structure," in *Fundamentals of Protein Structure and Function*, Springer US, 2007, pp. 13–37.
- [78] I. Amelio, F. Cutruzzolá, A. Antonov, M. Agostini, and G. Melino, "Serine and glycine metabolism in cancer," *Trends Biochem. Sci.*, vol. 39, no. 4, pp. 191–198, Apr. 2014.
- [79] M. Jain *et al.*, "Metabolite Profiling Identifies a Key Role for Glycine in Rapid Cancer Cell Proliferation," *Science*, vol. 336, no. 6084, pp. 1040–1044, May 2012.
- [80] D. R. Wise and C. B. Thompson, "Glutamine addiction: a new therapeutic target in cancer," *Trends Biochem. Sci.*, vol. 35, no. 8, pp. 427–433, Aug. 2010.
- [81] M. E. Brosnan and J. Letto, "Interorgan metabolism of valine," *Amino Acids*, vol. 1, no. 1, pp. 29–35, Feb. 1991.
- [82] "Deprivation of arginine by recombinant human arginase in prostate cancer cells," *J. Hematol. Oncol. J Hematol Oncol*, vol. 5, no. 1, pp. 17–22, Jan. 2012.
- [83] C. S. Ahn and C. M. Metallo, "Mitochondria as biosynthetic factories for cancer proliferation," *Cancer Metab.*, vol. 3, p. 1, Jan. 2015.

- [84] J. O. Mecham, D. Rowitch, C. D. Wallace, P. H. Stern, and R. M. Hoffman, "The metabolic defect of methionine dependence occurs frequently in human tumor cell lines," *Biochem. Biophys. Res. Commun.*, vol. 117, no. 2, pp. 429–434, Dec. 1983.
- [85] T. Kato *et al.*, "Expression of mRNAs for *c-myc* and Branched-Chain Aminotransferases in Human Gastric Cancer Cells and Tissues," *J. Clin. Biochem. Nutr.*, vol. 29, pp. 29–36, 2000.
- [86] J. R. Mayers *et al.*, "Elevation of circulating branched-chain amino acids is an early event in human pancreatic adenocarcinoma development," *Nat. Med.*, vol. 20, no. 10, pp. 1193–1198, Oct. 2014.
- [87] A. R. Tee, "Metastatic Castration-Resistant Prostate Cancer Hungers for Leucine," *J. Natl. Cancer Inst.*, vol. 105, no. 19, pp. 1427–1428, Oct. 2013.
- [88] Y. Nishio, T. Kakizoe, M. Ohtani, S. Sato, T. Sugimura, and S. Fukushima, "L-Isoleucine and L-Leucine: Tumor Promoters of Bladder Cancer in Rats," *Science*, vol. 231, no. 4740, pp. 843–845, 1986.
- [89] T. Nishihira *et al.*, "Anti-Cancer Therapy with Valine-Depleted Amino Acid Imbalance Solution," *Tohoku J. Exp. Med.*, vol. 156, no. 3, pp. 259–270, 1988.
- [90] M.-B. Tessem *et al.*, "Evaluation of lactate and alanine as metabolic biomarkers of prostate cancer using ¹H HR-MAS spectroscopy of biopsy tissues," *Magn. Reson. Med.*, vol. 60, no. 3, pp. 510–516, Sep. 2008.
- [91] B. Vogelstein, N. Papadopoulos, S. Velculescu Victor E., L. A. Diaz Jr., and K. W. Kinzler, "Cancer Genome Landscapes," *Science*, vol. 339, no. 6127, pp. 1546–1558, Mar. 2013.
- [92] L. Lumata, M. E. Merritt, and Z. Kovacs, "Influence of deuteration in the glassing matrix on ¹³C dynamic nuclear polarization," *Phys. Chem. Chem. Phys.*, vol. 15, no. 19, p. 7032, 2013.
- [93] A. Kiswandhi, B. Lama, P. Niedbalski, M. Goderya, J. Long, and L. Lumata, "The effect of glassing solvent deuteration and Gd³⁺ doping on ¹³C DNP at 5 T," *RSC Adv.*, vol. 6, no. 45, pp. 38855–38860, Apr. 2016.
- [94] P. Niedbalski, C. Parish, A. Kiswandhi, Z. Kovacs, and L. Lumata, "Influence of ¹³C Isotopic Labeling Location on Dynamic Nuclear Polarization of Acetate," *J. Phys. Chem. A*, vol. 121, no. 17, pp. 3227–3233, May 2017.
- [95] A. A. Sirusi, E. Hyun Suh, Z. Kovacs, and M. E. Merritt, "The effect of Ho ³⁺ doping on ¹³C dynamic nuclear polarization at 5 T," *Phys. Chem. Chem. Phys.*, vol. 20, no. 2, pp. 728–731, 2018.

- [96] A. Flori, M. Liserani, S. Bowen, J. H. Ardenkjaer-Larsen, and L. Menichetti, "Dissolution Dynamic Nuclear Polarization of Non-Self-Glassing Agents: Spectroscopy and Relaxation of Hyperpolarized [1-13C]Acetate," *J. Phys. Chem. A*, vol. 119, no. 10, pp. 1885–1893, Mar. 2015.
- [97] P. Niedbalski *et al.*, "Enhanced Efficiency of 13C Dynamic Nuclear Polarization by Superparamagnetic Iron Oxide Nanoparticle Doping," *J. Phys. Chem. C*, vol. 121, no. 35, pp. 19505–19511, Sep. 2017.
- [98] V. I. Bakhmutov, "NMR Relaxation by Dipole–Dipole and Quadrupole Interactions," in *Practical NMR Relaxation for Chemists*, John Wiley & Sons, Ltd, 2004, pp. 43–58.
- [99] C. Parish, P. Niedbalski, A. Kiswandhi, and L. Lumata, "Dynamic nuclear polarization of carbonyl and methyl 13C spins of acetate using 4-oxo-TEMPO free radical," *J. Chem. Phys.*, vol. 149, no. 5, p. 054302, Aug. 2018.
- [100] L. Lumata, M. E. Merritt, C. R. Malloy, A. D. Sherry, and Z. Kovacs, "The Impact of Gd3+ on DNP of [1-13C]Pyruvate Doped with Trityl OX063, BDPA, or 4-Oxo-TEMPO," *J. Phys. Chem. A*, vol. 116, no. 21, pp. 5129–5138, May 2012.
- [101] J. A. M. Bastiaansen, T. Cheng, M. Mishkovsky, J. M. N. Duarte, A. Comment, and R. Gruetter, "In vivo enzymatic activity of acetylCoA synthetase in skeletal muscle revealed by 13C turnover from hyperpolarized [1-13C]acetate to [1-13C]acetylcarnitine," *Biochim. Biophys. Acta BBA - Gen. Subj.*, vol. 1830, no. 8, pp. 4171–4178, Aug. 2013.
- [102] H. M. Mizioro, "Enzymes of the mevalonate pathway of isoprenoid biosynthesis," *Arch. Biochem. Biophys.*, vol. 505, no. 2, pp. 131–143, Jan. 2011.
- [103] M. Mishkovsky, A. Comment, and R. Gruetter, "In vivo detection of brain Krebs cycle intermediate by hyperpolarized magnetic resonance," *J. Cereb. Blood Flow Metab.*, vol. 32, no. 12, pp. 2108–2113, Dec. 2012.
- [104] L. Lumata, C. Yang, M. Ragavan, N. Carpenter, R. J. DeBerardinis, and M. E. Merritt, "Chapter Two - Hyperpolarized 13C Magnetic Resonance and Its Use in Metabolic Assessment of Cultured Cells and Perfused Organs," in *Methods in Enzymology*, vol. 561, C. M. Metallo, Ed. Academic Press, 2015, pp. 73–106.
- [105] E. R. Andrew, "Magic Angle Spinning," *Int. Rev. Phys. Chem.*, vol. 1, no. 2, pp. 195–224, Aug. 1981.
- [106] E. R. Andrew, A. Bradbury, and R. G. Eades, "Nuclear Magnetic Resonance Spectra from a Crystal rotated at High Speed," *Nature*, vol. 182, p. 1659, Dec. 1958.

- [107] F. Mentink-Vigier, Ü. Akbey, H. Oschkinat, S. Vega, and A. Feintuch, “Theoretical aspects of Magic Angle Spinning - Dynamic Nuclear Polarization,” *J. Magn. Reson.*, vol. 258, pp. 102–120, Sep. 2015.
- [108] † Changsik Song, † Kan-Nian Hu, ‡ Chan-Gyu Joo, † and Timothy M. Swager, and * Robert G. Griffin, “TOTAPOL: A Biradical Polarizing Agent for Dynamic Nuclear Polarization Experiments in Aqueous Media,” 16-Aug-2006. [Online]. Available: <http://pubs.acs.org/doi/abs/10.1021/ja061284b>. [Accessed: 11-Aug-2016].
- [109] K.-N. Hu, H. Yu, T. M. Swager, and R. G. Griffin, “Dynamic Nuclear Polarization with Biradicals,” *J. Am. Chem. Soc.*, vol. 126, no. 35, pp. 10844–10845, Sep. 2004.
- [110] K.-N. Hu, V. S. Bajaj, M. Rosay, and R. G. Griffin, “High-frequency dynamic nuclear polarization using mixtures of TEMPO and trityl radicals,” *J. Chem. Phys.*, vol. 126, no. 4, p. 044512, Jan. 2007.
- [111] V. K. Michaelis, A. A. Smith, B. Corzilius, O. Haze, T. M. Swager, and R. G. Griffin, “High-Field ¹³C Dynamic Nuclear Polarization with a Radical Mixture,” *J. Am. Chem. Soc.*, vol. 135, no. 8, pp. 2935–2938, Feb. 2013.
- [112] K.-N. Hu, C. Song, H. Yu, T. M. Swager, and R. G. Griffin, “High-frequency dynamic nuclear polarization using biradicals: A multifrequency EPR lineshape analysis,” *J. Chem. Phys.*, vol. 128, no. 5, p. 052302, Jan. 2008.
- [113] E. L. Dane, T. Maly, G. T. Debelouchina, R. G. Griffin, and T. M. Swager, “Synthesis of a BDPA-TEMPO Biradical,” *Org. Lett.*, vol. 11, no. 9, pp. 1871–1874, May 2009.
- [114] S. Lange *et al.*, “The effect of biradical concentration on the performance of DNP-MAS-NMR,” *J. Magn. Reson.*, vol. 216, pp. 209–212, Mar. 2012.
- [115] E. L. Dane *et al.*, “Rigid Orthogonal Bis-TEMPO Biradicals with Improved Solubility for Dynamic Nuclear Polarization,” *J. Org. Chem.*, vol. 77, no. 4, pp. 1789–1797, Feb. 2012.
- [116] J.-L. Muñoz-Gómez, I. Marín-Montesinos, V. Lloveras, M. Pons, J. Vidal-Gancedo, and J. Veciana, “Novel PTM-TEMPO Biradical for Fast Dissolution Dynamic Nuclear Polarization,” *Org. Lett.*, vol. 16, no. 20, pp. 5402–5405, Oct. 2014.
- [117] L. F. Pinto *et al.*, “NMR signal enhancement of >50000 times in fast dissolution dynamic nuclear polarization,” *Chem. Commun.*, vol. 53, no. 26, pp. 3757–3760, 2017.
- [118] C. T. Farrar, D. A. Hall, G. J. Gerfen, S. J. Inati, and R. G. Griffin, “Mechanism of dynamic nuclear polarization in high magnetic fields,” *J. Chem. Phys.*, vol. 114, no. 11, pp. 4922–4933, Mar. 2001.

- [119] T. A. Siaw *et al.*, “Effect of electron spin dynamics on solid-state dynamic nuclear polarization performance,” *Phys. Chem. Chem. Phys.*, vol. 16, no. 35, pp. 18694–18706, Aug. 2014.
- [120] J. P. Wolfe, “Direct Observation of a Nuclear Spin Diffusion Barrier,” *Phys. Rev. Lett.*, vol. 31, no. 15, pp. 907–910, Oct. 1973.
- [121] P. Niedbalski *et al.*, “Influence of Dy³⁺ and Tb³⁺ doping on ¹³C dynamic nuclear polarization,” *J. Chem. Phys.*, vol. 146, no. 1, p. 014303, Jan. 2017.
- [122] P. Niedbalski *et al.*, “¹³C Dynamic Nuclear Polarization Using a Trimeric Gd³⁺ Complex as an Additive,” *J. Phys. Chem. A*, vol. 121, no. 27, pp. 5127–5135, Jul. 2017.
- [123] J. G. Salway, *Metabolism at a Glance*, 2nd ed. Oxford: Blackwell Science Limited, 1994.
- [124] D. M. Wilson and J. Kurhanewicz, “Hyperpolarized ¹³C MR for Molecular Imaging of Prostate Cancer,” *J. Nucl. Med.*, vol. 55, no. 10, pp. 1567–1572, Oct. 2014.
- [125] P. Dutta, G. V. Martinez, and R. J. Gillies, “A new horizon of DNP technology: application to in-vivo ¹³C magnetic resonance spectroscopy and imaging,” *Biophys. Rev.*, vol. 5, no. 3, pp. 271–281, Jan. 2013.
- [126] J. R. Mayers *et al.*, “Tissue of origin dictates branched-chain amino acid metabolism in mutant Kras-driven cancers,” *Science*, vol. 353, no. 6304, pp. 1161–1165, Sep. 2016.
- [127] A. Hattori *et al.*, “Cancer progression by reprogrammed BCAA metabolism in myeloid leukaemia,” *Nature*, vol. 545, no. 7655, pp. 500–504, May 2017.
- [128] M. Tönjes *et al.*, “BCAT1 promotes cell proliferation through amino acid catabolism in gliomas carrying wild-type IDH1,” *Nat. Med.*, vol. 19, no. 7, pp. 901–908, Jul. 2013.
- [129] M. Karlsson *et al.*, “Imaging of branched chain amino acid metabolism in tumors with hyperpolarized ¹³C ketoisocaproate,” *Int. J. Cancer*, vol. 127, no. 3, pp. 729–736, Aug. 2010.
- [130] Q. Wang *et al.*, “Targeting Amino Acid Transport in Metastatic Castration-Resistant Prostate Cancer: Effects on Cell Cycle, Cell Growth, and Tumor Development,” *JNCI J. Natl. Cancer Inst.*, vol. 105, no. 19, pp. 1463–1473, Oct. 2013.
- [131] A. Eden and N. Benvenisty, “Involvement of branched-chain amino acid aminotransferase (Bcat1/Eca39) in apoptosis,” *FEBS Lett.*, vol. 457, no. 2, pp. 255–261, Aug. 1999.
- [132] A. Hattori, T. Ito, and M. Tsunoda, “Analysis of Branched-Chain Keto Acids in Cell Extracts by HPLC-Fluorescence Detection,” *Chromatography*, vol. advpub, 2017.

[133] “Branched chain amino acid transaminase 1,” *Wikipedia*. 06-Aug-2018.

BIOGRAPHICAL SKETCH

After overcoming the learning disabilities dyslexia and attention deficit hyperactivity disorder and the psychiatric disability obsessive compulsive disorder at a young age, Christopher Parish entered Hirschi High School only to be confronted with a diagnosis of Ewing's sarcoma (PNET) at the age of seventeen. Following a year of chemotherapy, he went into remission and entered Midwestern State University of Wichita Falls in 2006. He received a BS with a double major in mathematics and physics and a minor in chemistry in 2011. After enduring another diagnosis of PNET, with a year of requisite chemotherapy, he earned his MS from The University of Texas at Dallas in 2013. He entered the Ph.D. program in biophysics at The University of Texas at Dallas in 2013. He is currently in remission. His research interests include general cancer research and NMR, quantum field theory, time, information theory and graph theory.

CURRICULUM VITAE

Christopher Richard Parish

Education

PhD in Physics candidate –The University of Texas at Dallas, Richardson, TX (Expected PhD Defense in April 2019)

Master of Science in Physics – December 2014

University of Texas at Dallas, Richardson, TX

Bachelor of Science in Physics and in Mathematics (double major), Chemistry minor – May 2011

Midwestern State University, Wichita Falls, TX

Honors and Affiliations

Phi Kappa Phi academic honor society, 2018-present

Margie Renfrow Scholarship, 2017

Experimental NMR Conference Travel Award, 2017

Margie Renfrow Scholarship, 2016

Golden Key international honor society, 2013 – present

Sigma Pi Sigma physics honor society, 2010 – present

American Society of Physics Students, 2010 – present

Pi Mu Epsilon mathematics honor society, 2009 – present

American Chemical Society, 2009 – 2011

Alpha Lambda Delta and Phi Eta Sigma academic honor societies, 2007 – 2011

MSU Presidential Leadership Scholar and Honors Program Scholar, 2006 – 2011

American Cancer Society Texas Young Adult Cancer Survivor Scholar, 2006 – 2011

The Cancer Survivors' Fund Texas Scholar, 2006 – 2011

Research Interests

- Biophysics, especially as related to cancer diagnosis and treatment
- Quantum information theory
- Classical and quantum gravity
- Solid state physics
- Mathematical generalizations of Linear Algebra
- Nuclear Magnetic Resonance, especially unusual applications of NMR

Teaching Interests

- Physics at a college or university, preferably a graduate school
- Graduate, or even undergraduate, quantum mechanics, NMR/MRI or condensed matter courses

Research Experience

Research Classes, Department of Physics, University of Texas at Dallas, Richardson, TX

August 2014 – present

- Currently assisting in biophysical research with Lloyd Lumata, PhD, Assistant Professor
- Assisted in derivations for a cold atom gas in a static lattice coupled with a moving lattice research with Chuanwei Zhang, PhD, Associate Professor, in Fall 2014

Research Assistant, Department of Physics, University of Texas at Dallas, Richardson, TX

January – May 2013; January 2015 – present

- Currently researching applications of spectroscopic and imaging techniques to cancer diagnosis under supervision of Lloyd Lumata, PhD, Associate Professor
- Gained research-related coding experience under supervision of Lindsay King, PhD, Associate Professor

Volunteer Research Assistant, Department of Mathematics, Midwestern State University, Wichita Falls,

TX

January – August 2011

- Performed undergraduate research in mathematics concerning near-rings with Michelle Knox, PhD, Associate Professor

Research Participant, Department of Hematology and Oncology, Cook Children's Medical Center, Fort Worth, TX

February – December 2005

- Participated in Ewing's sarcoma clinical research trial under direction of Jeffrey Murray, M.D., Adolescent and Young Adult Oncology Specialist
- Received fourteen regimens of inpatient chemotherapy in standard vs shortened interval protocol
- Contributed follow-up personal data and tissue samples 2006 – 2013

Teaching Experience

Mentor, Department of Physics, University of Texas at Dallas, Richardson, TX

June 2017 – August 2018

- Guided 1 NSF REU (undergraduate student) in researching and presenting the metabolic role of [U-¹³C₆] glucose in SfXL cells within the Lumata Lab, between May 2018 and August 2018.
- Guided 2 UTD nano-explorers (high school students) in researching and presenting the metabolic role of glutamate, [1-¹³C] alpha-ketoisocaproate and [1-¹³C] alpha-ketoisovalerate in HUH7 (liver) cancer cells within the Lumata Lab, between June 2018 and August 2018.
- Guided a Welch scholar (a high school student) in researching, writing and presenting the metabolic role of [1-¹³C] alanine and ¹³C₃ sodium pyruvate in SfXL (brain) cancer cells within the Lumata Lab, between May 2018 and June 2018.
- Guided a high school student in researching and presenting the metabolic role of [U-¹³C₆] glucose and [1-¹³C] fructose in SfXL (brain) and PC-3 (prostate) cancer cells within the Lumata Lab, between August 2017 and May 2018. Said student presented her research at a Texas section APS conference.
- Guided 2 UTD nano-explorers (high school students) in researching and presenting on T₁s of different lanthanides and of transition metals within the Lumata Lab, between June 2017 and August 2017.
- Guided a Welch scholar (a high school student) in research and how to present said research.

Teaching Assistant, Department of Physics, University of Texas at Dallas, Richardson, TX

August 2017 – May 2018; August 2014 – May 2015; August – December 2012; January – May 2012

- Graded class quizzes and tests under supervision of Lloyd Lumata, PhD, Assistant Professor, in August 2017 – May 2018.

- Aided students individually with homework and graded assignments for Phillip Anderson, PhD, Professor, in Spring 2015
- Assisted with grading assignments for David Lary, PhD, Associate Professor, in Fall 2014
- Supervised student laboratory sessions and graded lab reports under direction of Paul MacAlevy, PhD, Senior Lecturer, in Fall 2012
- Conducted class review sessions and graded tests under supervision of Lindsay King, PhD, Associate Professor, in Spring 2012

Teaching Assistant, Hirschi IB Math and Science High School, Wichita Falls, TX

January – May 2006

- Assisted teacher Thea Griffin in International Baccalaureate Biology class
- Prepared classroom laboratory for student experiments

Peer-Reviewed Publications:

1. "Effects of glassing matrix deuteration on the relaxation properties of hyperpolarized ^{13}C spins and free radical electrons at cryogenic temperatures" Christopher Parish, Peter Niedbalski, Qing Wang, Fatemeh Khashami, Zahra Hayati, Mengtian Liu, Likai Song and Lloyd Lumata* (Submitted to *Journal of Chemical Physics*).
2. "Dynamic nuclear polarization of carboxyl and methyl ^{13}C Spins of acetate using 4-oxo-TEMPO free radical" Christopher Parish, Peter Niedbalski, Anhdika Kiswandhi, and Lloyd Lumata*, *Journal of Chemical Physics* **149**, 054302 (2018).
3. "NMR Spectroscopy Unchained: Attaining the Highest Signal Enhancements in Dissolution Dynamic Nuclear Polarization" Peter Niedbalski, Anhdika Kiswandhi, Christopher Parish, Qing Wang, Fatemeh Khashami, and Lloyd Lumata*, *The Journal of Physical Chemistry Letters* **9**, 5481-5489 (2018).
4. "Magnetic Field-Dependent Lifetimes of Hyperpolarized ^{13}C Spins at Cryogenic Temperature" Peter Niedbalski, Qing Wang, Christopher Parish, Fatemeh Khashami, Anhdika Kiswandhi, and Lloyd Lumata*, *Journal of Physical Chemistry B* **122**, 1898-1904 (2018).
5. "Transition Metal Doping Reveals Link between Electron T_1 Reduction and ^{13}C Dynamic Nuclear Polarization Efficiency" Peter Niedbalski, Christopher Parish, Qing Wang, Zahra Hayati, Likai Song, Andre Martins, A. Dean Sherry, and Lloyd Lumata*, *Journal of Physical Chemistry A* **121**, 9221-9228 (2017).
6. "Enhanced Efficiency of ^{13}C Dynamic Nuclear Polarization by Superparamagnetic Iron Oxide Nanoparticle Doping" Peter Niedbalski, Christopher Parish, Qing Wang, Zahra Hayati, Likai Song, Zackary I. Cleveland, and Lloyd Lumata*, *Journal of Physical Chemistry C* **121**, 19505-19511 (2017).
7. " ^{13}C dynamic nuclear polarization using derivatives of TEMPO free radical" Peter Niedbalski, Christopher Parish, Qing Wang, Anhdika Kiswandhi, and Lloyd Lumata*, *Applied Magnetic Resonance* **48**, 933-942 (2017).
8. " ^{13}C dynamic nuclear polarization using a trimeric gadolinium complex as an additive" Peter Niedbalski, Christopher Parish, Qing Wang, Anhdika Kiswandhi, Zahra Hayati, Likai Song, and Lloyd Lumata*, *Journal of Physical Chemistry A* **121**, 5127-5135 (2017).

9. "Assembly and performance of a 6.4 T cryogen-free dynamic nuclear polarization system" Andhika Kiswandhi, Peter Niedbalski, Qing Wang, Christopher Parish, and Lloyd Lumata*, *Magnetic Resonance in Chemistry-Rapid Communication* **55**, 846-852 (2017).
10. "Influence of ^{13}C isotopic labeling location on dynamic nuclear polarization of acetate" Peter Niedbalski, Christopher Parish, Andhika Kiswandhi, Zoltan Kovacs, and Lloyd Lumata*, *Journal of Physical Chemistry A* **121**, 3227-3233 (2017).
11. "Construction and ^{13}C hyperpolarization efficiency of a 180 GHz dissolution dynamic nuclear polarization system" Andhika Kiswandhi, Peter Niedbalski, Christopher Parish, Sarah Ferguson, David Taylor, George McDonald, and Lloyd Lumata*, *Magnetic Resonance in Chemistry* **55**, 828-836 (2017).
12. "Influence of Dy^{3+} and Tb^{3+} -doping on ^{13}C dynamic nuclear polarization" Peter Niedbalski, Christopher Parish, Andhika Kiswandhi, Leila Fidelino, Chalermchai Khemtong, Zahra Hayati, Likai Song, Andre Martins, A. Dean Sherry, and Lloyd Lumata*, *Journal of Chemical Physics* **146**, 014303 (2017).
13. "Impact of Ho^{3+} -doping on ^{13}C dynamic nuclear polarization using trityl OX063 free radical" Andhika Kiswandhi, Peter Niedbalski, Christopher Parish, Pavanjeet Kaur, Andre Martins, Leila Fidelino, Chalermchai Khemtong, Likai Song, A. Dean Sherry, and Lloyd Lumata*, *Physical Chemistry Chemical Physics* **18**, 21351-21359 (2016).
14. " ^{13}C dynamic nuclear polarization using isotopically-enriched 4-oxo-TEMPO free radicals" Peter Niedbalski, Christopher Parish, Andhika Kiswandhi and Lloyd Lumata*, *Magnetic Resonance in Chemistry* **54**, 962-967 (2016).
15. "Influence of ^{13}C nuclear spin density on NMR signal enhancement and relaxation of hyperpolarized [1- ^{13}C] pyruvic acid" Christopher Parish, Peter Niedbalski, Qing Wang, Likai Song, and Lloyd Lumata* (*Submitted to Physics in Medicine and Biology*).

Ongoing Projects

1. " ^{13}C Dynamic Nuclear Polarization using a mixture of Trityl OX063 and 4-Oxo-TEMPO" Christopher Parish, Peter Niedbalski, Qing Wang, Andhika Kiswandhi, Zahra Hayati, Likai Song and Lloyd Lumata*.
2. " ^{13}C Dynamic Nuclear Polarization using BDPA and trityl OX063" Christopher Parish, Peter Niedbalski, Andhika Kiswandhi, Qing Wang, Fatemeh Khashami and Lloyd Lumata*.

Presentations/Talks/Posters/Abstracts

1. **Effect of Solvent Deuteration upon Nuclear and Electronic Spin-Lattice Relaxation Times**, Christopher Parish, Peter Niedbalski, Qing Wang, Lloyd Lumata, and Likai Song, Experimental NMR Conference (ENC), Grand Cypress Hotel, Orlando, Florida (April 29 – May 4, 2018).
2. **^{13}C Dynamic Nuclear Polarization Using BDPA and trityl OX063**, Christopher Parish, Peter Niedbalski, Andhika Kiswandhi, Qing Wang, Fatemeh Khashami, and Lloyd Lumata, Experimental NMR Conference (ENC), Grand Cypress Hotel, Orlando, Florida (April 29 – May 4, 2018).
3. **Tracking leucine metabolism in cancer cells via ^{13}C NMR spectroscopy**, Christopher Parish, Peter Niedbalski, Fatemeh Khashami, Qing Wang, Aya Cloyd, and Lloyd Lumata, 51st Annual

- American Chemical Society-DFW meeting, Southern Methodist University, Dallas, Texas (April 21, 2018).
4. **^{13}C dynamic nuclear polarization using a mixture of BDPA and trityl OX063**, Christopher Parish, Peter Niedbalski, Qing Wang, Fatemeh Khashami, and Lloyd Lumata, Texas Section of the American Physical Society (APS) meeting, University of Texas at Dallas, Richardson, Texas (October 20-21, 2017).
 5. **Tracking leucine metabolism in prostate cancer cells via ^{13}C NMR spectroscopy**, Christopher Parish, Peter Niedbalski, Qing Wang, Fatemeh Khashami, and Lloyd Lumata, Texas Section of the American Physical Society (APS) meeting, University of Texas at Dallas, Richardson, Texas (October 20-21, 2017).
 6. **Mechanisms of dynamic nuclear polarization using a mixture of two free radicals**, Christopher Parish, Peter Niedbalski, Qing Wang, and Lloyd Lumata, 50th Annual American Chemical Society-DFW meeting, Texas Christian University, Fort Worth, Texas (April 29, 2017).
 7. **^{13}C dynamic nuclear polarization using a mixture of trityl OX063 and 4-oxo-TEMPO at 3.35 T and 1.2 K**, Christopher Parish, Peter Niedbalski, Qing Wang, Zahra Hayati, Likai Song, Andhika Kiswandhi, and Lloyd Lumata, 58th Experimental NMR Conference (ENC), Asilomar, California (March 26-31, 2017).
 8. **^{13}C dynamic nuclear polarization using a mixture of trityl OX063 and 4-oxo-TEMPO free radicals**, Christopher Parish, Peter Niedbalski, Qing Wang, Andhika Kiswandhi, and Lloyd Lumata, Southwest Regional Meeting of the American Chemical Society (ACS), Galveston Convention Center, Galveston, Texas (November 10-13, 2016).
 9. **Influence of ^{13}C isotopic labeling location on ^{13}C DNP of acetate using TEMPO free radical**, Christopher Parish, Peter Niedbalski, Zoltan Kovacs, and Lloyd Lumata, Experimental NMR Conference (ENC), Wyndham Grand Hotel, Pittsburgh, Pennsylvania (April 10-15, 2016).
 10. **Real-time tracking of dissociation of hyperpolarized ^{89}Y -DTPA: a model for degradation of open-chain Gd^{3+} MRI contrast agents**, Christopher Parish, Sarah Ferguson, Peter Niedbalski, Andhika Kiswandhi, Zoltan Kovacs, and Lloyd Lumata, Experimental NMR Conference (ENC), Wyndham Grand Hotel, Pittsburgh, Pennsylvania (April 10-15, 2016).
 11. **Hyperpolarized ^{13}C NMR lifetimes in the liquid-state: relating structures and T_1 relaxation times**, Christopher Parish, Peter Niedbalski, Zohreh Hashami, Leila Fidelino, Zoltan Kovacs, and Lloyd Lumata, American Physical Society (APS) meeting, Baltimore Convention Center, Baltimore, Maryland (March 14-18, 2016).
 12. **Production and NMR signal optimization of hyperpolarized ^{13}C -labelled amino acids**, Christopher Parish, Peter Niedbalski, Sarah Ferguson, Andhika Kiswandhi, and Lloyd Lumata, American Physical Society (APS) meeting, Baltimore Convention Center, Baltimore, Maryland (March 14-18, 2016).
 13. **Dynamic nuclear polarization of ^{13}C -labeled amino acids**, Christopher Parish, Peter Niedbalski, Sarah Ferguson, Andhika Kiswandhi and Lloyd Lumata, Texas Section of the American Physical Society (APS) meeting, Baylor University, Waco, TX (October 29-31, 2015).
 14. **Influence of ^{13}C isotopic labeling location of ^{13}C DNP of acetate using TEMPO free radical**, Christopher Parish, Peter Niedbalski and Lloyd Lumata, American Physical Society (APS) March Meeting, San Antonio, TX (March 2-6, 2015).
- Other Presentations/Posters/Talks (as Contributing Author)
 1. **Temperature Dependence of Proton NMR Relaxation Times at Earth's Magnetic Field**, Fatemeh Khashami, Peter Niedbalski, Christopher Parish, David Clark, Qing Wang, Lloyd Lumata,

- Experimental NMR Conference (ENC), Grand Cypress Hotel, Orlando, Florida (April 29 – May 4, 2018).
2. **Magnetic Field-Dependent Lifetimes of Hyperpolarized Carboxyl ^{13}C Spins at cryogenic Temperatures**, Peter Niedbalski, Qing Wang, Fatemeh Khashami, Andhika Kiswandhi Lloyd Lumata, 51st Annual American Chemical Society-DFW meeting, Southern Methodist University, Dallas, Texas (April 21, 2018).
 3. **Temperature Dependence of Proton NMR Relaxation Times at Earth's Magnetic Field**, Fatemeh Khashami, Peter Niedbalski, Christopher Parish, David Clark, Qing Wang, and Lloyd Lumata, 51st Annual American Chemical Society-DFW meeting, Southern Methodist University, Dallas, Texas (April 21, 2018).
 4. **Magnetic field-dependent lifetimes of ^{13}C spins at cryogenic temperature**, Peter Niedbalski, Qing Wang, Christopher Parish, Fatemeh Khashami, and Lloyd Lumata, Texas Section of the American Physical Society (APS) meeting, University of Texas at Dallas, Richardson, Texas (October 20-21, 2017).
 5. **Transition metal doping reveals link between electron T_1 reduction and ^{13}C dynamic nuclear polarization efficiency**, Peter Niedbalski, Christopher Parish, Qing Wang, Zahra Hayati, Likai Song, Andre Martins, A. Dean Sherry, and Lloyd Lumata, Texas Section of the American Physical Society (APS) meeting, University of Texas at Dallas, Richardson, Texas (October 20-21, 2017).
 6. **Temperature-dependent proton relaxation time T_1 of water:glycerol solutions at earth's magnetic field**, Fatemeh Khashami, Qing Wang, Peter Niedbalski, and Lloyd Lumata, Texas Section of the American Physical Society (APS) meeting, University of Texas at Dallas, Richardson, Texas (October 20-21, 2017).
 7. **Hyperpolarized ^{89}Y -EDTP and ^{89}Y -DTPP as pH sensitive MRI agents**, Qing Wang, Peter Niedbalski, Christopher Parish, James Ratnakar, Zoltan Kovacs, and Lloyd Lumata, Texas Section of the American Physical Society (APS) meeting, University of Texas at Dallas, Richardson, Texas (October 20-21, 2017).
 8. **Hyperpolarized ^{89}Y -EDTP and ^{89}Y -DTPP as pH sensitive MRI agents**, Qing Wang, Peter Niedbalski, Christopher Parish, James Ratnakar, Zoltan Kovacs, and Lloyd Lumata, 50th Annual American Chemical Society-DFW meeting, Texas Christian University, Fort Worth, Texas (April 29, 2017).
 9. **Dynamic nuclear polarization: boosting MRI signals by >10,000-fold**, Peter Niedbalski, Christopher Parish, Qing Wang, and Lloyd Lumata, 50th Annual American Chemical Society-DFW meeting, Texas Christian University, Fort Worth, Texas (April 29, 2017).
 10. **Hyperpolarized ^{89}Y -EDTP and ^{89}Y -DTPP as pH sensitive MRI agents**, Qing Wang, Peter Niedbalski, Christopher Parish, James Ratnakar, Zoltan Kovacs, and Lloyd Lumata, 58th Experimental NMR Conference (ENC), Asilomar, California (March 26-31, 2017).
 11. **A 180 GHz dynamic nuclear polarization system using a cryogen-free and sweepable superconducting magnet**, Andhika Kiswandhi, Peter Niedbalski, Christopher Parish, Qing Wang, and Lloyd Lumata, 58th Experimental NMR Conference (ENC), Asilomar, California (March 26-31, 2017).
 12. **^{13}C dynamic nuclear polarization using derivatives of TEMPO free radical**, Peter Niedbalski, Christopher Parish, Qing Wang, Andhika Kiswandhi, and Lloyd Lumata, 58th Experimental NMR Conference (ENC), Asilomar, California (March 26-31, 2017).
 13. **Influence of Tb^{3+} and Dy^{3+} doping on ^{13}C dynamic nuclear polarization**, Peter Niedbalski, Christopher Parish, Andhika Kiswandhi, Zahra Hayati, Likai Song, Leila Fidelino, Chalermchai Khemtong, Andre Martins, A. Dean Sherry, and Lloyd Lumata, 58th Experimental NMR Conference (ENC), Asilomar, California (March 26-31, 2017).

14. **^{13}C dynamic nuclear polarization using trimeric gadolinium complex**, Peter Niedbalski, Christopher Parish, Qing Wang, Andhika Kiswandhi, Zahra Hayati, Likai Song, Magnus Karlsson, Mathilde Lerche, and Lloyd Lumata, 58th Experimental NMR Conference (ENC), Asilomar, California (March 26-31, 2017).
15. **^{13}C dynamic nuclear polarization using trimeric gadolinium complex**, Peter Niedbalski, Christopher Parish, Qing Wang, Andhika Kiswandhi, Zahra Hayati, Likai Song, Magnus Karlsson, Mathilde Lerche, and Lloyd Lumata, 58th Experimental NMR Conference (ENC), Asilomar, California (March 26-31, 2017).
16. **Influence of Dy^{3+} and Tb^{3+} on ^{13}C dynamic nuclear polarization**, Peter Niedbalski, Christopher Parish, Andhika Kiswandhi, Zara Hayati, Andre Martins, Leila Fidelino, Chalermchai Khemtong, Likai Song, A. Dean Sherry, and Lloyd Lumata, Southwest Regional Meeting of the American Chemical Society (ACS), Galveston Convention Center, Galveston, Texas (November 10-13, 2016).
17. **Dynamic nuclear polarization of low-gamma nuclei**, Qing Wang, Christopher Parish, Peter Niedbalski, Andhika Kiswandhi, Zoltan Kovacs, and Lloyd Lumata, Southwest Regional Meeting of the American Chemical Society (ACS), Galveston Convention Center, Galveston, Texas (November 10-13, 2016).
18. **Influence of Ho^{3+} -doping on ^{13}C dynamic nuclear polarization**, Andhika Kiswandhi, Peter Niedbalski, Christopher Parish, Pavanjeet Kaur, Andre Martins, Leila Fidelino, Chalermchai Khemtong, Likai Song, A. Dean Sherry, and Lloyd Lumata, Joint Meeting of the Texas and Four Corners Sections of the American Physical Society (APS), New Mexico State University, Las Cruces, New Mexico (October 21-22, 2016).
19. **Ho-DOTA as a polarization enhancer for dissolution dynamic nuclear polarization**, Andhika Kiswandhi, Christopher Parish, Peter Niedbalski, Pavanjeet Kaur, Zahra Hayati, Andre Martins, A. Dean Sherry, Chalermchai Khemtong, Likai Song, and Lloyd Lumata, NSF Site Visit Symposium for Early Career Scientists, National High Magnetic Field Laboratory (NHMFL), Tallahassee, FL (August 29-31, 2016).
20. **Temperature dependence of proton NMR relaxation times at Earth's magnetic field**, Peter Niedbalski, Christopher Parish, Andhika Kiswandhi, Sarah Ferguson, Eduardo Cervantes, Anisha Oomen, Anagha Krishnan, Aayush Goyal, and Lloyd Lumata, Experimental NMR Conference (ENC), Wyndham Grand Hotel, Pittsburgh, Pennsylvania (April 10-15, 2016).
21. **Dynamic Nuclear Polarization of Carbonyl and Methyl ^{13}C Spins in Acetate Using Trityl OX063**, Peter Niedbalski, Christopher Parish, Zoltan Kiswandhi, and Lloyd Lumata, Experimental NMR Conference (ENC), Wyndham Grand Hotel, Pittsburgh, Pennsylvania (April 10-15, 2016).
22. **Development and Performance of a 180 GHz Dissolution DNP Hyperpolarizer**, Andhika Kiswandhi, Peter Niedbalski, Christopher Parish, Sarah Ferguson, David Taylor, George MacDonald, and Lloyd Lumata, Experimental NMR Conference (ENC), Wyndham Grand Hotel, Pittsburgh, Pennsylvania (April 10-15, 2016).
23. **^{13}C Dynamic Nuclear Polarization Using Isotopically-Enriched 4-oxo-TEMPO Free Radicals**, Peter Niedbalski, Christopher Parish, Andhika Kiswandhi, and Lloyd Lumata, Experimental NMR Conference (ENC), Wyndham Grand Hotel, Pittsburgh, Pennsylvania (April 10-15, 2016).
24. **The effects of Ho^{3+} -DOTA doping on ^{13}C dynamic nuclear polarization: ESR and hyperpolarization studies**, Andhika Kiswandhi, Christopher Parish, Peter Niedbalski, Pavanjeet Kaur, Zahra Hayati, Andre Martins, A. Dean Sherry, Chalermchai Khemtong, Likai Song, and Lloyd Lumata, Experimental NMR Conference (ENC), Wyndham Grand Hotel, Pittsburgh, Pennsylvania (April 10-15, 2016).
25. **Hyperpolarized ^{89}Y NMR spectroscopic detection of Yttrium ion and DOTA macrocyclic ligand complexation: pH dependence and YDOTA intermediates**, Sarah Ferguson, Peter

- Niedbalski, Christopher Parish, Andhika Kiswandhi, Zoltan Kovacs, and Lloyd Lumata, American Physical Society (APS) meeting, Baltimore Convention Center, Baltimore, Maryland (March 14-18, 2016).
26. **Real-time tracking of dissociation of hyperpolarized ^{89}Y -DPTA: a model for degradation of open-chain Gd^{3+} MRI contrast agents**, Sarah Ferguson, Peter Niedbalski, Christopher Parish, Andhika Kiswandhi, Zoltan Kovacs, and Lloyd Lumata, American Physical Society (APS) meeting, Baltimore Convention Center, Baltimore, Maryland (March 14-18, 2016).
 27. **Temperature dependence of proton NMR relaxation times at Earth's magnetic field**, Peter Niedbalski, Christopher Parish, Andhika Kiswandhi, Sarah Ferguson, Eduardo Cervantes, Anisha Oomen, Anagha Khrishnan, Aayush Goyal, and Lloyd Lumata, American Physical Society (APS) meeting, Baltimore Convention Center, Baltimore, Maryland (March 14-18, 2016).
 28. **Optimization of ^{13}C dynamic nuclear polarization: isotopic labeling of free radicals**, Peter Niedbalski, Christopher Parish, Andhika Kiswandhi, and Lloyd Lumata, American Physical Society (APS) meeting, Baltimore Convention Center, Baltimore, Maryland (March 14-18, 2016).
 29. **Construction and ^{13}C NMR signal efficiency of a dynamic nuclear polarizer at 6.4 T and 1.4 K**, Andhika Kiswandhi, Peter Niedbalski, Christopher Parish, Sarah Ferguson, David Taylor, George MacDonald, and Lloyd Lumata, American Physical Society (APS) meeting, Baltimore Convention Center, Baltimore, Maryland (March 14-18, 2016).
 30. **Novel Earth's field magnetic resonance imaging of copper-doped water for inexpensive detection of disease**, Anagha Khrishnan, Andhika Kiswandhi, Peter Niedbalski, Christopher Parish and Lloyd Lumata, American Association for the Advancement of Science (AAAS) 2016 Annual Meeting, Washington, D.C. (February 11-15, 2016).
 31. **Dynamic nuclear polarization of carbonyl and methyl ^{13}C spins: ^{13}C acetate samples doped with trityl OX063**, Peter Niedbalski, Christopher Parish and Lloyd Lumata, Texas Section of the American Physical Society (APS) meeting, Baylor University, Waco, TX (October 29-31, 2015).
 32. **The effect of isotopic labeling on 4-oxo-TEMPO free radical on ^{13}C dynamic nuclear polarization**, Peter Niedbalski, Andhika Kiswandhi, Christopher Parish and Lloyd Lumata, Texas Section of the American Physical Society (APS) meeting, Baylor University, Waco, TX (October 29-31, 2015).
 33. **Enhancing the NMR Signals of ^{13}C -enriched Amino Acids via Dynamic Nuclear Polarization**, Aayush Goyal, Christopher Parish, Andhika Kiswandhi, and Lloyd Lumata, 2015 George A. Jeffrey UTD Nanoexplorers Symposium, Richardson, TX (August 12, 2015).
 34. **Novel Earth's Field MR Imaging of Copper Chloride**, Anagha Krishnan, Andhika Kiswandhi, Peter Niedbalski, Christopher Parish, and Lloyd Lumata, 2015 George A. Jeffrey UTD Nanoexplorers Symposium, Richardson, TX (August 12, 2015).
 35. **Dynamic nuclear polarization of carbonyl and methyl ^{13}C spins in acetate using trityl OX063**, Peter Niedbalski, Christopher Parish and Lloyd Lumata, American Physical Society (APS) March Meeting, San Antonio, TX (March 2-6, 2015).

Skills

Nuclear Magnetic Resonance (NMR)
Cell Culture
UV/Vis Spectroscopy
Fluorescence Spectroscopy
Western Blot

C++
Matlab
Dynamic Nuclear Polarization (DNP)
Cell Culture
Magnetic Resonance Imaging (MRI)